# Representing uncertainty in global climate models using stochastic sea ice parameterizations

PhD Thesis
of

Stephan Juricke

Department 1
Physics and Electrical Engineering
Universität Bremen

Bremen
26. May 2014

**Reviewer:**

Prof. Thomas Jung
Alfred Wegener Institute,
Helmholtz Centre for Polar and Marine Research

Prof. Peter Lemke
Alfred Wegener Institute,
Helmholtz Centre for Polar and Marine Research

# Contents

**Zusammenfassung**

Diese Dissertation befasst sich mit der Darstellung von Unsicherheiten in der Modellierung von Meereis, vorrangig mit den Unsicherheiten in der Meereisdynamik. Ein wichtiger Bestandteil der Impulserhaltungsgleichung zur Berechnung der Meereisdrift ist die viskos–plastische Meereisrheologie. Sie beschreibt das Deformationsverhalten des Eises bei konvergenten Driftverhältnissen. Dabei beeinflusst der Eisstärkeparameter die interne Eisstärke, die plastischer Deformation und somit dem Auftürmen des Meereises entgegenwirkt. Unsicherheiten in der Wahl dieses Parameters werden in dieser Arbeit durch symmetrische Perturbationsschemata simuliert. Es werden sowohl zeitliche als auch örtliche Korrelationen in die Generierung der kontinuierlich durchgeführten stochastischen Störungen mit einbezogen. Die Parameterperturbationen werden innerhalb eines Ozean–Meereis– und eines gekoppelten Atmosphäre–Ozean–Meereis–Modells getestet. Ergebnisse zeigen, dass die implementierten Unsicherheitsabschätzungen zu einer Änderung der mittleren Meereisverteilung führen, insbesondere in der Arktis. Ein zufällig reduzierter Eisstärkeparameter führt zu einer Beschleunigung der Meerdrift bei Konvergenz, dem ein zufällig erhöhter Wert im späteren Verlauf nicht im gleichen Maße entgegenwirkt. Dies ist bedingt durch die hochgradig nichtlineare Formulierung der Parameterisierung und resultiert in der Beschleunigung des Meereises durch die symmetrischen Perturbationen. In dem Ozean–Meereis–Modell erfolgt dadurch eine Zunahme dicken, deformierten Eises in Regionen mit vorrangig konvergenter Drift. Diese Zunahme baut sich in der Arktis langsam, aber stetig über Jahrzehnte auf. Das antarktische Meereis weist eine relativ geringe Änderung der mittleren Eisverteilung auf. Im gekoppelten Atmosphäre–Ozean–Meereis–Modell erfolgt durch die Eisstärkeperturbationen ebenfalls eine Beschleunigung der Drift. Jedoch fällt der Einfluss auf die Meereisdickenverteilung geringer aus. Die Ursache sind gekoppelte Feedback–Mechanismen, die einer generellen Eisdickenzunahme entgegenwirken. Darüber hinaus werden im Zusammenhang mit Meereisvorhersagen mit dem gekoppelten Modell Ensemble-Simulationen durchgeführt. Ein Vergleich von Ensembles mit Parameterperturbationen und solchen mit Perturbationen der atmosphärischen Anfangsbedingungen zeigt, dass eine Inklusion von Modellunsicherheiten während der ersten Wochen einer Simulation zu einer stärkeren Streuung der einzelnen Ensemblemitglieder in Bezug auf die zentralarktische Meereisverteilung führt. Dies hat bedeutende Implikationen für Unsicherheitsabschätzungen bei Datenassimililation und Vorhersagen in den polaren Regionen.

**Abstract**

This dissertation deals with the representation of uncertainties in sea ice modelling, especially within the sea ice dynamics. An important term of the momentum balance for computing the evolution of sea ice drift is the viscous–plastic sea ice rheology. It describes the deformation of sea ice under convergent drift. In this context, an ice strength parameter determines the internal ice strength, which counteracts plastic deformation and hence piling up of sea ice. Uncertainties in the choice of the parameter are simulated in this study by application of symmetric perturbation schemes. Temporal as well as spatial correlations are included in the generation of continuously applied stochastic perturbations. The parameter perturbations are implemented in an ocean–sea ice and in a coupled atmosphere–ocean–sea ice model. Results show that including these uncertainty estimates leads to a change in the mean sea ice distribution, especially in the Arctic. A randomly reduced ice strength parameter results in a relative acceleration of sea ice drift under convergence, which cannot be reverted by a randomly increased ice strength in the subsequent course of the simulation. This is caused by the highly nonlinear formulation of the sea ice rheology and results in a general acceleration of sea ice owing to the symmetric perturbations. As a result, the amount of thick, ridged sea ice in regions of predominantly convergent drift is increased. In the Arctic this increase accumulates slowly, but continuously over decades. Antarctic sea ice on the other hand exhibits relatively small changes in the mean sea ice distribution. In the coupled atmosphere–ocean–sea ice model ice strength perturbations lead to increased drift as well, although the impact on the sea ice thickness distribution is reduced. The reason are coupled feedback mechanisms, which counteract a general thickness increase. Finally, ensemble simulations are conducted with the coupled model in the context of sea ice predictions. Comparing ensembles with parameter perturbations and ensembles with atmospheric initial condition perturbations shows that the inclusion of model uncertainty leads to increased ensemble spread for the sea ice distribution of the central Arctic during the first weeks of the simulation. This has important implications for uncertainty estimations in data assimilation and forecasts for the polar regions.

# 1. Introduction

People don't understand the earth,
but they want to, so they build a model,
and then they have two things they don't understand
*Gerard Roe*

In the climate sciences, the prognostic governing equations of the Earth system are well known. They describe the temporal evolution of the relevant variables—such as wind, water and ice velocities—in the different components of the system—i.e. in atmosphere, ocean and sea ice. The equations arise from general laws of physics, such as the laws of mass continuity and conservation of energy. Solving them in a time integrated sense would allow a perfect forecast of the future state of the respective variables. But these solutions cannot be obtained analytically. Therefore, one has to resort to numerical approximations of the solutions. This is done by discretizing the equations in time and space.

Starting from a prescribed initial state of the system, the discretized equations are integrated forward in time, up to the specific date in the future that one would like to forecast. In other words, a model has to be implemented that is a rather simplified and approximated representation of the Earth system or parts thereof.

Different climate models use different techniques for the numerical discretizations, in time as well as space. In general they have in common that each consecutive step forward in time is separated to the previous by a fixed length, called time step. Furthermore, the spatial discretization usually operates on a grid or mesh with a predefined mesh size to resolve the problem at hand (see figure 1.1). The shorter the time step and the finer the mesh size, the more accurate are the numerical approximations. But on the downside, increasing accuracy in this fashion also increases computational costs for solving the problem numerically, as the number of arithmetic operations grows rapidly. Even large state of the art supercomputers that are used for simulations of weather and climate have their limits as to how fast they can actually perform all the necessary computations. Therefore, to produce a forecast for the future state of the Earth system in a reasonable amount of time, time step and grid have to be chosen in a manner that balances accuracy with speed.

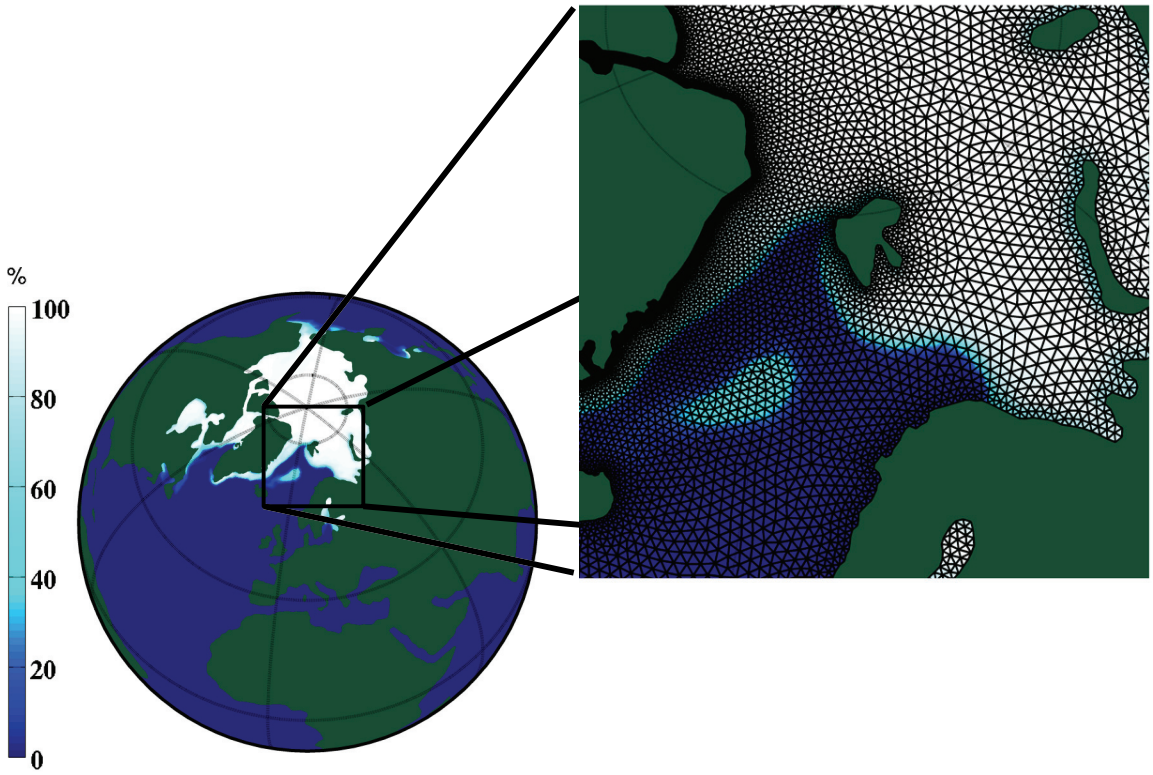


Figure 1.1: Illustration of (left) the discretized world ocean with (right) an unstructured triangular grid. High grid resolution is applied to coast lines (see coast of Greenland in the magnified region to the right). Shown is the Arctic sea ice concentration of January as simulated by a climate integration of the model FESOM. The discretized ocean is blue to white, while the land surface is green.

## 1.1. Uncertainties in weather and climate simulations

Discretizing the governing equations for the simulation of weather and climate leads inevitably to errors and uncertainties in the forecasts. There are fundamentally different sources of such uncertainties in predictions, which will be discussed in detail further below. In general, however, as all of these sources lead to a degraded accuracy of forecasts, their combined effects need to be estimated to allow for informed decisions to be made by stakeholders that rely on weather and climate predictions. These stakeholders can be companies such as insurers that need to estimate possible expenses caused by extreme weather events. Public authorities are stakeholders that issue severe weather warnings or have to adjust a country's infrastructure to a changing climate. But also single individuals want to know how accurate a given weather forecast actually is, as uncertainties of a forecast might affect their plans for the weekend.

As the impacts of human induced, i.e. anthropogenic climate change become more and more palpable, reliable climate predictions become increasingly important as well. In the end, if the climate is changing rapidly owing to human activities, everyone will have an interest to know how these human interferences affect our planet. It has to be investigated what these interactions will eventually cause, in terms of changes in the atmosphere, the land surface, the oceans and the cryosphere, and especially the biosphere. The risks of a changing climate have to be assessed

to allow for useful decision making.

To start a forecast with a model, the simulation has to be initialized. As one would like to predict the evolution of a system given a certain initial state the model has to be provided with such an initialization for every component of the system under consideration, i.e., in case of the Earth system, for the atmosphere, the ocean and so forth. Integrations will then be carried out from these so called initial conditions to determine the evolution of the relevant variables following the laws of physics. But measuring instruments will always entail some measuring errors and will never be able to measure the state of the Earth system completely in time and space. As a result, the initial conditions for predictions of the future state of the system will always be flawed. It is certainly possible to continuously reduce this error, by increasing accuracy and area coverage of measuring instruments such as satellites and weather stations. Nevertheless, uncertainties will always remain. And in some parts (e.g. in the deep ocean) constant, area-wide measurements will be challenging for a long time to come.

Small residual errors in the initial conditions would not be a problem if the system would react to those small deviations from the actual initial state in a foreseeable fashion. This would be the case for a linear system, but not for the components of the Earth system. The atmosphere is known to behave in a very fast and chaotic manner (*Lorenz*, 1963). This leads to the fact that a simulation based forecast of the future state of the atmosphere can differ substantially from the actually observed state within days, just due to rather small errors in the initial conditions. Therefore, forecast accuracy is limited by the accuracy of the initial state. For large parts of the atmosphere it is basically impossible to predict the future state beyond a couple of weeks with considerably more accuracy as would be the case for an educated guess based on the statistics of the climate of past years.

An established method in weather forecasts to account for uncertainties in the initial conditions is to set up ensemble simulations. Each ensemble member starts integration from slightly different initial conditions but uses the same general model configuration. The aim is to sample the uncertainty in the initial conditions. As the forecasts of the single members of the ensemble diverge, possible states of the future atmosphere are generated. The hope is that those states encompass the trajectory of the atmosphere that will be observed in the future (see figure 1.2). Forecasters are then able to diagnose the ensemble and give probabilistic forecasts. A single, deterministic forecast generated by only one single initial state might very well predict a future far from the observed. Probabilistic forecasts, however, include the uncertainties of the initial state. They do not claim to be a hundred percent accurate but rather report on the probability of some future state to actually occur. If the members of the ensemble stay close together, the forecast is comparatively certain. If, on the contrary, the members diverge strongly, uncertainty of the forecast is large.

Aside from uncertainties in the initial conditions simulations of the climate have to deal with uncertainties in the boundary conditions. Boundary conditions present the information that is not itself simulated during the process of integration. An example is the solar forcing or, for an ocean-only simulation, the atmospheric forcing. Especially for climate integrations with forecast lead times of many decades, adequate and accurate boundary conditions are necessary to produce useful predictions. But those conditions can in most cases only be estimated, especially

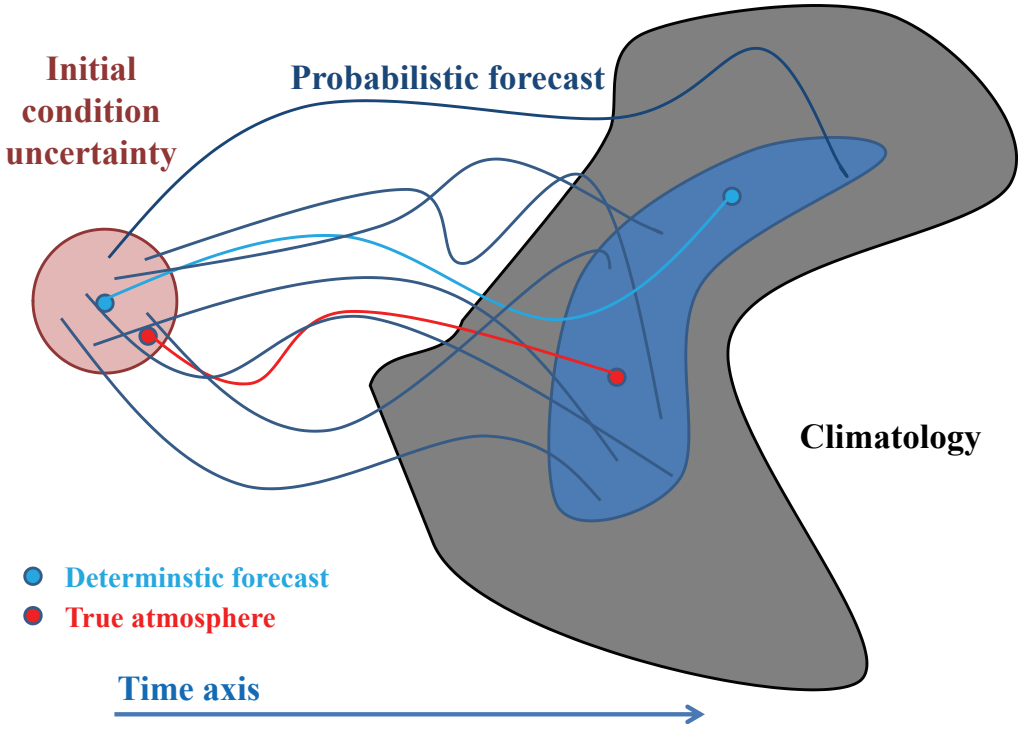


Figure 1.2: Illustration of atmospheric initial condition uncertainty in probabilistic versus deterministic forecasts. The probabilistic forecast takes initial condition uncertainty into account and produces an estimate for forecast uncertainty. The single deterministic forecast is initialized with the best guess of the current state of the atmosphere, but the forecast is far from the actually observed state. Based on a figure at `http://www.easterbrook.ca/steve/2010/07/tracking-down-the-uncertainties-in-weather-and-climate-prediction/` (18.04.2014).

when changes therein during the course of the integration cannot be foreseen.

One well known example in this context is the evolution of $CO_2$ concentrations in the atmosphere. The anthropogenic $CO_2$ emission in the future can hardly be modelled as it depends on changes in politics, economics, human populations and also scientific advances. The latter might even lead to a reduction in atmospheric $CO_2$ concentrations. All these factors make a prediction of the evolution of atmospheric $CO_2$ concentrations very uncertain. This, in turn, leads to uncertainties in changes of the radiative balance of the atmosphere.

The method to tackle boundary condition uncertainty is again based on the concept of ensemble simulations. In the case of atmospheric $CO_2$ concentrations, the climate integrations of the ensemble differ in the prescribed evolution of (anthropogenic) $CO_2$ emissions. Different scenarios are formulated, ranging from a reduction of yearly emissions in the near future, to an unrestricted increase resulting from worldwide industrialization and population growth (see *IPCC SRES*, 2000). Using these different scenarios, changes in the climate such as an increase in surface air temperatures for the future decades can be estimated, depending on the emission scenario that will actually occur. The fifth assessment report of the Intergovernmental Panel on Climate Change (IPCC; see *IPCC AR5 WG1* (2013))[1] uses this information from a whole

[1] See also `http://www.ipcc.ch` (18.04.2014)

variety of different climate models to give estimates on the strength of future climate change for the different scenarios. This information might then be used by politicians and the public in general to decide upon which emission scenario should be aimed at. The decision is based on trading off the costs of implementing a plan to reduce $CO_2$ emissions against future costs and risks caused by climate change if necessary provisions are not made.

Numerical simulations on computers always produce errors. There are, among others, rounding errors that simply originate from the fact that numbers with infinite digits have to be truncated at some point. Moreover, the accuracy of the chosen discretization methods can vary strongly. Derivatives and integrals have to be numerically approximated. This leads to additional truncation errors. These kind of errors may differ in form and magnitude between different model frameworks.

A whole variety of models are used around the world, each one applying more or less differing numerical strategies. A method to estimate the uncertainty related to the numerical discretization strategies is to use an ensemble that consists of different models developed rather independently at different research institutions (multi-model ensemble). The ensemble aims at sampling different so called dynamical cores, i.e. the different strategies to integrate the prognostic governing equations numerically in time and space. This has been done for atmospheric models (e.g. *Gates et al.*, 1999)[2] as well as climate models that include more or less all the components of the Earth system (e.g. *Taylor et al.*, 2012)[3]. Owing to its set-up the ensemble will also sample uncertainties related to the fact that different models might be tuned in ways to best address a certain research or forecasting problem. Models differ in their systematic biases and an ensemble of different models samples these systematic biases as well as a model's particular advantages. Unfortunately it is difficult to retrospectively separate the sources of uncertainty in an ensemble that consist of many fundamentally different models.

When prognostic equations are discretized, processes of time and length scales smaller than the time step and mesh size can no longer be explicitly resolved. Nevertheless, their effects on the resolved larger scales have to be accounted for. To this end, so called parameterizations are developed that take the variables of the resolved large scales and use them to estimate the accumulated impact of unresolved scales on the large scales (see figure 1.3). In other words, the resolved mean flow itself is used to estimate the effect of unresolved fluctuations on the mean flow. Different strategies are applied to develop such parameterizations, considering theoretical results and observational data as well as data from (usually higher resolved) numerical simulations. Depending on the model's resolution in time and space, parameterizations have to be adjusted to account for those processes that are not yet resolved. In the end, though, these parameterizations are again only approximations of the real physics that are meant to be simulated.

Many different strategies have been developed in recent decades to account for model uncertainty related to unresolved scales. They range from methods that try to sample the choice of parameters within the parameterizations (so called perturbed parameter or multi-parameter ensembles) (e.g. *Doblas-Reyes et al.*, 2009; *Weisheimer et al.*, 2011), to methods that try to sample the choice of the parameterizations itself (multi-parameterization or multi-physics ensembles)

[2]See also `http://www-pcmdi.llnl.gov/projects/amip/` (18.04.2014)
[3]See also `http://cmip-pcmdi.llnl.gov/cmip5/` (18.04.2014)

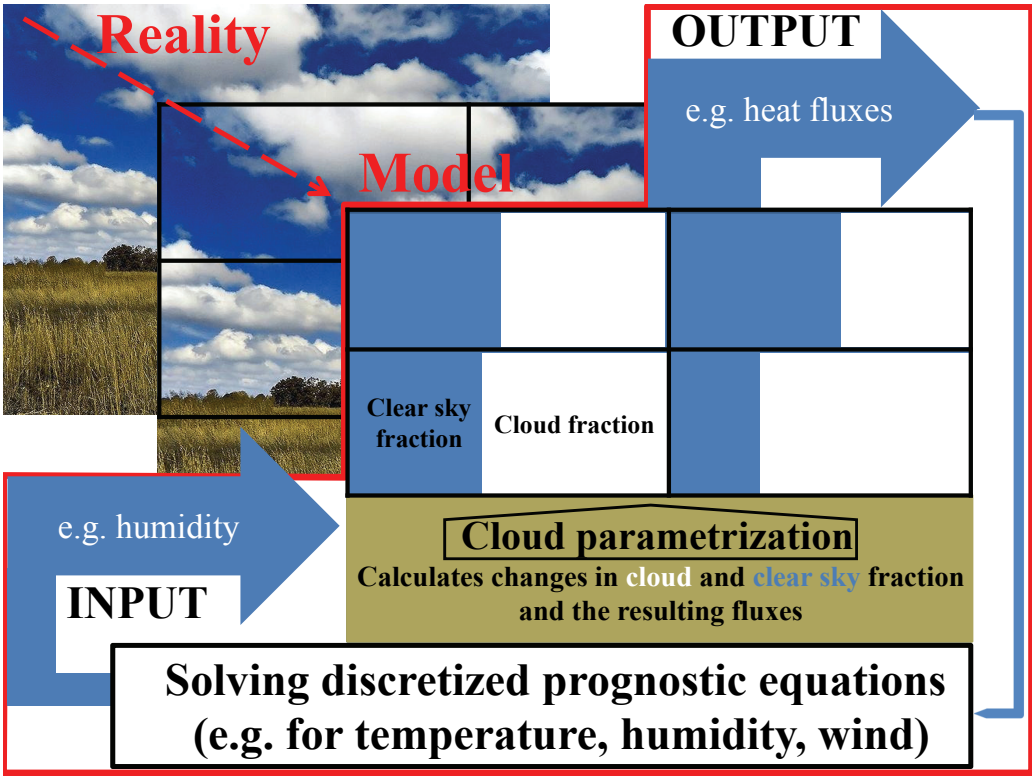


Figure 1.3: Illustration of a simplified cloud parameterization. The real world is discretized and simulated on a mesh with different grid boxes. Single clouds, as observed in nature, are not resolved. But the fraction of each grid box covered by clouds is parameterized using the information supplied by the prognostic variables. From the cloud covered area per grid box, fluxes can be calculated that are used to compute the evolution of the prognostic variables in time. The photograph is from `http://en.m.wikipedia.org/wiki/Parameterization_(atmospheric_modeling)` (18.04.2014).

(e.g. *Berner et al.*, 2011) and, finally, to methods that formulate the parameterizations in a more or less stochastic fashion instead of using *classical* deterministic parameterizations (stochastic parameterization or stochastic physics methods). The latter themselves can again be separated into different categories (as distinguished and discussed in more detail in later sections).

Depending on the focus of research or forecasts, the different sources of uncertainty can vary in their importance for estimating the total uncertainty of the simulations. Figure 1.4 illustrates the dependence of relative importance of uncertainties on the lead time. While initial condition uncertainty is of great importance at short lead times, it is surpassed by model and especially boundary condition uncertainty for longer integrations (*Hawkins and Sutton*, 2009). For regional distributions of fractional uncertainty, relative importance of model uncertainty compared to boundary condition uncertainty at longer lead times is increasing towards the high latitudes, where model uncertainty is at a maximum (see figure 6 of *Hawkins and Sutton*, 2009). In the end it is desirable to include all kinds of uncertainty estimates in a model to be able to represent the total uncertainty of forecasts as best as possible (*Palmer*, 2012)).

Methods of uncertainty estimations can be very costly, though, concerning both time consumption and computing resources. As they make use of ensembles, they are by a factor equal to

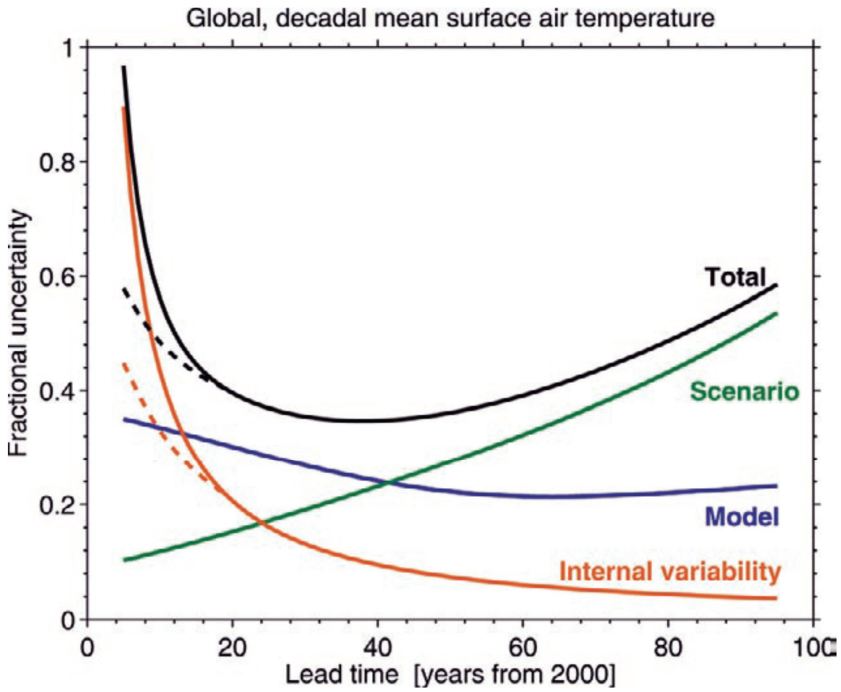


Figure 1.4: Illustration of fractional uncertainty (in relation to global warming since 2000) pertaining to the different sources of forecast uncertainty in predicting the decadal mean of the global surface air temperature. Sources for uncertainty are the internal variability (which is related to initial condition uncertainty), model uncertainty and uncertainty in boundary conditions, i.e. in the $CO_2$ emission scenarios. The dashed lines illustrate possible reductions in initial condition uncertainty related to improved ocean initialization through data assimilation. From *Hawkins and Sutton* (2009).

the number of ensemble members more costly than single integrations[4]. That is why ensemble simulations are often less highly resolved in time and space than single high resolution control simulations. But the advantages of probabilistic ensemble forecasts owing to their estimation of forecast uncertainty can be considerable. Therefore ensemble forecast can complement deterministic predictions that use much higher temporal and spatial resolutions[5]. Still, uncertainty estimation is again a question of balancing speed and costs with accuracy.

## 1.2. Sea ice simulations

In recent decades the specific role of the high latitudes in the context of climate change has attracted a lot of attention, not only in the scientific world but also in the media and public.

[4]The advantage in this context is that ensembles simulations, even though they are costly, can be conducted very efficiently, as they allow for a good parallelization on supercomputers.

[5]The ensemble forecasts at the European Centre for Medium-Range Weather Forecast (ECMWF), as an example, include a deterministic forecast with very high resolution (the highest resolution that has been sufficiently tested at that time) using the best possible model configuration and initial conditions. It also includes one forecast of lower resolution, but again with the best possible configuration and initialization. Finally, the lower resolution forecast is perturbed in initial conditions and model configuration to produce 50 perturbed members for the uncertainty estimation of the forecast. For further information it is referred to `http://www.ecmwf.int` (18.04.2014).

Observed temperature increase has been about twice as large in the Arctic compared to the global mean change[6], a phenomenon called the Arctic amplification (see e.g. *Bekryaev et al.*, 2010; *Pithan and Mauritsen*, 2014). Reduction in Arctic sea ice extent and thickness is claimed to be an indisputable result of increased $CO_2$ concentrations and the resulting enhanced greenhouse effect.

In contrast to melting ice sheets and glaciers, reduced sea ice volume in the polar regions does not contribute to sea level rise as sea ice is floating on the ocean surface. Nevertheless, sea ice thickness and area extent are of great importance when it comes to atmosphere–ocean interactions and the radiation balance at the intermediate surfaces.

Due to their very high reflectivity, called albedo, sea ice and snow on sea ice reflect large parts of short wave solar radiation back to the atmosphere and ultimately to space, reducing the radiative energy absorbed by the earth. This is especially important as the open ocean generally has a very low albedo, absorbing most of the incoming solar short wave radiation. Furthermore, sea ice acts as an insulating layer between atmosphere and ocean, reducing heat, momentum and fresh water exchange between the two components. Heat flux from the ocean to the atmosphere in autumn, when the ocean is still warm and the atmosphere starts to cool, can be reduced by more than an order of magnitude by an ice cover (see e.g. *Wettlaufer*, 1991). Effects of atmospheric winds will be largely shielded from the ocean by sea ice. On the other hand, horizontally rather small scale structures of ridged sea ice can reach a couple of meters up into the atmosphere and many meters down into the ocean, leading to additional turbulence when sea ice is drifting or winds and currents pass by.

Aside from the fact that sea ice will largely prevent snow and rain from reaching the ocean and evaporation from reaching the atmosphere, it influences oceanic fresh water fluxes drastically during its formation and melt. As sea ice contains salt mainly in small so called brine pockets and otherwise consists of fresh water, freezing and melting of sea ice produces large fresh water fluxes. Brine is ejected during the freezing season and fresh water during the melting season. This influences the stability of the ocean and can, by brine ejection and resulting increased water densities, lead to deep convection, which is a main driver of the global thermohaline circulation. To put it simply, in this circulation dense, cold, and rather salty water sinks to the ocean floor in the high latitudes and follows bottom topography around the world until it surfaces again in regions of strong upwelling (see figure 1.5 and for a more detailed discussion *Rahmstorf*, 2002, 2006; *Kuhlbrodt et al.*, 2007).

Some of these interactions with sea ice are very sensitive to changes, leading to positive feedbacks when the balance is perturbed. While negative feedbacks counteract disturbances to the mean state and lead to a stabilization of the system, positive feedbacks amplify the effects of perturbations and tend to destabilize. In this context, the sea ice–albedo feedback, as an example, leads to increased uptake of solar radiation by the ocean when the sea ice cover is reduced. As a consequence, ocean temperatures rise, which in turn enhances sea ice melt. Increase in ice cover on the other hand increases reflectivity and reduces uptake of solar radiation, which favours further sea ice growth. Figure 1.6 illustrates some of the positive

[6]The estimated trend for 1875–2008 is about 1.35 degrees per century for the northern high-latitudes compared to 0.79 degrees per century for the northern hemisphere (*Bekryaev et al.*, 2010).

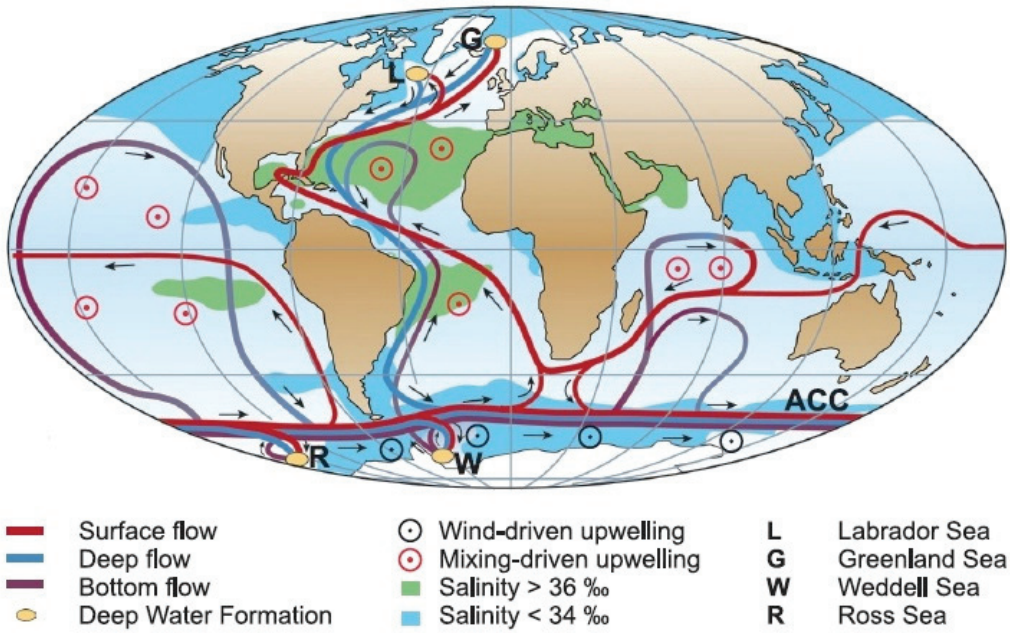


Figure 1.5: Sketch of the global, thermohaline (i.e. driven by temperature and salinity differences) ocean circulation. Deep water formation caused by deep convection takes place in the high latitudes. Upwelling regions are either wind-driven (i.e. caused by divergent winds) or mixing-driven (i.e. caused by water mass properties). From *Kuhlbrodt et al.* (2007) (based on *Rahmstorf*, 2002)

feedbacks triggered by global warming.

A question of prime scientific importance is whether or not a tipping point exists in climate, human-induced or not, where positive feedbacks start to accelerate the change. This is especially true for changes in future sea ice cover. Due to the many positive feedbacks that act in the high latitudes, sensitivity to perturbations can be very large and might lead to irreversible changes.

The trends in sea ice cover in the high latitudes have been very different for the northern and southern hemisphere. While sea ice has decreased considerably in the north, an increase has been observed in the south (see figure 1.7). Some suggestions have been made as to why the Antarctic sea ice does not show a similarly strong response to climate change as the Arctic (e.g. *Turner et al.*, 2007; *Latif et al.*, 2013). It is quite obvious, though, that relevant processes at the two poles differ considerably just simply owing to the topographical differences between the north and the south. In the south a continent resides covered with ice sheets of many kilometers thickness and surrounded by a huge, continuous ocean. The Arctic, however, consists of an ocean surrounded by massive continents with only rather small connections through straits to other oceans in the northern hemisphere. Still, the differences between sea ice in the two hemispheres is a topic of continuous research and, especially in the context of climate change, of great importance.

In addition to research on processes in the high latitudes, there has been an increasing amount of research in the field of teleconnections in recent years. The question is whether and, if so, how changes and generally the climate in high latitudes affect the mid-latitudes (see e.g.

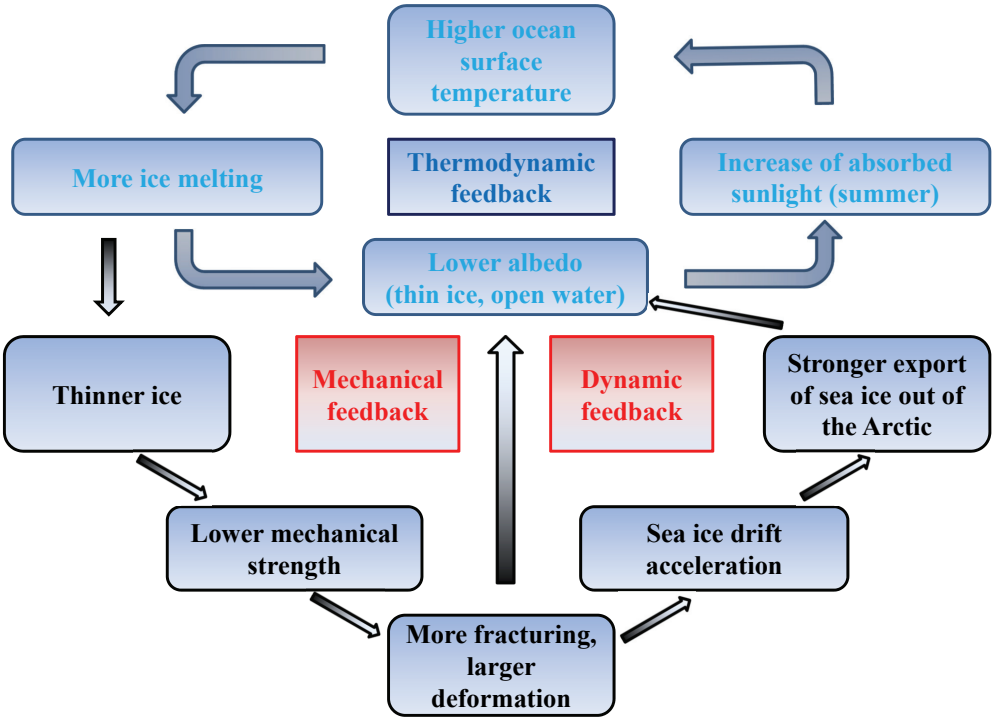


Figure 1.6: Positive Arctic sea ice feedback mechanisms initiated by an increased sea ice melt caused by increased air temperatures. The feedbacks can be separated into a thermodynamic, a mechanical and a dynamic feedback. The first is the so called sea ice–albedo feedback, which is amplified by the response of the drifting sea ice. Figure adapted from *Weiss* (2013).

*Semmler et al.*, 2012). The attention has so far been rather focused on the Arctic, as potential impacts of polar amplification on weather and climate in the mid-latitudes may affect densely populated regions in Europe, Asia and North America. But scientifically it is of equal importance to understand teleconnections and the related processes in the southern hemisphere as well.

## 1.3. Focus and concept of this dissertation: Model uncertainties in sea ice simulations

In a changing climate, knowing the future development of sea ice is of great interest. Therefore it is also necessary to know of the uncertainties in the sea ice predictions. In the high latitudes inaccuracies in the representation of the sub-grid scales have a large impact on the total forecast uncertainty of climate predictions owing to the various feedback mechanisms and complex physical processes involved (*Hawkins and Sutton*, 2009). Additionally, for short term forecasts from days to a few years, estimating the forecast error of sea ice through probabilistic means can be useful in terms of local weather forecasts and hazard analysis for shipping and other economic, but also scientific enterprises in the high latitudes. This is especially true as uncertainties in one component of the Earth system will not remain within this component, but will translate to uncertainties in the other components as well. In case of sea ice this means that uncertainties are translated to the atmosphere and ocean, extending the spatial and temporal range of their

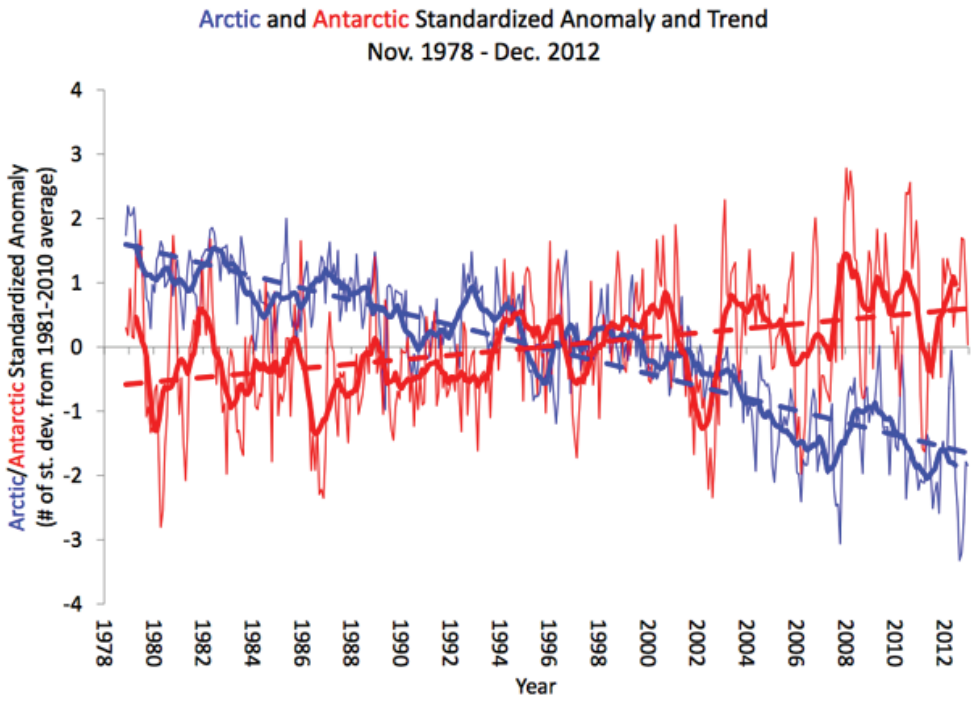


Figure 1.7: Trend in Arctic and Antarctic standardized sea ice extent anomalies from 1979–2012, with units in standard deviations from the 1981–2010 average. Thin lines show monthly mean extent anomalies, thick lines are 12-month running means. From National Snow and Ice Data Center, University of Colorado, Boulder, `http://nsidc.org/cryosphere/sotc/sea_ice.html` (18.04.2014).

impacts. As an example, uncertainty estimation for the predictions of the sea ice edge—and, on a smaller scale, open water leads—would be very useful. This is not only true for predicting the ice edge itself, but also for the related uncertainties in fluxes between atmosphere and ocean, which exhibit a large gradient where the surface waters change from ice-covered to ice-free.

The aim of this dissertation is to develop strategies of model uncertainty representation. More precisely, the impact of including these representations in the simulation of sea ice are analyzed. Up till now model uncertainty representation, especially for uncertainties in parameterizations, has in recent years primarily been applied to atmospheric models in the context of weather forecasts from days to seasons (e.g. *Buizza et al.*, 1999). Uncertainties in the sea ice and also the ocean model have largely been neglected. While this is to some extent also true for uncertainties in the respective initial conditions, this dissertation focuses on the uncertainties related to the model's sub-grid scale parameterizations. Parameters of different sea ice parameterizations are commonly used to tune a sea ice model with respect to the simulated sea ice extent and the thickness distribution. Some of these parameters are very difficult to measure and may vary considerably between models. In addition, the implementation of some parameterizations in the sea ice model may be challenged, as to whether they are capable of accurately representing the statistics of the respective sub-grid scale process or not. As a result, uncertainties related to sea ice parameterizations are large.

I will illustrate in this dissertation that representing model uncertainty in the simulation of sea ice is of great importance, with lead times ranging from days to decades. To do so, I will

introduce a stochastic parameter perturbation scheme aiming at parameter-related uncertainty representation in a sea ice model. While generally employable to a range of uncertain parameters, the main application of the scheme will be the stochastic perturbation of the so called sea ice strength parameter. This parameter determines the internal ice strength as part of the parameterization of the internal forces of the sea ice, which in turn determine the resistance the sea ice exhibits towards convergent drift. It therefore influences the generation of dynamically formed thick ice that piles up under convergent drift of a closely packed sea ice cover. The sea ice strength parameter is commonly used to tune the simulated ice thickness distribution. It varies considerably between models and is very difficult to measure, which suggests that related uncertainties are large. Hence, it is a suitable candidate for the application of a stochastic perturbation scheme.

The structure of the dissertations is as follows: The next chapter is devoted to a short introduction to the two models used in this dissertation. The Finite Element Sea ice–Ocean Model FESOM, developed at the Alfred Wegener Institute, Helmholtz Centre for Polar and Marine Research (AWI) in Bremerhaven, is the tool employed for simulating sea ice distributions and its characteristics. The stochastic parameter perturbations have been implemented in FESOM to account for model uncertainty in the simulations of sea ice. The second model is the coupled atmosphere–ocean–sea ice model ECHAM6-FESOM. As I was involved in the coupling of the atmospheric model ECHAM6 and the sea ice–ocean model FESOM, chapter 2 includes a subsection on coupled model performance regarding a multi-centennial climate integration. The chapter is concluded with a short section on the generation of ensemble simulations.

In chapter 3 three different stochastic ice strength parameterizations of varying complexity and their implementation in FESOM are described. The parameterizations are compared and analyzed concerning their impact on the simulated Arctic mean climate as well as some characteristics of stochastic ensemble simulations. Chapter 3 has been published in the *Journal of Climate* under the title *Effects of stochastic ice strength perturbation on Arctic finite element sea ice modeling* (*Juricke et al.*, 2013).

The application of the stochastic sea ice strength perturbations in the fully coupled model ECHAM6-FESOM is discussed in chapter 4. Impacts of the perturbations on the mean climate are compared to those observed in a sea ice–ocean simulation with prescribed atmospheric fluxes generated by ECHAM6. It highlights considerable differences in the climatic response to the stochastic perturbations caused by atmospheric feedback mechanisms when an atmospheric model is coupled to sea ice and ocean. Chapter 4 has been published in the *Philosophical Transactions of the Royal Society A: Mathematical, Physical and Engineering Sciences* under the title *Influence of stochastic sea ice parametrization on climate and the role of atmosphere–sea ice–ocean interaction* (*Juricke and Jung*, 2014).

Finally, chapter 5 deals with the concept of potential predictability in the high latitudes, focusing on sea ice. The influence of incorporating model uncertainty estimates by applying stochastic perturbations of the ice strength parameter on potential predictability and initial sea ice spread growth is discussed. Chapter 5 is about to be resubmitted to the *Geophysical Research Letters* under the title *Potential sea ice predictability and the role of stochastic sea ice perturbations* (*Juricke et al.*, 2014).

The dissertation is concluded with a summary of the results in chapter 6 and an outlook in chapter 7 that includes information on additional research in stochastic parameter perturbations and parameterizations that is currently being carried out.

# 2. Model description

## 2.1. FESOM

This section will provide a short introduction to the Finite Element Sea ice–Ocean Model FESOM. As FESOM is the main tool of this dissertation for simulating sea ice, the purpose is to briefly describe the functioning of the model. To this end, the governing equations of the ocean and sea ice component of FESOM are described separately in sections 2.1.1 and 2.1.2. Afterwards the discretization procedure for these equations is laid out in section 2.1.3. Details of the coupling procedure between the sea ice and the ocean as well as boundary conditions to the prognostic equations are neglected in this introduction to FESOM. They are not essential for the understanding of the results presented in chapters 3 to 5. A more detailed description of FESOM can be found in *Timmermann et al.* (2009) and *Wang et al.* (2013). Additionally, in chapter 3 of this dissertation model details that are relevant for the stochastic ice strength perturbations and the conducted experiments are discussed.

### 2.1.1. Governing equations: Ocean

In the simulation of the ocean state the evolution of the four main variables is modelled by the discretization of governing equations. Those variables are

- $\vec{\mathbf{u}} = \vec{\mathbf{u}}(x, y, z, t) = (u(x, y, z, t), v(x, y, z, t), w(x, y, z, t))$ the three-dimensional ocean velocity vector in $(\mathrm{m\ s^{-1}}, \mathrm{m\ s^{-1}}, \mathrm{m\ s^{-1}})$
- $\eta_o = \eta_o(x, y, t)$ the sea surface height of the ocean in m
- $S(x, y, z, t)$ the salinity of sea water in $\mathrm{g\ kg^{-1}}$
- $\theta(x, y, z, t)$ the potential water temperature in K

The variables depend on time $t \geq 0$ (in s) and spatial coordinates $x$, $y$, and $z$. The horizontal coordinates $x$ and $y$ are given in m, but can also be given as geographic coordinates longitude $x_{lon}$ and latitude $y_{lat}$ in degrees or radians *East/West* and *North/South*, respectively. The vertical coordinate $z$ is given in m.

The evolution of the velocity vector $\vec{\mathbf{u}}$ is described by the equations of momentum balance (*Wang et al.*, 2008)

$$\partial_t u + (\vec{\mathbf{u}} \cdot \nabla_3 u) - fv + \frac{1}{\rho_0}\partial_x p + g\partial_x \eta_o = \nabla \cdot A_h \nabla u + \partial_z A_v \partial_z u, \tag{2.1}$$

$$\partial_t v + (\vec{\mathbf{u}} \cdot \nabla_3 v) + fu + \frac{1}{\rho_0}\partial_y p + g\partial_y \eta_o = \nabla \cdot A_h \nabla v + \partial_z A_v \partial_z v, \tag{2.2}$$

as well as the continuity equation for mass conservation

$$\partial_x u + \partial_y v + \partial_z w = 0, \tag{2.3}$$

and the assumption of hydrostatic balance for pressure $p$, in N m$^{-2}$,

$$\partial_z p = -g\rho. \tag{2.4}$$

In this context $\partial_t u := \dfrac{\partial u}{\partial t}$, $\nabla_3$ is the three-dimensional and $\nabla$ the two dimensional Nabla operator. For the density $\rho$, in kg m$^{-3}$, the equation of state

$$\rho = \rho(\theta, S, z)$$

is applied, which relates density $\rho$ to potential temperature $\theta$ and salinity $S$ of water at a given depth $z$. In the above equations $\rho_0$ is the reference density $\rho_0 = 1000\,\mathrm{kg\ m^{-3}}$, $g$ is the gravitational acceleration $g = 9.81\,\mathrm{m\ s^{-2}}$, and $f$ is the Coriolis parameter

$$f = \frac{4\pi}{86400}\sin(y_{lat})\,\mathrm{s^{-1}} \tag{2.5}$$

depending on the latitude $y_{lat}$. Additionally, lateral and vertical viscosities are given by $A_h$ and $A_v$ in m$^2$ s$^{-1}$. The equations of momentum balance (2.1) and (2.2) describe temporal changes in horizontal velocities, i.e. accelerations that arise from the imbalance between terms from advection, Coriolis force, pressure gradient, sea surface elevation and the terms for divergence. The hydrostatic balance (2.4) arises from the equation of vertical momentum balance. The continuity equation (2.3), as already stated, is a result of the law of mass conservation.

The prognostic equation for the sea surface height $\eta_o$

$$\partial_t \eta_o + \nabla \cdot \int_{z=-H}^{z=\eta_o} \begin{pmatrix} u \\ v \end{pmatrix} \mathrm{d}z = P - E \tag{2.6}$$

describes changes in sea surface elevation by influx or efflux of mass, with $H = H(x, y)$ as total ocean depth (with respect to $z = 0\,\mathrm{m}$) in m and $P - E$ as precipitation minus evaporation (at the surface) in m s$^{-1}$. Finally, energy conservation and mass conservation for potential temperature $\theta$ and salinity $S$, respectively, are given by

$$\partial_t \theta + \vec{\mathbf{u}} \cdot \nabla_3 \theta = \nabla \cdot K_h \nabla \theta + \partial_z K_v \partial_z \theta, \tag{2.7}$$

$$\partial_t S + \vec{\mathbf{u}} \cdot \nabla_3 S = \nabla \cdot K_h \nabla S + \partial_z K_v \partial_z S. \tag{2.8}$$

In (2.7) and (2.8) $K_h$ and $K_v$ are the lateral and vertical diffusivity in m$^2$ s$^{-1}$. Comparable to equations (2.1) and (2.2), (2.7) and (2.8) describe changes in $\theta$ and $S$ due to imbalances between

the advection and the diffusion terms.

### 2.1.2. Governing equations: Sea ice

The relevant variables for the sea ice model are

- $h = h(x, y, t)$ the (effective) ice thickness in m (volume per given area $A_{grid}$).
- $h_s = h_s(x, y, t)$ the (effective) snow thickness in m (volume per given area $A_{grid}$).
- $A = A(x, y, t)$ the sea ice concentration for a given area $A_{grid}$ as a dimensionless quantity, with $A \in [0, 1]$.
- $\vec{\mathbf{u}}_i = \vec{\mathbf{u}}_i(x, y, t) = (u_i(x, y, t), v_i(x, y, t))$ the lateral sea ice (and snow on sea ice) drift velocity in $(\mathrm{m\ s^{-1}}, \mathrm{m\ s^{-1}})$.

Sea ice is assumed to be a two dimensional, quasi continuous fluid. Therefore, vertical velocities are neglected. The reference area $A_{grid}$ is the area of the respective grid box under consideration, after the equations have been discretized. It depends on location and grid configuration. The discretization method is discussed below. Dividing sea ice thickness by area concentration $h/A$ results in the actual sea ice thickness of the ice-covered part of the grid box under consideration.

Changes in $h$, $h_s$, and $A$ are given by the prognostic equations

$$\partial_t h + \nabla \cdot (\vec{\mathbf{u}}_i h) = S_h, \tag{2.9}$$

$$\partial_t h_s + \nabla \cdot (\vec{\mathbf{u}}_i h_s) = S_s, \tag{2.10}$$

$$\partial_t A + \nabla \cdot (\vec{\mathbf{u}}_i A) = S_A, \tag{2.11}$$

each one describing increase or decrease of sea ice and snow thickness $h$ and $h_s$ as well as sea ice concentration $A$ due to dynamic sea ice drift and the respective thermodynamic freezing and melting terms $S_h$, $S_s$, and $S_A$, with $S_h$ and $S_s$ in $\mathrm{m\ s^{-1}}$ and $S_A$ in $\mathrm{s^{-1}}$. These include changes due to snow fall and conversion of snow to ice by flooding of snow covered ice floes. Changes in the sea ice drift are given by the momentum balance (*Hibler*, 1979)

$$m \left( \frac{\partial \vec{\mathbf{u}}_i}{\partial t} + \vec{\mathbf{u}}_i \cdot \nabla \vec{\mathbf{u}}_i \right) = \vec{\boldsymbol{\tau}}_{air} + \vec{\boldsymbol{\tau}}_{ocean} - mf\vec{\mathbf{k}} \times \vec{\mathbf{u}}_i - mg\nabla\eta_o + \vec{\mathbf{F}}_{int}, \tag{2.12}$$

with $\vec{\boldsymbol{\tau}}_{air}$ and $\vec{\boldsymbol{\tau}}_{ocean}$ as atmospheric (wind induced) and oceanic (ocean current induced) stresses in $\mathrm{N\ m^{-2}}$, $\vec{\mathbf{k}} = (0, 0, 1)$, $m$ the mass per area with $m = \rho_{ice} h$ in $\mathrm{kg\ m^{-2}}$, and $\rho_{ice}$ the density of sea ice in $\mathrm{kg\ m^{-3}}$. Coriolis force and the force due to the sea surface elevation are similar to those within the momentum balance for the ocean in (2.1) and (2.2). The last term on the right-hand side, $\vec{\mathbf{F}}_{int}$ in $\mathrm{N\ m^{-2}}$, represents the internal forces of the sea ice (per area) which counteract convergent or shear drift. Generally, the advection term (second term on the left-hand side) is

neglected in the discretization of the equation as it is of relatively small magnitude compared to the other terms. The balance of forces in equation (2.12) is illustrated by figure 2.1.

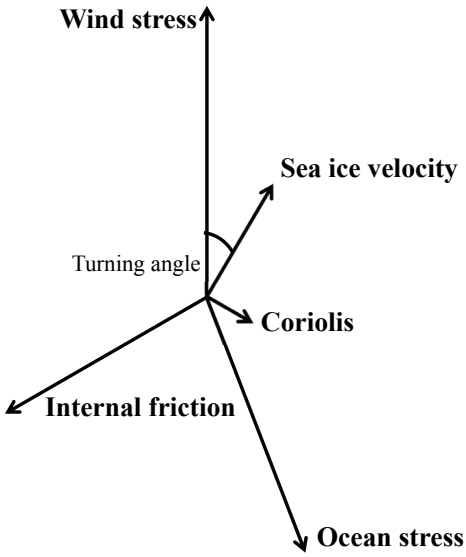


Figure 2.1: Illustration of an exemplary force balance for the sea ice dynamics. Based on *Hunkins* (1975).

The major focus of this dissertation is the uncertainty estimation of parameterizations in the sea ice model, more specifically the parameterization of the internal forces $\vec{\mathbf{F}}_{int}$ in equation (2.12) of the sea ice dynamics. In chapter 3 the parameterization of this term is discussed in more detail.

### 2.1.3. Discretization

Now that all relevant variables are identified and the prognostic equations that govern their evolution are formulated, the next step is to find a solution for the equations for a given time and location. To this end, the equations need to be discretized. This means, approximations for the derivatives in time and space need to be chosen. In case of FESOM, time derivatives are approximated by finite differences, while spatial derivatives are approximated by the finite element method. Instead of solving the equations for the variables $u$, $v$, $w$, $\eta_o$, $S$, $\theta$, $A$, $h$, $h_s$, $u_i$, and $v_i$ continuously in time $t$ and space $(x, y, z)$, solutions are approximated at discrete times and locations. The finite differences estimate the time derivatives in the governing equations by differences between the current and previous discrete instants of time. This makes it possible to approximate the temporal evolution of the variables. The actual numerical finite difference schemes applied by FESOM are explained by *Wang et al.* (2013).

The finite element method is a specific method of numerical discretization not commonly applied in global sea ice–ocean modelling. While the size of the time step in FESOM is fixed during the course of the simulation and given by $\Delta t$, the finite element mesh used for the

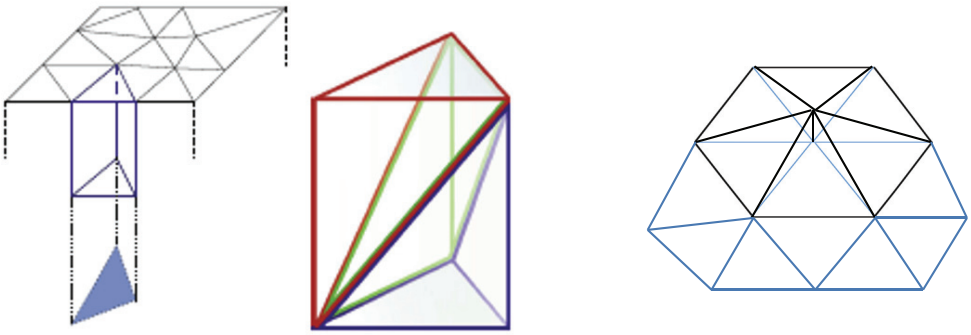

Figure 2.2: Left: Unstructured triangular surface grid and expansion in the vertical direction by subdividing subjacent prisms at different levels. Middle: Prisms are once more subdivided into tetrahedrons. Right: Illustration of a basis function on a grid node. Left and middle panel from *Timmermann et al.* (2009).

discretization of the spatial domain is an unstructured triangular grid on the ocean surface. It can vary in the distances between neighbouring nodes and therefore sizes of the triangles. In the vertical, three-dimensional tetrahedrons are stacked on top of each other throughout the water column from ocean floor to sea level height. This is done by subdividing the triangular columns below each surface triangle in predefined levels and than again subdividing the resulting prisms into three tetrahedrons each (see figure 2.2).

Due to the flexibility of the triangles in size and shape, different domains with complex boundaries can be filled out more easily than would be the case for rectangular grids that are used by spatial finite differences (see figure 2.3). This is not only true for fine details of the coastal boundaries at the surface but also for the complex bathymetry. In addition, as larger triangles lead to larger approximation errors, triangles can be continuously reduced in size to suit regions of interest where fast or interesting processes occur that need to be resolved very precisely. This may, for example, be the case in areas where rather narrow and fast ocean currents occur (e.g. for the western boundary currents). On the downside, discretization using the finite element method is computationally quite expensive when compared to other discretization schemes. The latter are usually not capable of consistently implementing such a flexible spatial resolution, though.

For applications of FESOM in this dissertation the model domain is the entire ocean and the grid is fitted as best as possible to the domain, balancing a good representation and high resolution of the ocean with a reasonable speed of the simulations.

The sea ice model as part of FESOM makes use of the same surface mesh as the ocean. This results in a straightforward coupling of fluxes—such as fresh water and heat—between the two components (see *Timmermann et al.* (2009) for details). Informations on the specific global ocean grids and resolutions as well as time step sizes that have been used for the applications of this dissertation are given in the respective chapters.

The actual finite element method is based on approximating the partial differential equations in space by weighted basis functions. On each node of the grid, that is on each vertex of each triangle, one of those basis functions is defined. In case of FESOM, where linear basis functions

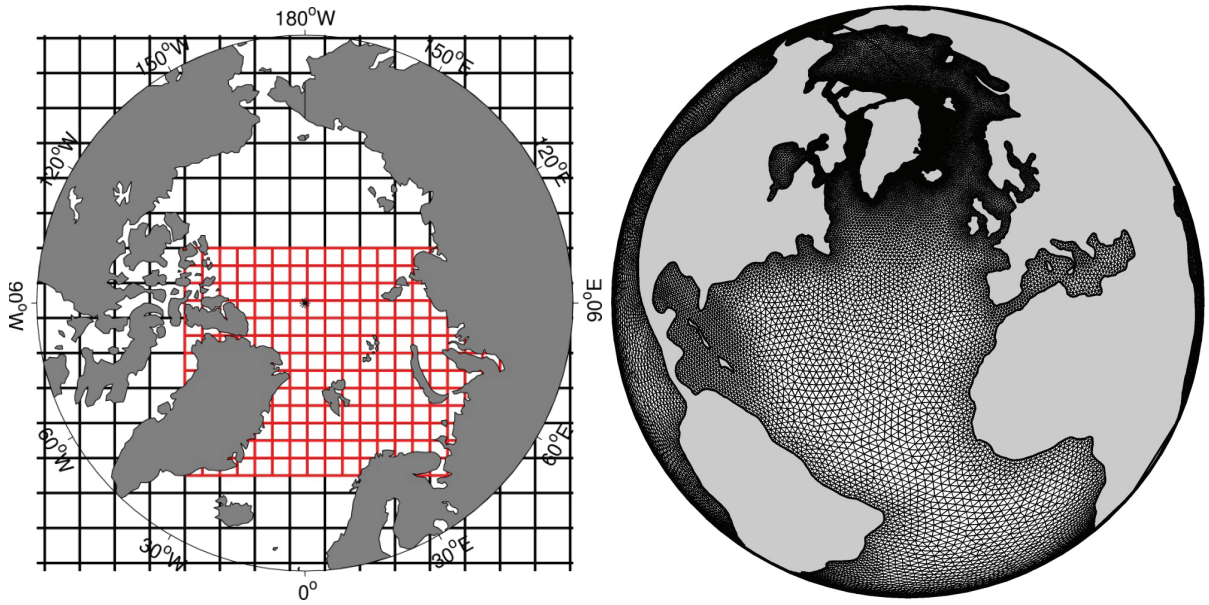


Figure 2.3: Left: Nesting of a finer resolved, rectangular grid in a grid with lower resolution. Boundaries between the two grids are crucial and cause additional interpolation errors during the course of the integration. Right: Global triangular grid with smoothly and consistently varying grid resolution. This allows for locally high resolution but causes no additional interpolation errors. By courtesy of T. Rackow (18.04.2014).

are chosen, each of those functions is 1 at its respective node, reduces linearly to 0 towards its direct neighbours and is 0 everywhere else (see figure 2.2, right). As the approximated solutions of the governing differential equations are now based on linear combinations of those basis functions—which are easy to differentiate in space—the solutions are given by continuous, piecewise linear functions of the form

$$\nu(x, y, z, t) = \sum_{k=1}^{N_\nu} \nu_k(t)\psi_k(x, y, z), \tag{2.13}$$

with $\nu = \nu(x, y, z, t)$ as an approximated solution for one of the prognostic variables of the ocean or sea ice model. $N_\nu$ is the amount of grid points with $\nu_k(t)$ the value of $\nu$ at the coordinates of node $k$ and time $t$ and with $\psi_k(x, y, z)$ the basis function defined at node $k$. In the cases of $\nu$ being a variable of the sea ice model, or $\eta_o$, $N_\nu$ is equal to the amount of surface nodes, while for all other ocean model variables $N_\nu$ is equal to the amount of 3D nodes. After inserting the approximated solution (2.13) into the respective equations, differentiating in space and discretizing the time derivatives by finite differences, a system of linear equations with the dimension equal to the amount of nodes needs to be solved $j$ times in successive order to calculate $\nu_k(j\Delta t)$. Therefore, as the mesh gets finer and the amount of 2D and 3D nodes increases, so does the amount summands in (2.13) and the dimension of the linear system. For a more detailed explanation of the spatial and temporal discretization it is once more referred to *Timmermann et al.* (2009) and *Wang et al.* (2013).

## 2.2. ECHAM6-FESOM

In this section the coupled atmosphere–ocean–sea ice model ECHAM6-FESOM is introduced. A brief description of the atmospheric model ECHAM6 in section 2.2.1 is followed by some information on the coupling procedure between the ECHAM6 and FESOM in section 2.2.2. As I assisted in the coupling of the models and the diagnosing of the coupled system, and to give an overview of the performance of the coupled model, a multi-centennial climate integration is compared to observational and reanalysis data in section 2.2.3.

The configuration of FESOM in ECHAM6-FESOM is basically the same as for uncoupled sea ice–ocean simulations, with some minor changes applied to relevant model parameters and parameterizations in general. These changes serve the purpose to tune the model in the coupled set-up. Also, the thermodynamics of the sea ice model concerning heat balances for open ocean and ice-covered grid fractions have been adjusted. The atmospheric fluxes are now calculated by the atmospheric model ECHAM6 based on the sea ice and snow thickness, sea ice concentration and sea surface temperature fields provided by FESOM. FESOM uses these fluxes to calculate the heat balance separately for open ocean and ice-covered node area fractions, which results in the thermodynamic growth rates of ice (see *Sidorenko et al.*, 2014). For a detailed discussion of ECHAM6-FESOM it is referred to *Sidorenko et al.* (2014).

As a result of the coupling, FESOM simulations can be conducted using atmospheric forcing generated by a coupled ECHAM6-FESOM integration carried out beforehand. To prepare the coupled system for the simulations of chapter 4, I implemented this option for ECHAM6-FESOM. An uncoupled FESOM simulation with prescribed ECHAM6 forcing can be used to detect the effects of coupling. Effects of new processes or changes implemented in the sea ice–ocean model can be compared between simulations carried out with the uncoupled configuration and with the coupled system ECHAM6-FESOM, where the atmospheric model can react to changes in the ocean and sea ice. As is shown in chapter 4, this procedure can be a very handy tool to analyze the different behaviours of climate models of different complexity, but accordances in some components. This is the case for FESOM compared to the much more sophisticated ECHAM6-FESOM. Not surprisingly, impacts of new implementations in the two models can be very different. Therefore extrapolation of results from one to the other should be handled with utmost care. This is especially true when it comes to coupled model tuning and the use of identical parameter and parameterization sets for uncoupled and coupled simulations.

### 2.2.1. ECHAM6

The atmospheric model ECHAM6 has been developed at the Max Planck Institute for Meteorology in Hamburg (MPI Hamburg) and is an atmospheric climate model based on the ECMWF atmospheric model (hence ECHAM, version 6). It is a spectral model, which means that the basis functions for the approximation of the solutions of the relevant (dry) atmospheric variables (i.e. vorticity, divergence, temperature, logarithmic surface pressure and surface geopotential) are spherical harmonics. For approximations by spherical harmonics the spatial discretization of the governing equations of the dynamical core of the model does not take place on an actual mesh with grid points. Spherical harmonics are waves on the sphere, i.e. globe, that vary in

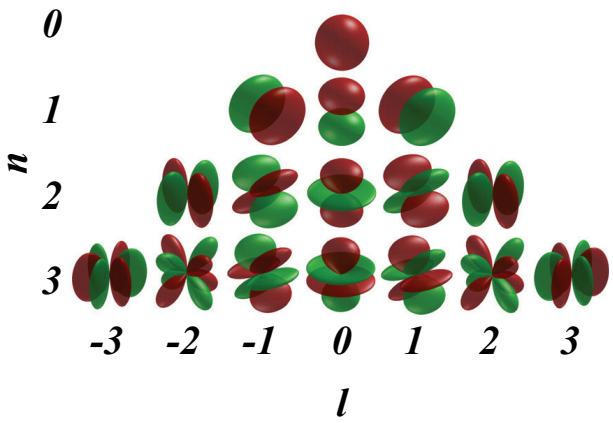


Figure 2.4: Illustration of spherical harmonics for zonal wave numbers $l = -3, ..., 3$ (left to right), meridional index $n = 0, ..., 3$ (top to bottom) and $N(M) = 3$ with $M = 3$. See text for detail. From `http://en.m.wikipedia.org/wiki/Spherical_harmonics` (19.04.2014)

wave length from very large waves to infinitesimal waves (see figure 2.4). An infinite superposition of theses waves with the appropriate coefficients can represent arbitrary functions on the sphere, as long as certain smoothness conditions are fulfilled by the function (see e.g. *Freeden and Schreiner*, 2009). This is comparable to the representation of sufficiently smooth functions by superposition of trigonometric functions with varying wavelengths and amplitude as is done in the field of Fourier analysis.

Truncating the infinite superpositions at a certain wavelength discards the very small waves and therefore small scale processes but allows the approximation of the solution by a finite number of numerically solvable equations, one for each complex-valued spectral coefficient included in the approximation. The approximation has the general form

$$\nu(x_{lon}, y_{lat}, \eta_p, t) = \sum_{l=-M}^{M} \sum_{n=|l|}^{N(M)} \nu_n^l(\eta_p, t) P_n^l(y_{lat}) e^{im\, x_{lon}}. \tag{2.14}$$

The function $\eta_p = \eta_p(p, p_s)$ is a monotonic function of the pressure $p$ and the surface pressure $p_s$ with

$$\eta_p(0, p_s) = 0 \quad and \quad \eta_p(p_s, p_s) = 1, \tag{2.15}$$

i.e. $\eta_p$ is zero at the top of the atmosphere and 1 at the surface. In equation (2.14) $\nu$ is the respective discretized variable, $l$ is the zonal wave number, $n$ the meridional index, the $P_n^l$ are associated Legendre functions, $i$ is the imaginary unit, and the $\nu_n^l$ are the complex-valued spectral coefficients (see *Giorgetta et al.*, 2013). $M$ is the truncation of the zonal wave number and $N(M)$ the appropriate truncation of the meridional index. Both are chosen in such a manner that a triangular truncation is applied for $n$ and $l$. The vertical discretization takes place on specifically defined discrete pressure levels. For further details on the formulation of the governing equations for temperature, divergence and vorticity (i.e. horizontal wind velocities), logarithmic surface pressure and surface geopotential as well as their spectral discretization in the horizontal and the finite difference scheme used for the vertical discretization, see *Giorgetta et al.* (2013).

Aside from the (dry) dynamical core, which uses the spherical harmonics approximation, the changes in atmospheric mixing ratios (i.e. humidity) concerning the different atmospheric water species are computed in grid point space. This holds true for the different parameterization schemes as well, as parameterized tendencies are generally also computed in grid point space. To this end, transformations between the spherical harmonics space and a grid point space of comparable resolution are used to supply the parameterizations with applicable representations of the prognostic variables in grid point space and afterwards transform the calculated parameterized tendencies back to the spectral space. The temporal discretization in ECHAM6 uses finite difference schemes.

The reason for using the spherical harmonics for the atmospheric model is that there are no complex topographic boundaries aside from the surface that would need to be considered in the atmosphere. Therefore a continuous formulation for the whole globe is adequate. Also, spherical harmonics calculations can be very fast with state of the art algorithms. The same is true for the transformations between grid point space and spectral space. The parameterizations, on the other hand, are computed in grid point space as they estimate sub-grid scale processes by using local mean values of the prognostic variables. Once again, for further information on the parameterizations, the grid point space, and the transformation to and from spectral space, it is referred to *Giorgetta et al.* (2013).

Also included in the ECHAM6 model is the land surface (including a hydrological discharge) model JSBACH, simulating, e.g., soil moisture and river runoff as well as the seasonal cycle of the biosphere. For the current set-up of the coupled system, atmospheric tracers such as the $CO_2$ concentration and aerosols are fixed. The values are approximately those of 1990 for all coupled experiments discussed in this dissertation. More information on the formulation and the performance of the atmospheric model ECHAM6 is provided by *Stevens et al.* (2013).

### 2.2.2. Coupling

One of the major tasks for implementing the coupled system ECHAM6-FESOM was the development of the coupling procedure. Figure 2.5 illustrates the two different meshes used by the two different models, the unstructured triangular grid of FESOM and the Gaussian grid of ECHAM6. It is obvious that there are some issues that need to be addressed.

For one, the two meshes have different resolutions in different regions of the globe. FESOM uses up to 1/4° resolution in the equatorial belt, near coastlines and an even higher resolution in the Arctic around Greenland. The resolution of ECHAM6 on the other hand is about 1.9° everywhere, with effectively increased resolution towards the poles as longitudes converge. The grid set-up of ECHAM6 is T63L47, meaning that spectral truncation is applied at $N(M) = 63$ and that in the vertical 47 levels are used, from the ground up to 0.01 hPa ($\sim$ 80 km) with increased resolution in the boundary layer near the surface, decreasing upwards. Another issue is that the two meshes do not follow the coastlines the same way, with ECHAM6 using a land-ocean mask to determine the percental amount of ocean and land within one grid box. This mask had to be adjusted for the coupling to minimize the discrepancy in total ocean area between the two models.

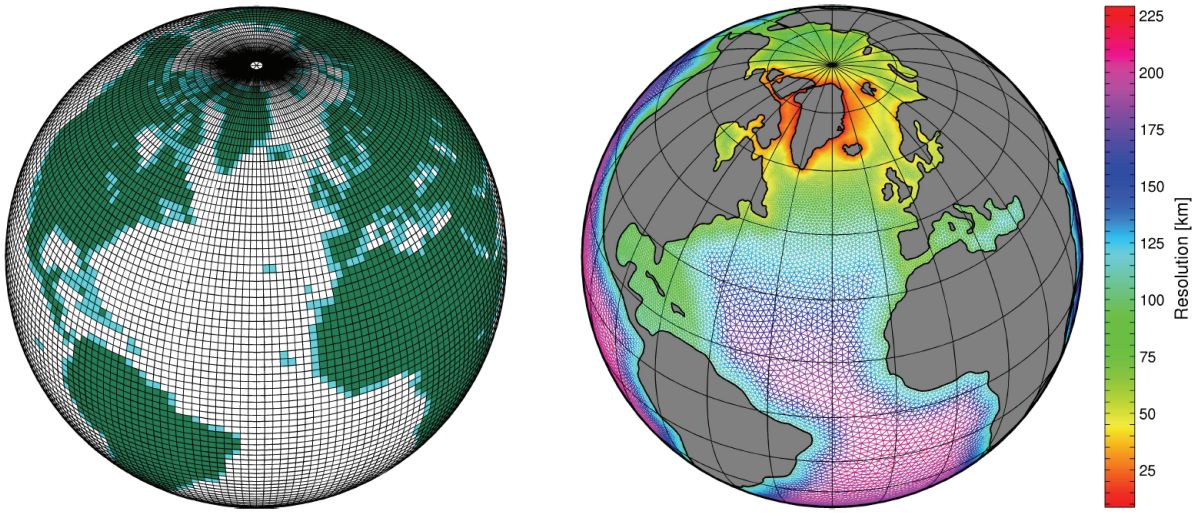


Figure 2.5: Grids used by (left) ECHAM6 (T63 ($\sim$ 180 km) horizontal resolution) and (right) FESOM. For the ECHAM6 grid the areas, where the land fraction is above 50% (between 0% and 50%), are marked dark (light) green. For the unstructured FESOM grid the color coding indicates the resolution (in km). From *Sidorenko et al.* (2014).

The general coupling procedure is described in detail by *Sidorenko et al.* (2014). Generally, the coupling is done by the coupler OASIS3-MCT (*Valcke*, 2013). The fields (FESOM to ECHAM6) and fluxes (ECHAM6 to FESOM) that are coupled are illustrated in figure 2.6. The coupling is done via a third intermediate mesh of approximately the same resolution as the ECHAM6 grid. The intermediate mesh is used by OASIS3-MCT to exchange the information between the two models.

FESOM interpolates from its own mesh to the intermediate mesh. There are two possibilities: If the mesh is finer in FESOM than in the intermediate mesh, all FESOM nodes close to the intermediate mesh node are used to calculate a mean. If the resolution in FESOM is locally similar or coarser than the intermediate mesh resolution, information from the FESOM mesh is linearly interpolated to the respective intermediate mesh node. This is especially the case in some areas of the open oceans or near the coasts, when a grid box of the intermediate mesh covers mainly land. The FESOM fields for the coupling are temporally averaged over the coupling interval (6 hours).

Interpolation between the intermediate mesh and ECHAM6 grid is done by OASIS3-MCT via bilinear interpolation, in both directions. Exchange from the intermediate grid back to the FESOM mesh is done by an inverse distance weighting (*Shepard*, 1968). Also, a redistribution of residual fluxes, either globally or regarding the respective hemisphere, is performed so that total fluxes are conserved. Atmospheric fluxes are accumulated during the coupling interval. The coupling procedure takes place every 6 hours, with FESOM applying a time step of 30 minutes and ECHAM6 a time step of 10 minutes.

The second important task in coupling the two models was the tuning of the coupled system. This was mainly done on the FESOM side, as ECHAM6 was not developed at AWI and it was agreed upon to keep changes to ECHAM6 at a minimum to be able to compare ECHAM6-FESOM to the coupled system of the Max Planck Institute, MPI-ESM-LR (MPI Earth System

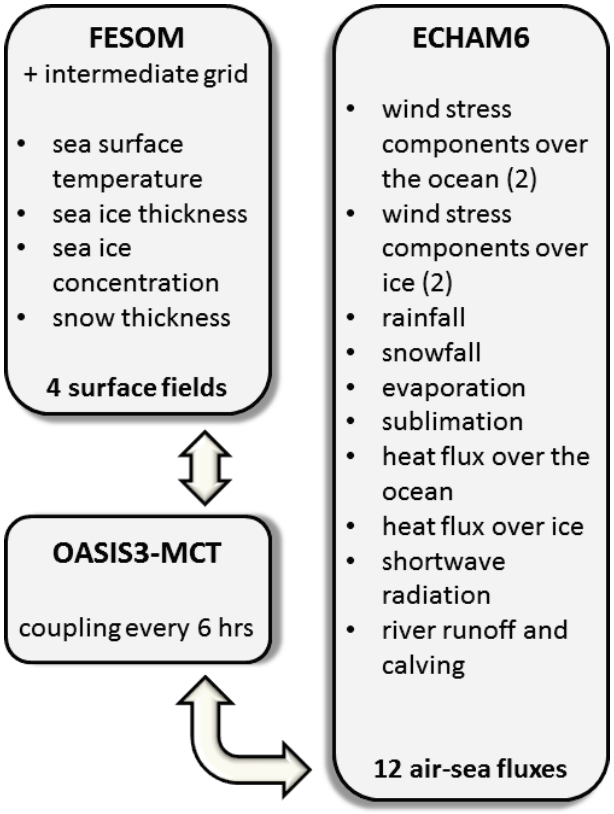


Figure 2.6: Illustration of the coupling procedure between ECHAM6 and FESOM. The 4 6-hourly averaged surface fields (FESOM to ECHAM6) and 12 6-hourly accumulated air-sea fluxes (ECHAM6 to FESOM) are a mapped between the two components at 6-hourly intervals making use of an intermediate grid and the OASIS3-MCT coupler. From *Sidorenko et al.* (2014).

Model Low Resolution), which uses the same atmospheric model but the MPI (sea ice–) ocean model (MPI-OM). One of the main motivations for developing ECHAM6-FESOM was to develop a tool that makes it possible to compare the effect of the variable ocean resolution of FESOM with the rather uniform resolution of most other ocean models (such as the MPI-OM) used in coupled climate systems. FESOM uses a discretization method that is computationally more expensive than other methods, but has the advantage of consistently implemented local refinements that can be rather arbitrarily placed. Simulations with ECHAM6-FESOM might prove that this advantage compensates for the additional computational costs.

### 2.2.3. Model performance[7]

After the model was set up, a long control integration was initialized to investigate the quality of the simulated model climate compared to observations and reanalysis at hand. This was done in two separate parts, one dealing with the quality of the main climate (*Sidorenko et al.*, 2014) for 350 years of (coupled) integration, the other dealing with the quality of the simulated climate variability (*Rackow et al.*, 2014), with the integration extended to 1500 years. As ECHAM6-

[7]The results of this section are based on the article *Towards multi-resolution global climate modeling with ECHAM6-FESOM. Part I: model formulation and mean climate* under review for *Climate Dynamics* (*Sidorenko et al.*, 2014).

FESOM is the model used in chapters 4 and 5, the following section give a short overview over the oceanic and atmospheric mean climate performance of the coupled system.

The triangular grid that was used for the climate integration is relatively coarse and exhibits only moderate mesh stretching factors. This grid was chosen to be able to compare ECHAM6-FESOM not only to observations but also to other climate models with a comparable oceanic resolution. However, such a grid configuration does not make excessive use of the capability of FESOM to finely resolve regions of specific interest. This limits the exploitation of the true potential of FESOM.

### Atmosphere

Exemplary, to give a feeling for the quality of performance of the atmospheric simulation, figure 2.7 shows mean 2-meter temperature (averaged over 300 years) for boreal winter (DJF) and summer (JJA) simulated by ECHAM6-FESOM as well as the difference to ERA-40 reanalysis (years 1957-2002, *Uppala et al.*, 2005).

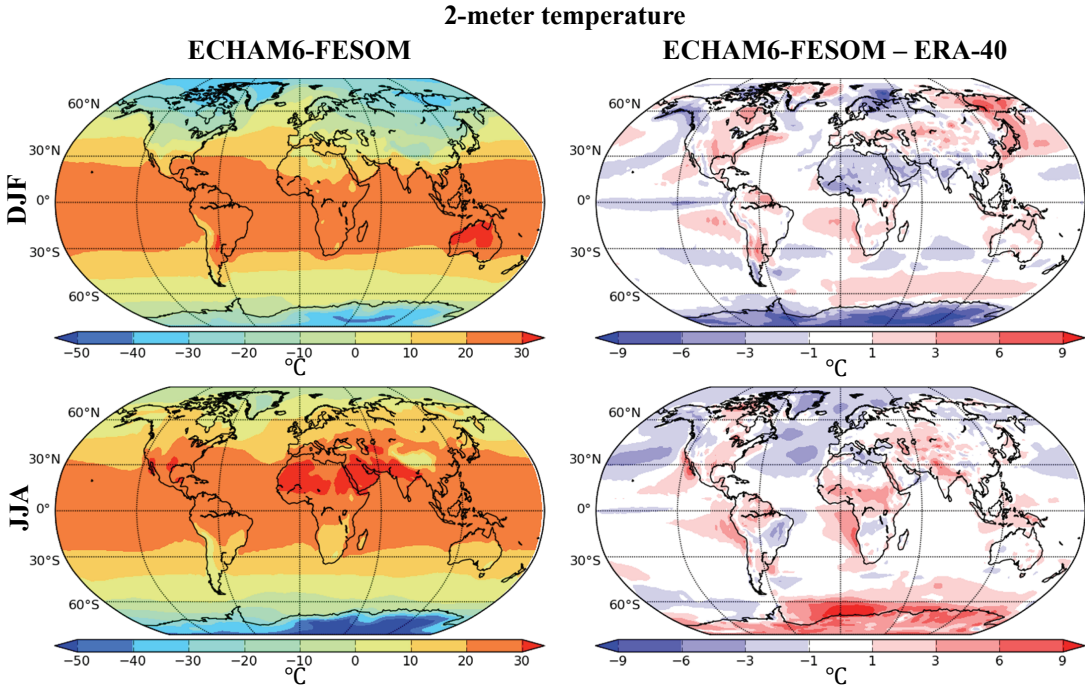


Figure 2.7: Top left: Simulated boreal winter (DJF) climatological 2-m temperature (°C) from ECHAM6-FESOM. Top right: Difference in 2-m temperature between ECHAM6-FESOM and the ERA-40 reanalysis (*Uppala et al.*, 2005). Bottom row: The same as for the top row, except for boreal summer (JJA). From *Sidorenko et al.* (2014).

Generally, the simulations of mean 2-meter temperature are for most regions rather accurate with an error of about 1 K when compared to the reanalysis. Also, biases are quite similar to the biases of the MPI-ESM-LR model. The excessive bias over Antarctica is also present in other state of the art models such as MPI-ESM-LR (*Stevens et al.*, 2013) and HadGEM2 (*Collins et al.*, 2011) and might also be partly caused by biases found in the reanalysis data itself (*Sidorenko et al.*, 2014). Noticeable is also the cold bias in the Barents sea and northern

North Atlantic, where an excessive sea ice cover is simulated especially during the boreal winter months. Shortcomings in the simulation of the North Atlantic circulation are partly responsible for those biases in 2-meter temperature. Another general aspect worth mentioning is the fact that ECHAM6-FESOM simulates a climate with constant 1990 $CO_2$ forcing, whereas the reanalysis data from 1957 to 2002 reflects a climate under changing $CO_2$ concentrations. For a more thorough discussion of the atmospheric performance of ECHAM6-FESOM, see *Sidorenko et al.* (2014), where aside from 2-meter temperature mean fields for precipitation, cloud cover, radiation, winds and 500-hPa geopotential height are discussed.

Table 2.1: Modified performance index for ECHAM6-FESOM in five different regions (see text and *Sidorenko et al.*, 2014). Values below 1 indicate that a model performs better, above 1 indicate worse performance than the average of five CMIP5 models (MPI-ESM-LR, HadGEM2, CCSM4 (*Gent et al.*, 2011), GFDL CM3 (*Griffies et al.*, 2011), and MIROC-ESM (*Watanabe et al.*, 2011)). Adjusted from *Sidorenko et al.* (2014).

| Model | 60-90°S | 30-60°S | 30°N - 30°S | 30-60°N | 60-90°N |
|---|---|---|---|---|---|
| ECHAM6-FESOM | 0.93 | 0.86 | 0.84 | 0.79 | 0.90 |

In addition to the analysis of single atmospheric fields, table 2.1 shows performance indices for the simulated atmosphere. These evaluate the mean absolute error of the model compared to different atmospheric reanalysis and observational data and normalize it with the average over the mean absolute error of five other state of the art global climate models. In cases where ECHAM6-FESOM performs better than the mean of the other models, the value is below 1. It is 1 if they perform equally good or bad and it is greater than 1 if ECHAM6-FESOM performs worse. The performance indices are calculated separately for different regions of the globe. In general, ECHAM6-FESOM performs slightly better than the mean of the five models (see *Sidorenko et al.*, 2014, for more details).

### Ocean and model trend

When considering the performance of the ocean simulation, and the climate in general, it is of interest to know whether the simulated mean is in equilibrium or exhibits some form of drift. The latter would indicate that the system needs more time to end up in a balanced climatic mean state. Figure 2.8 illustrates the changes in mean potential ocean temperature and the imbalance of heat fluxes at the ocean surface. If the system were in equilibrium, mean temperatures would not change on longer time scales and the global mean fluxes would be zero. The imbalance in fluxes and increase of ocean temperature illustrate that the system is still drifting. From an extended integration carried out with the coupled model for the analysis of climate variability (see *Rackow et al.*, 2014) we know that the drift is slowing down and an exponential function can be fitted to the global mean potential temperature with rather high accuracy. The exponential fit suggests a deep ocean equilibration time scale of about 800 years.

In general, it is not uncommon for a model to drift during the first couple of hundred years.

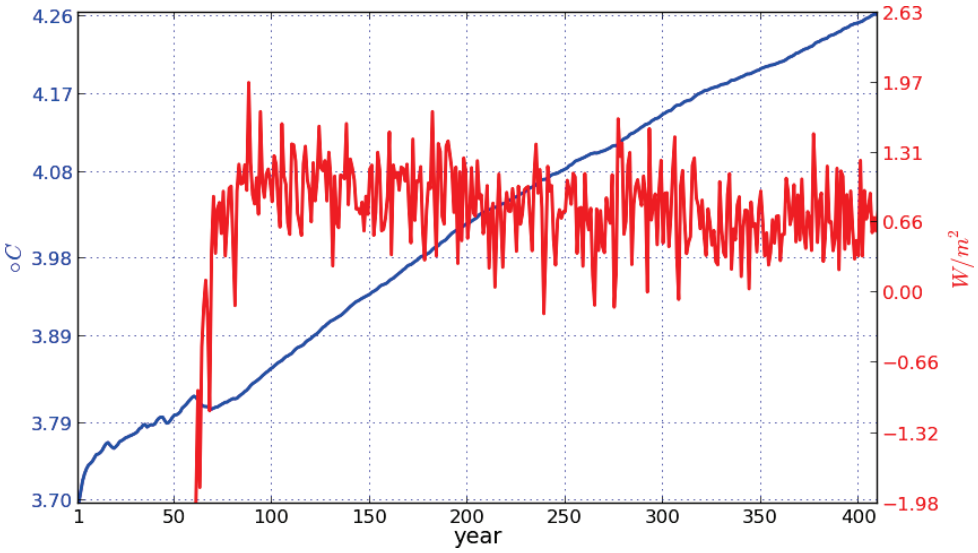


Figure 2.8: Time series of the global average of potential ocean temperature (°C; blue line) and of the global net residual heat flux (including all components) at the ocean surface (W m$^{-2}$; red line). In the time series for the potential temperature 60 years of an ocean-only spin-up are included. From *Sidorenko et al.* (2014).

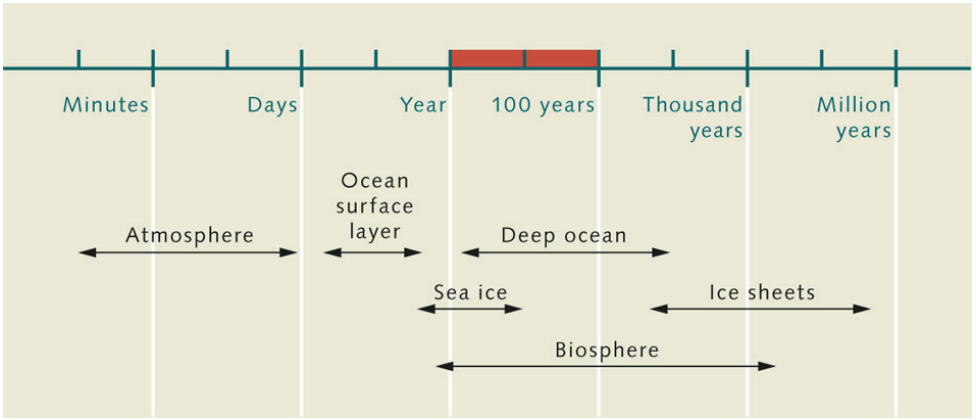


Figure 2.9: Illustration of the time scales of the different components of the Earth system. From *WOR* (2010).

The initial ocean state[8] is only an approximation of the actual state of the real system. Also, the model does not exactly represent the real climatic state but simulates its own model climate that, as would be desirable, is close to what is actually observed. But due to the very long time scales for water mass changes in the deep ocean (centuries to millennia, see figure 2.9), it takes a long time for the model to reach its own climate, even from slightly deviating initial conditions. And it has to be kept in mind that the initial conditions for the ocean rely on observations for a quite short time period in which there has been a trend in atmospheric $CO_2$ concentrations, whereas the model uses constant annual mean atmospheric $CO_2$ forcing.

Figure 2.10 illustrates the changes in salinity and potential ocean temperature from the surface down to the deep ocean, averaged for the global oceans. A freshening and cooling of the

[8] 60 years of FESOM spin-up are conducted under Common Ocean Reference Experiment (CORE), version 2 atmospheric forcing (*Large and Yeager*, 2009) before FESOM is coupled to ECHAM6.

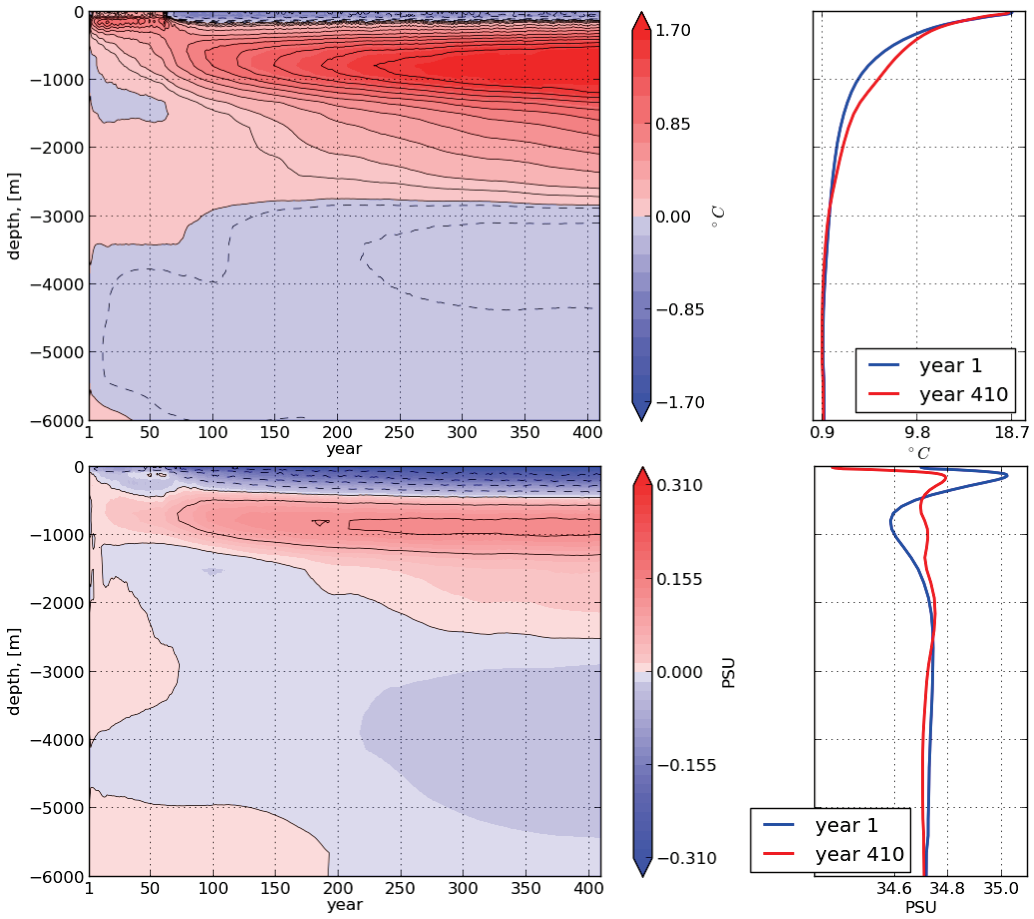


Figure 2.10: Top left: Hovmöller diagram illustrating the changes in the depth profile of the global potential ocean temperature (°C). Shown are the departures from the Polar Science Center Hydrographic Climatology (PHC, *Steele et al.*, 2001). Top right: Depth profile of potential ocean temperature for PHC climatology (blue line) and ECHAM6-FESOM model year 410 (red line). 60 years of an ocean-only spin-up are included. Bottom row: The same as for the top row, except for ocean salinity (PSU). From *Sidorenko et al.* (2014).

upper ocean can be detected in the simulation, while in the mid-depth temperatures and salinity increases. As discussed in *Sidorenko et al.* (2014) this is primarily due to respective changes in the Atlantic ocean, especially in the northern hemisphere (see their figures 12 and 13).

This might be one of the causes for periodic, multi-decadal freezing events occurring in the Labrador sea during boreal winter, accompanied by locally reduced mixed layer depth, reduced sea surface height in the subpolar gyre, and increased fresh water content in the Labrador sea (see figure 2.11). Reasons for this coupled phenomenon in ECHAM6-FESOM are currently still investigated. A hypothesis on how these oscillations might take place is given in *Sidorenko et al.* (2014). In addition, a more complete discussion on simulated ocean circulations and characteristics, as well as global heat transports can be found in *Sidorenko et al.* (2014).

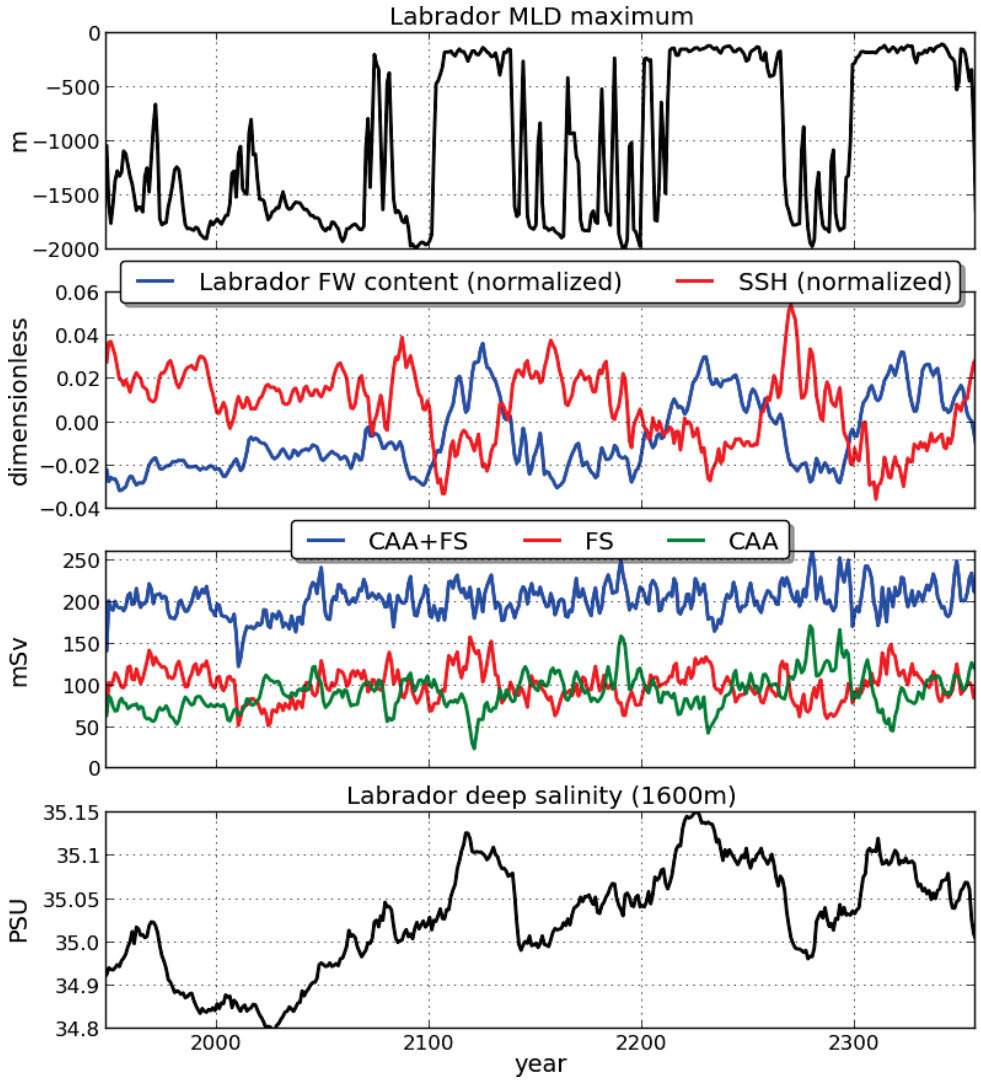


Figure 2.11: From top to bottom: time series of the annual maximum of the mixed layer depth in the Labrador Sea (m); normalized annual mean sea surface elevation (red) and fresh water content (blue) in the Labrador Sea; annual mean exports of freshwater across Davis Strait (green), Fram Strait (red) and the sum of both (blue) (mSv); annual mean deep salinity (at 1600 m depth) in the Labrador Sea (PSU). From *Sidorenko et al.* (2014).

### Sea ice

Of great interest for the applications of the stochastic sea ice parameterization in ECHAM6-FESOM is the simulated sea ice distribution shown in figure 2.12. Sea ice concentration in March is overestimated in the Labrador, Greenland and Barents Sea when compared to passive microwave satellite data (climatology from 1981-2010) from the National Snow and Ice Data Center (NSIDC), University of Colorado, Boulder[9]. Still, distributions "are similar to reanalysis and observational estimates" as noted by *Sidorenko et al.* (2014). This is true for the northern and southern hemisphere. Especially the observed large ice thicknesses north of Greenland and the Canadian Arctic Archipelago are well represented. Also, values of integrated quantities such

[9] `http://nsidc.org/cryosphere/sotc/sea_ice.html` (25.04.2014)

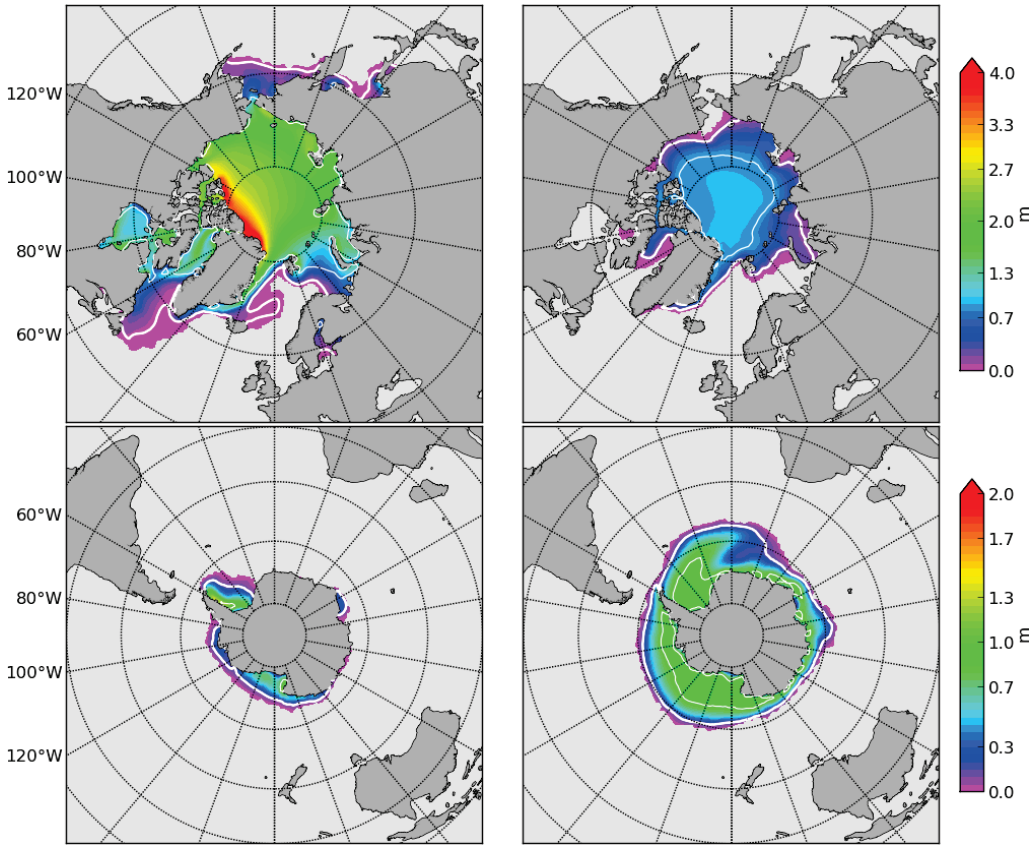


Figure 2.12: Simulated mean sea ice thickness (m) in (left) March and (right) September for (top) the Northern Hemisphere and (bottom) the Southern Hemisphere, averaged over 300 years of the coupled simulation. The thick (thin) contours indicate a mean sea ice concentration of 15% (85%). From *Sidorenko et al.* (2014).

as total Arctic and Antarctic sea ice extent seem reasonable when compared to observations (see *Sidorenko et al.*, 2014).

One thing that needs to be mentioned in this context, though, is that the area of the Arctic Ocean is in the current mesh configuration not accurately represented, leading to a reduced total ocean area (and therefore, potentially, sea ice area) of around 10% due to coastal mismatches in the Canadian Arctic Archipelago and along the coast of Siberia. Nevertheless, ECHAM6-FESOM seems well suited for studies concerning the effects of changes in sea ice parameterizations on the simulated sea ice distributions and, generally, the climate in the high latitudes.

Another issue that needs to be addressed, is the effect of the oscillations of mixed layer depth anomalies in the Labrador Sea mentioned before (see figure 2.11). Currently these multi-annual to multi-decadal phenomena in the simulations are not predictable years or decades ahead. The resulting large interdecadal variability in the northern North Atlantic sea ice concentrations and thicknesses as well as mixed layer depth poses a problem when it comes to analyzing signals of the stochastic ice strength perturbations. As discussed in chapter 4, the impact of those perturbations is rather small on the year to year scale, while the background noise due to

internal model variability is comparatively large in ECHAM6-FESOM. Therefore, integrations in the coupled set-up had to be extended and integrated longer than originally planned to see the influence of the stochastic ice strength perturbations.

## 2.3. Ensemble simulations

Generally, in a fully coupled climate model, due to the presence of the atmospheric component, small differences between otherwise identical model configurations (e.g. perturbations in the initial or boundary conditions, a slightly differing choice of parameter sets or any stochastic aspect of the model) will very quickly lead to model states that differ quite considerably. This is caused by the very fast, chaotic and nonlinear nature of the atmospheric model (and also the "real" atmosphere), which makes it very difficult to give meaningful weather forecasts beyond a few weeks time (depending somewhat on the region and the stability of the current weather situation, i.e. the season and atmospheric state). But due to the coupling between the atmosphere and other, slower components of the climate system (see figure 2.9), in some regions (e.g. over the oceans) some atmospheric variables (e.g. near surface temperatures) diverge somewhat slower, especially when compared to the interannual variability in the respective region. The latter is a measure for how variable the atmosphere is at a given location (or rather, how variable it has been in the past). As long as the ensemble spread stays below this interannual variability, the ensemble members have not reached a level where they actually just sample all possible atmospheric or oceanic states. In other words, it can still be information gained from the ensemble. A forecast with more skill then just based on statistical inference of climatic records is possible. For measures of potential predictability, where ratios of ensemble spread to interannual variability are investigated, see e.g. *Pohlmann et al.* (2004).

The development of spread within an ensemble can depend on very different factors. There is the location under consideration and the variable of interest. It also depends on the method that is used to generate the ensemble, such as the specific initial perturbation technique that is applied. Furthermore, it depends on the initial state from which the ensemble is initialized. Some initial states are more stable than others, meaning that the ensemble members will diverge less rapidly when started at or near this state. It is therefore necessary, if one is estimating the potential of predictions by means of ensemble simulations, to sample a variety of different initial states to be able to make a conclusion that is not only valid for a very specific atmospheric, oceanic or climatic state. Multiplying the sampled initial states by the number of members per ensemble—which already needs to be reasonable large to sample the ensemble spread with sufficient accuracy—makes studies of potential predictability computationally very costly. But many initial dates and sufficient ensemble sizes are necessary to reach relevant and statistically significant results.

In this context three major decisions have to be made:

- A perturbation strategy has to be chosen that samples some kind of uncertainty. This will create the ensemble members, each one slightly differing from the others, and will generate ensemble spread.

- The size of the ensemble has to be chosen, balancing an accurate representation of ensemble spread (owing to a high number of members) with computational costs, which increase linearly with an increasing amount of ensemble members.

- Different start dates need to be chosen. These should sample the same time of the year, but should be more or less independent. This can be achieved by choosing the same calender day but from different years, with the years being sufficiently far apart to guarantee independence. The latter is especially important for the sea ice and ocean state, which exhibit considerable memory that can extent over many years.

To illustrate the concept, in the following one of the atmospheric perturbations applied in chapter 5, originally introduced by *Magnusson et al.* (2009), is described. To a given atmospheric state $XX$, e.g. from the first of January of some more or less arbitrary model year, a perturbation is generated by choosing randomly two other atmospheric states from the same calender day but from different years, $YY$ and $ZZ$. From these two states the main dynamical variables (three-dimensional temperature and wind fields) are subtracted, one from the other, and multiplied by a factor of 0.1 to reduce the amplitude of the perturbation. This perturbation is then added to the respective fields of the atmospheric state $XX$ to generate the new initial field. Exemplary, for the temperature filed $T$ the new perturbed temperature field $T_{XX}^{new}$ is given by

$$T_{XX}^{new} = T_{XX} + 0.1 \cdot (T_{YY} - T_{ZZ}). \tag{2.16}$$

Figure 2.13 illustrates the spread evolution produced by this kind of ensemble with 10 members for one start date and for 2-meter temperature. The spread is here defined as the unbiased standard deviation of the ensemble for each grid point. Ensemble spread develops very rapidly over land, whereas the growth is much smaller over the ocean areas. This is due to the fact that the sea surface temperatures of the ocean are changing much slower than land surface temperatures, as the ocean has a much larger specific heat capacity and changes caused by the perturbations from the mean state are developing much slower. The ocean has a much longer memory than the atmosphere and, through coupling, this memory is to some extend transfered to the lower atmosphere as well.

As soon as more than one start date is taken into account, the standard deviations calculated for each ensemble start date are averaged to obtain a mean spread evolution for the perturbation technique under consideration. This mean ensemble spread is in chapter 5 compared to the interannual standard deviation calculated from a long control integration, for different times of the year, to allow for an estimation of sea ice predictability, using different perturbation strategies.

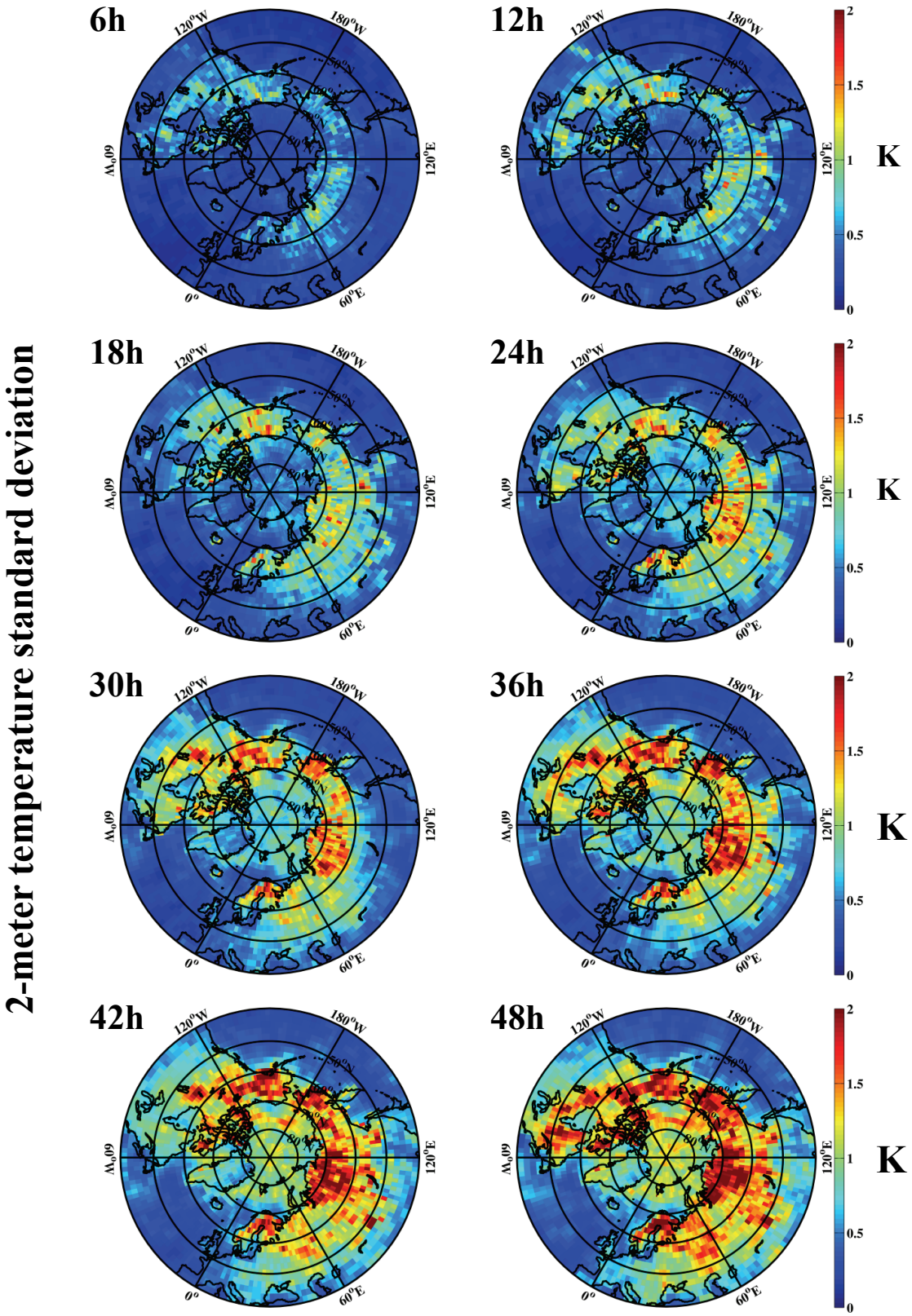


Figure 2.13: Illustration of the evolution of 2-meter temperature ensemble standard deviation for the first two days. Ensemble size is 10, with initialization on the 1st of January, 00:00 UTC. The ensemble is generated by atmospheric initial perturbations using equation (2.16).

# 3. Effects of stochastic ice strength perturbation on Arctic finite element sea ice modeling[10]

[10] This chapter has been published under the title *Effects of stochastic ice strength perturbation on Arctic finite element sea ice modeling* in the *Journal of Climate* (see reference *Juricke et al.*, 2013). The original layout of the article was changed to match the layout of the dissertation. No changes to the text were made, though, except for referencing to figures, equations and tables as well as citations. Those have been changed to match the respective layout in the rest of the dissertation. In addition, the bibliography and the appendix of the publication have been merged with the bibliography and the appendix of the dissertation, respectively. The abstract of the article was retained. My contributions to the article include all the necessary implementations and model adjustments, the experimental set-up and initialization as well as monitoring of the simulations. I carried out all of the diagnostics and the plotting of the results. The concept for the experimental set-up as well as the evaluation, assessment, and interpretation of the results were developed and conducted in discussions with my coauthors Peter Lemke, Ralph Timmermann and Thomas Rackow. They have also corrected my original manuscript before submission to the journal. In addition, I would like to point to the acknowledgments at the end of the chapter.
Please excuse any remaining inconsistencies with the other chapters of this dissertation originating from the general layout of the original publication, including differences in spelling, figure layout, acronyms, equations and phrasing.

**Abstract**

The ice strength parameter $P^*$ is a key parameter in dynamic/thermodynamic sea ice models that cannot be measured directly. Stochastically perturbing $P^*$ in the Finite Element Sea Ice–Ocean Model (FESOM) of the Alfred Wegener Institute aims at investigating the effect of uncertainty pertaining to this parameterization. Three different approaches using symmetric perturbations have been applied: 1) reassignment of uncorrelated noise fields to perturb $P^*$ at every grid point, 2) a Markov chain time correlation, and 3) a Markov chain time correlation with some spatial correlation between nodes. Despite symmetric perturbations, results show an increase of Arctic sea ice volume and a decrease of Arctic sea ice area for all three approaches. In particular, the introduction of spatial correlation leads to a substantial increase in sea ice volume and mean thickness. The strongest response can be seen for multiyear ice north of the Greenland coast. An ensemble of eight perturbed simulations generates a spread in the multiyear ice comparable to the interannual variability of the model. Results cannot be reproduced by a simple constant global modification of $P^*$.

## 3.1. Introduction

Because of the diversity in spatial and temporal scales of physical processes and the limited resolution in climate models, parameterizations are generally needed to describe the influence of small-scale processes on large-scale flows. This influence is mostly considered in terms of the mean of the models' prognostic variables, while the effect of unresolved scales on higher-order moments such as the variance is frequently ignored. Because of the numerical implementation of the parameterizations, model errors arise. Especially in numerical weather prediction (NWP) the idea of applying probabilistic methods to previously deterministic models to address such model errors and to increase the model spread has become a well-established research topic in recent years. As summarized by *Palmer* (2012), the inclusion of stochastic parameterizations may help to better estimate model uncertainty and reduce biases or even the uncertainties themselves. In this context, *Buizza et al.* (1999) applied a stochastic perturbation to the parameterized tendencies in their European Centre for Medium-Range Weather Forecasts (ECMWF) Ensemble Prediction System (EPS) to address model error within the parameterizations of physical processes. This successfully increased the ensemble spread. This was followed by a more sophisticated spectral stochastic kinetic energy backscatter scheme (SSBS) (*Berner et al.*, 2009), based on stochastic perturbations of streamfunctions.

Another approach that also aims at the inclusion of model error within the physical processes in NWP has been applied by *Lin and Neelin* (2000), *Bright and Mullen* (2002), and *Li et al.* (2008). These authors stochastically perturbed parameters of a certain parameterization scheme to account for uncertainties that are related to a deterministic parameter choice, as some of the parameters do not have an obvious analog in nature. A first-order Markov process is used by *Lin and Neelin* (2000) to perturb the convective available potential energy within the parameterization of deep convection. The same concept of temporal correlation is applied by *Bright and Mullen* (2002) to perturb the grid-scale vertical velocity at the lifting condensation level within the cumulus parameterization and the critical bulk Richardson number within the planetary boundary layer scheme. *Li et al.* (2008) employed a more sophisticated parameter perturbation in their convective and condensation schemes. They applied a first-order Markov process to create random numbers as spectral coefficients of spherical and Fourier harmonics expansions in the horizontal and vertical direction, respectively. Thereby, spatial correlation is introduced to the stochastic parameter perturbations.

Sea ice models contain several sensitive parameters that need to be chosen carefully and are used to tune the model. Early studies—for example, by *Stössel et al.* (1990), *Owens and Lemke* (1990), and *Harder* (1996)—show that the ice strength parameter $P^*$ of the viscous–plastic sea ice rheology introduced by *Hibler* (1979) is among the important parameters within the sea ice dynamics, together with parameters such as the drag coefficients for the momentum fluxes between the ice and the ocean and atmosphere. Sensitivity experiments carried out prior to this study have confirmed the importance of $P^*$ when it comes to sea ice distribution and drift patterns in our model. The quantity $P^*$ determines the internal ice strength; for higher values of $P^*$ the ice is less easily deformed in case of a convergent drift. Changes in the sea ice drift influence the advection of sea ice, which has an impact on the ice thickness distribution,

especially on the formation of pressure ridges that often accrete to multiyear ice, and on the ice concentration. As sea ice plays an important role for the surface albedo and has a strong effect on the transport of heat and momentum between atmosphere and ocean, changes in the ice coverage influence the thermodynamics of the model and in coupled models affect both the ocean and the atmosphere components. So, the parameter $P^*$ has an impact not only on the sea ice drift itself and on the thickness distribution, but also on aspects such as the Arctic freshwater export linked to sea ice drift through the straits, the heat budget of the ocean, sea ice production rates, and bottom water formation. As a consequence, a proper representation of the sea ice dynamics is necessary for accurate predictions of climate in the high latitudes.

The value of $P^*$ is only weakly constrained, however, as it cannot be measured directly and may vary strongly in time and space (*Harder and Fischer*, 1999). *Tremblay and Hakakian* (2006) estimated upper and lower bounds for $P^*$ based upon the deformation law of *Hibler* (1979) using satellite data for sea ice drift and reanalysis data for sea level pressure. Even though they found values of the same magnitude as other studies that used in situ measurements or drift buoy data, the derived values vary quite considerably. They also state that the time averaged atmospheric forcing used in any given model as well as the choice of parameters such as the air-ice drag coefficient may have a strong influence on the appropriate value of $P^*$. This leads to further uncertainties. Because of these uncertainties and the global averaging of a highly variable parameter, $P^*$ seems a good first candidate for applying a stochastic approach as a method to tackle the model error connected to the physical process of subgrid-scale sea ice deformation and to investigate the changes arising in the sea ice thickness distribution due to the nonlinearity of the parameterization.

In this work we present a first approach to include uncertainty estimates in a sea ice model by the use of stochastic parameterizations. We introduce a new suite of schemes to stochastically perturb the ice strength parameter $P^*$ and demonstrate that this symmetric parameter perturbation leads to an increase in total Arctic sea ice volume and a distinct change in the local Arctic sea ice thickness distribution. Adding first temporal and then spatial correlation to the perturbations leads to an increasing impact on the Arctic sea ice coverage. The spatial correlation in particular will prove to be of great importance in the perturbation scheme. While the influence of the seasonal cycle reduces the effects of the perturbed sea ice strength parameterization for first-year ice and along the ice edge, the multiyear ice exhibits a strong sensitivity to the new scheme and tends to increase considerably in thickness. The Arctic monthly mean sea ice thickness in an ensemble simulation shows an increase of about +5% in January and about +11% in September compared to the reference simulation. The spread in multiyear ice thickness generated by the parameter perturbation is comparable to the interannual variability of the model and may give an indication for a range of values for $P^*$ to be used in data assimilation studies. The range chosen for most perturbations in this study is $P^* \in (5000 \text{ N m}^{-2}, 35000 \text{ N m}^{-2})$.

This paper has the following structure. In section 3.2 we will give a short overview of the Finite Element Sea Ice–Ocean Model (FESOM) (*Wang et al.*, 2008; *Timmermann et al.*, 2009; *Sidorenko et al.*, 2011) of the Alfred Wegener Institute for Polar and Marine Research (AWI) and the sea ice rheology that is used by the model. Section 3.3 describes the three different parameter perturbation approaches that have been studied: one with no spatial correlation

between any two nodes and just a simple form of temporal correlation, a second one again with no spatial correlation but a temporal correlation given by a first-order Markov process, and finally a third version featuring the temporal correlation according to the Markov process of the second approach and also a spatial correlation between nodes with common neighbor nodes. Results of the three approaches in comparison with a deterministic reference simulation and with observations of sea ice draft and concentration will be analyzed in section 3.5, focusing on the Arctic Ocean. Finally, section 3.6 will provide conclusions and a short outlook for future work.

## 3.2. Model background

We use the Finite Element Sea Ice–Ocean Model to perform simulations of the Arctic sea ice. Spatial discretization of the model is implemented via finite elements on a triangular grid at the ocean surface and a tetrahedral grid with $z$ levels for the three-dimensional ocean modeling. The ocean model discretizes the momentum, heat, salt, and mass continuity equations based on the hydrostatic assumption and is coupled to a sea ice model. The model setup in this study is forced by the interannual varying Common Ocean Reference Experiment (CORE), version 2 atmospheric dataset by *Large and Yeager* (2009). FESOM under the normalized year forcing of CORE I has been evaluated and compared to other models by *Sidorenko et al.* (2011). Further details on FESOM have been presented by *Wang et al.* (2008) and *Timmermann et al.* (2009).

In the sea ice model the prognostic variables effective (mean) sea ice thickness $h_{ice}$, lateral sea ice velocities $u_{ice}$ and $v_{ice}$, and sea ice concentration $A$, as well as mean snow layer thickness $h_s$, are calculated. For this purpose, prognostic equations for $h_{ice}$, $h_s$, and $A$ describing the rate of change due to freezing and melting processes and advection are solved. The dynamical part of the model describes the rate of change in the sea ice velocities via the momentum balance (*Timmermann et al.*, 2009). Sea ice and ocean models use the same surface mesh, which makes their coupling straightforward. The global finite element mesh is locally refined in the Arctic and especially along the coastlines and in straits, the resolution ranging from over 300 km in the Pacific Ocean to about 11 km at the coasts. The mesh of the Arctic region can be seen in figure 3.1. The time step in this study is $\Delta t = 1\,\mathrm{h}$.

The momentum equation for the sea ice velocities discretized in FESOM is

$$m\frac{\partial \vec{\mathbf{u}}_i}{\partial t} = \vec{\boldsymbol{\tau}}_{air} + \vec{\boldsymbol{\tau}}_{ocean} - mf\vec{\mathbf{k}} \times \vec{\mathbf{u}}_i - mg\nabla\eta_o + \vec{\mathbf{F}}_{int} \tag{3.1}$$

with $m$ being the mass per unit area, $\vec{\mathbf{u}}_i$ the horizontal sea ice velocity vector, $\vec{\boldsymbol{\tau}}_{air}$ and $\vec{\boldsymbol{\tau}}_{ocean}$ the atmospheric and oceanic stress, respectively, $f$ the Coriolis parameter, $\vec{\mathbf{k}} = (0, 0, 1)$, $g$ the gravitational acceleration, and $\eta_o$ the sea surface height of the ocean. For this study the important term in equation (3.1) is the last term on the right-hand side that describes the internal forces $\vec{\mathbf{F}}_{int} = (F1, F2)$ within the sea ice.

For the computation of the internal stress FESOM offers the classical viscous–plastic rheology introduced by *Hibler* (1979) with adjustments by *Harder* (1996), and alternatively the elastic–viscous–plastic rheology devised by *Hunke and Dukowicz* (1997) following in its implementation

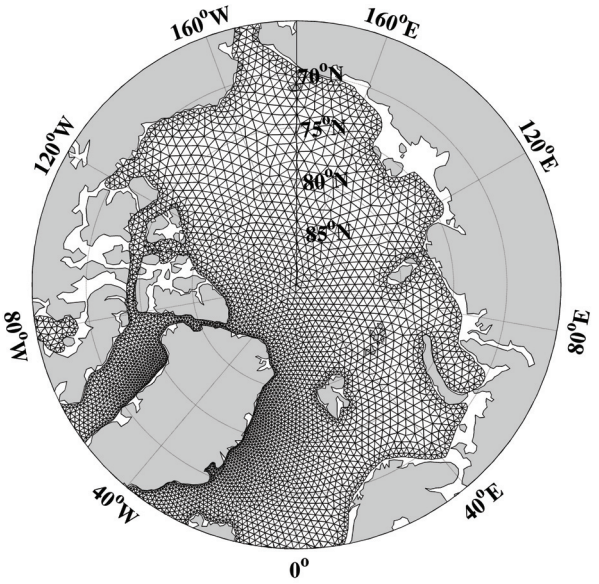


Figure 3.1: Arctic sector of the global mesh used for this study.

the documentation of the Community Ice Code (CICE) model (also known as the Los Alamos Sea Ice Model; *Hunke and Lipscomb*, 2010). The latter has been used for this study. Both rheologies describe the internal forces as the divergence of the two-dimensional stress tensor $\boldsymbol{\sigma}$:

$$F_j = \sum_{i=1}^{2} \frac{\partial \sigma_{ij}}{\partial x_i}, \quad j = 1, 2. \tag{3.2}$$

For the elastic–viscous–plastic rheology the tensor components $\sigma_{ij}$ are described by the differential equations

$$E\frac{\partial \sigma_{ij}}{\partial t} + \frac{1}{2\eta}\sigma_{ij} + \frac{\eta - \zeta}{4\eta\zeta}\sum_{k=1}^{2}\sigma_{kk}\delta_{ij} + \frac{P}{4\zeta}\delta_{ij} = \dot{\epsilon}_{ij}, \tag{3.3}$$

where $\dot{\boldsymbol{\epsilon}}$ is the deformation rate tensor

$$\dot{\epsilon}_{ij} = \frac{1}{2}\left\{\frac{\partial u_i}{\partial x_j} + \frac{\partial u_j}{\partial x_i}\right\}, \tag{3.4}$$

$\eta$ and $\zeta$ are the nonlinear shear and bulk viscosities, respectively, $\delta_{ij}$ is the Kronecker symbol, and $E$ is some elasticity constant (*Hunke and Dukowicz*, 1997).

The ice strength $P$ is given by

$$P = \frac{P_p \cdot \Delta}{\Delta + \Delta_{min}} \tag{3.5}$$

with

$$\Delta = \left[(\dot{\epsilon}_{11}^2 + \dot{\epsilon}_{22}^2)(1 + \frac{1}{e^2}) + 4\frac{\dot{\epsilon}_{12}^2}{e^2} + 2\dot{\epsilon}_{11}\dot{\epsilon}_{22}(1 - \frac{1}{e^2})\right]^{\frac{1}{2}}, \tag{3.6}$$

where $\Delta_{min}$ represents a small regularization value that creates a smooth transition from viscous to plastic regimes, following the idea of *Harder* (1996), and $e$ is the eccentricity of the elliptical

flow curve (i.e., it describes the relation between $\zeta$ and $\eta = \zeta/e^2$).

The important parameterization concerning the perturbations introduced in the next section is that for the sea ice strength given by

$$P_p = P^* \frac{h_{ice}}{A} \cdot \exp(-C(1-A)) \tag{3.7}$$

with the dynamic ice strength parameters $P^*$ and $C$. The viscosities $\eta$ and $\zeta$ also depend linearly on $P_p$.

Equations (3.5) and (3.7), through (3.2) and (3.3), describe the resistance of the sea ice against deformation. For small deformation rates the internal forces increase with rising deformation rates, in a manner that depends on the value given by equation (3.7). But as soon as a limiting value of $\Delta$ is reached, a further increase in deformation rates does not increase the internal forces. The sea ice behaves plastically and, by way of its drift, tends to pile up. Therefore equation (3.7) influences the behavior of sea ice especially in convergent drifts, where $h_{ice}$ and $A$ have an impact on the rate at which the sea ice is deformed and thereby increases in thickness.

This highly nonlinear dependence of internal stresses on ice strength and hence $P^*$ will be analyzed in the following section by a symmetric parameter perturbation.

## 3.3. Parameter perturbation

The stochastic perturbation in this work is applied to the sea ice strength parameter $P^*$ governing the internal forces within the sea ice dynamics. In the purely deterministic version of FESOM the parameter $P^*$ is fixed in time and space at a value of $P^* = P^*_{ref} = 20000\,\mathrm{N\ m^{-2}}$. This does not account for small-scale variations imposed by, for example, different local melting and freezing histories or brine pocket formation. Furthermore, the associated natural variability in space and time around a given mean in sea ice thickness and compactness is not resolved. Some of this variability can be introduced by a symmetric perturbation of $P^*$ around $P^*_{ref}$.

The general approach is based on perturbing $P^*_{ref}$ via

$$P^*(i,j) = (1 + x(i,j)) \cdot P^*_{ref}. \tag{3.8}$$

The indices $i$ and $j$ give the nodal index in space and the time step, respectively. The value $x(i,j)$ is a random value from a preassigned distribution, bounded within some range $-a < x(i,j) < a$, with $0 < a \leq 1$.

For the use in the sea ice rheology in FESOM, nodal values are averaged over elements where rheology calculations take place.

This general kind of parameter perturbation has been used in different parameterizations within atmospheric general circulation models, for example by *Lin and Neelin* (2000) in a convective parameterization or by *Bright and Mullen* (2002) in cumulus and in planetary boundary layer parameterizations. In both studies the random numbers $x(i,j)$ have been correlated in time, but not in space. In this work we will present three different possibilities for the parameter

perturbation in equation (3.8). In the first approach, reassignment of random values will occur after a predefined time interval and there will be no correlation between different nodes. For the second approach the reassignment of random values will be replaced by a time correlation via a Markov process. Finally, the third approach will include a limited correlation in space as well as the correlation in time via a Markov process. In this context, the inclusion of correlation in time and space seems reasonable. Sea ice has a strong memory when it comes to processes such as formation, melting, and deformation, all of which have an impact on the resistance of the ice toward further deformation. And even though small-scale structures such as ridges and leads occur in the ice, there is generally considerable correlation within the spatial ice thickness distribution, which is connected to different ice strength regimes. The relevant parameters of spatial and temporal correlation for the new stochastic schemes will receive their values from references given in section 3.4.

### 3.3.1. Reassignment time step perturbation (RP)

The RP approach is implemented as follows. At the end of each time interval with length $(\Delta t)_{pert}$, every ice-covered node within the model area is reassigned a random number from some distribution. In addition, open ocean nodes that freeze over between those larger time steps receive some random number as well.

Gaussian distributions are widely used for parameter perturbations (*Lin and Neelin*, 2000; *Bright and Mullen*, 2002). The interval for possible values of the random numbers is bounded, however, because $P^*$ has to stay within physically realistic limits. Therefore the traditional Gaussian distribution cannot be used. In this study three different Gaussian-like distributions have been employed. Appendix A gives a short overview over the so-called $x$- and $y$-truncated Gaussian distributions (*Bardsley*, 2007) and a third distribution, which is generated through exponential transformation of a Gaussian distribution.

The important parameters for this first approach are the limit $a$ of the domain of the random number, the reassignment time step $(\Delta t)_{pert}$, the truncated or bounded distribution function used, and the variance of the underlying Gaussian distribution function. Values will be assigned in section 3.4.

### 3.3.2. Markov process time correlated perturbation (MTP)

To include some correlation in time that does not only depend on a reassignment time step, the approach of section 3.3.1 is adjusted. Following *Bright and Mullen* (2002) and *Lin and Neelin* (2000) a Markov process of the general form

$$y(i,j) = \alpha y(i,j-1) + z(i,j) \tag{3.9}$$

is used to keep correlation of the random value $y(i,j)$ at the current time step with the previous one, $y(i,j-1)$, with $y(i,0) = 0$ as initial condition and also $y(i_1, j_1 - 1) = 0$ if $j_1$ is the first ice-covered time step for node $i_1$ after an ice-free period. In equation (3.9) $0 < \alpha < 1$ denotes the memory of the first-order Markov process (i.e., the autocorrelation). As derived in appendix

B,

$$\alpha = 1 - \lambda(\Delta t), \tag{3.10}$$

where $\lambda = 1/\tau$ and $\tau$ is the relaxation time.

The perturbation $z(i,j)$ is an independent Gaussian random number with zero mean. We set the variance of the $z(i,j)$ to

$$\tilde{\sigma}^2 = \sigma^2/(\Delta t)_{pert} \cdot \Delta t, \tag{3.11}$$

with $\sigma$ being comparable to the standard deviation of the Gaussian perturbation used in section 3.3.1, $(\Delta t)_{pert}$ the reassignment time step also used in section 3.3.1, and $\Delta t$ the model time step. Contrary to the approach in section 3.3.1, the perturbations $z(i,j)$ are applied at each time step.

To use the random values produced by equation (3.9) the values need to be transformed into the respective values $x(i,j)$ with limited range. How this is done is also described in appendix B, for all the three possible bounded distributions. Differences in the results of the runs due to the three different corresponding transformations will be discussed in section 3.5.

### 3.3.3. Markov process time and space correlated perturbation (MTSP)

To include some spatial correlation in the perturbation of $P^*$, the random number $z(i,j)$ in equation (3.9) is adjusted as

$$z(i,j) = \frac{\sigma\sqrt{\Delta t}}{\sqrt{(\Delta t)_{pert}}} \left( \xi(i,j) + \sum_{k \in N_i} q(d_{ik}) \cdot \xi(k,j) \right) \left( 1 + \sum_{k \in N_i} q(d_{ik})^2 \right)^{-1/2}. \tag{3.12}$$

Here $\xi(i,j)$ and $\xi(k,j)$ are $N(0,1)$ distributed random numbers, $q(\cdot)$ is a weighting function depending on the distance $d_{ik}$ in meters between the current node $i$ and its neighbor $k$, and $N_i$ is the set of indices of the direct neighbor nodes of node $i$.

Dividing by the square root of the sum in (3.12) normalizes the variance of the random number $z(i,j)$ so that the corresponding random variable is still Gaussian distributed with the variance (3.11) and zero mean.

The weights $q(\cdot)$ are exponential functions given by

$$q(d_{ik}) = e^{-d_{ik}/d_{corr}} \tag{3.13}$$

with some correlation distance $d_{corr}$ in meters.

In this approach the variance of a random variable that corresponds to (3.12) is given by equation (3.11), while the covariance between two nodes is greater zero if they have common neighbors. Otherwise the covariance is equal to zero.

The procedure for transforming the values $y(i,j)$ into the respective values $x(i,j)$ with limited range is the same as for MTP as all variance calculations given in appendix B stay the same.

## 3.4. Model setup

The three different approaches of section 3.3 for the parameter perturbations have been implemented in the framework of FESOM. To analyze the changes caused by the perturbations, a reference simulation REF with fixed parameter $P^* = P^*_{ref} = 20000\,\mathrm{N\ m^{-2}}$ has been spun up for 12 yr. It was continued further and also used to initialize the different test cases for the stochastic perturbations. For the first part of this study we compared the total Arctic sea ice volume and area as well as the monthly mean sea ice thickness and concentration distribution of one realization of each stochastically perturbed model setup with the reference run. Integration time for these sensitivity experiments was 3 yr, starting from 1990.

As will become clear in section 3.5.1, the approach with the strongest impact is MTSP, with Markov process time and space correlated perturbations, which is the reason why the sensitivity studies presented here will focus on this last approach. For the other two approaches, RP and MTP, only one experiment each will be discussed in section 3.5.1. Table 3.1 shows the different model setups, introduces their names, and summarizes their impact on total Arctic sea ice volume and area.

Parameter ranges for the relaxation time $\tau$ follow *Lemke et al.* (1980), where the general idea of the Markov chain has been used to estimate, among other things, relaxation times for sea ice extent anomalies in the Arctic and Antarctic. The lower values of 2 h and 1 day have been tested as well to reduce the temporal correlation considerably.

The range for correlation distances follows estimates of spatial scales for a valid interpretation of the central Arctic sea ice thickness distribution function suggested by *Flato* (1998).

The parameter range $((1-a)P^*_{ref}, (1+a)P^*_{ref})$ for possible values of $P^*$ follows several publications concerning sensitivity studies of $P^*$, among other parameters, within different models (*Owens and Lemke*, 1990; *Harder and Fischer*, 1999). For this study we used from $P^* \in (10000\ \mathrm{N\ m^{-2}}, 30000\ \mathrm{N\ m^{-2}})$ to $P^* \in (3000\ \mathrm{N\ m^{-2}}, 37000\ \mathrm{N\ m^{-2}})$. The value for the variance $\sigma^2$ is matched to the value of $a$ to avoid the danger that the distribution function of the random values becomes too flat after transformation and therefore tends to lose its Gaussian-like shape. Values of $\sigma$ that have been tested but will not be discussed here are 0.25 and 0.5, as similar effects can be generated by changes in other parameters (e.g., $(\Delta t)_{pert}$).

The last parameter that needs to be chosen is $(\Delta t)_{pert}$. We chose values for $(\Delta t)_{pert}$ to be within the range of 1 to 7 days to simulate the differences between the accumulated influence of a diurnal up to a weekly perturbation cycle. Also a value of 1 h has been tested.

For the analysis of an ensemble run in section 3.5.2 we used an ensemble ENS of eight members with the configurations given in table 3.1 for MTSP0. Integration time for the ensemble was 17 yr, also starting from 1990.

In addition, we ran three deterministic experiments with fixed parameter values for $P^*$ (REF1 with 12500 N m$^{-2}$, REF2 with 15000 N/m$^2$ and REF3 with 17500 N m$^{-2}$) for 6 yr, to be able to compare the changes caused by the parameter perturbations in the ensemble with the effect of a uniform reduction of $P^*$.

Table 3.1: Parameter values of the stochastic perturbation for sensitivity experiments. For the MTSP approach only one of the parameters has been changed from one run to another, with the other values fixed at the default values in bold. RP0, MTP0 and MTSP0 are the default cases for the correspondent approaches. Here $\Delta V$ and $\Delta A$ give the corresponding mean changes in total Arctic sea ice volume and area for the time period 1990–1992 for all configurations. All these experiments use a $x$-truncated Gaussian distribution.

| | $\sigma$ | Range of $P^*$ [N m$^{-2}$] | $(\Delta t)_{pert}$ | $\tau$ | $d_{corr}$ [km] | $\Delta V$ [$10^3$ km$^3$] | $\Delta A$ [$10^6$ km$^2$] |
|---|---|---|---|---|---|---|---|
| RP0 | 0.375 | (5000, 35000) | 1 day | −− | – | +0.177 | −0.032 |
| MTP0 | 0.375 | (5000, 35000) | 1 day | 30 days | – | +0.243 | −0.053 |
| MTSP0 | **0.375** | **(5000,35000)** | **1 day** | **30 days** | **100** | +0.566 | −0.142 |
| MTSP1 | **0.375** | (10000, 30000) | **1 day** | **30 days** | **100** | +0.222 | −0.051 |
| MTSP2 | **0.375** | (3000, 37000) | **1 day** | **30 days** | **100** | +0.713 | −0.183 |
| MTSP3 | **0.375** | **(5000,35000)** | 1 h | **30 days** | **100** | +0.580 | −0.137 |
| MTSP4 | **0.375** | **(5000,35000)** | 7 days | **30 days** | **100** | +0.448 | −0.101 |
| MTSP5 | **0.375** | **(5000,35000)** | **1 day** | 2 h | **100** | +0.027 | −0.005 |
| MTSP6 | **0.375** | **(5000,35000)** | **1 day** | 1 day | **100** | +0.254 | −0.049 |
| MTSP7 | **0.375** | **(5000,35000)** | **1 day** | 60 days | **100** | +0.564 | −0.143 |
| MTSP8 | **0.375** | **(5000,35000)** | **1 day** | **30 days** | 10 | +0.217 | −0.059 |
| MTSP9 | **0.375** | **(5000,35000)** | **1 day** | **30 days** | 1000 | +0.539 | −0.137 |

## 3.5. Results

### 3.5.1. Sensitivity studies

In figure 3.2 results from experiments RP0, MTP0, and MTSP0 are shown, compared to the change caused by a global reassignment of $P^* = 15000$ N m$^{-2}$ in REF2. The differences in monthly mean sea ice volume and concentration between each approach and the reference run REF for the Northern Hemisphere for 3 yr reveal that the time and space correlated perturbations in MTSP0 are by far the most influential, comparable in magnitude to the deterministic REF2 experiment with $P^* = 15000$ N m$^{-2}$. It can also be seen that all three approaches lead to an increase in total ice volume and a decrease in total ice area. This is consistent with the reasoning by *Owens and Lemke* (1990): If $P^*$ values in the stochastic simulations are low, sea ice thickness

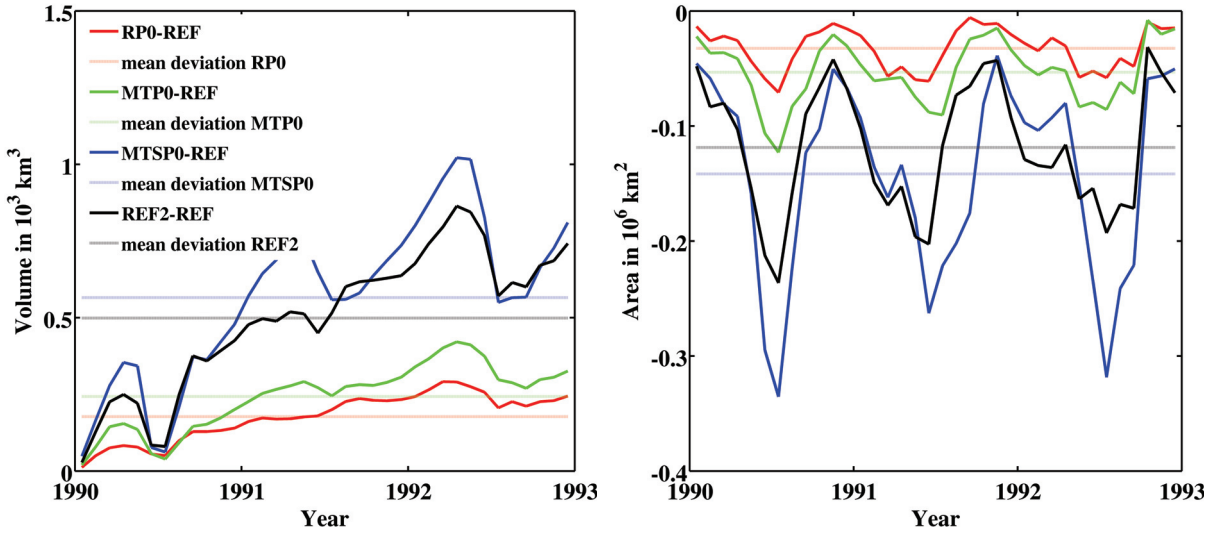


Figure 3.2: Effect of the three different perturbation approaches on the Arctic sea ice (left) volume and (right) area. Shown is the difference in total Northern Hemisphere sea ice volume and area between the reassignment time step perturbation RP0 (red), Markov process time correlated perturbation MTP0 (green), Markov process time and space correlated perturbation MTSP0 (blue), and the reference run REF with $P^* = 20000$ N m$^{-2}$, respectively, for three years. The difference is taken between monthly mean values of the respective stochastically perturbed experiment and the reference run. For comparison, the difference between the deterministic experiment REF2 with $P^* = 15000$ N m$^{-2}$ and the reference run REF is also shown (black). Light-colored horizontal lines give the respective mean deviations for the entire period.

increases locally along lines of convergent drift while the sea ice coverage around those areas is decreased. This allows ice-free areas to freeze over and the cycle is repeated. Locally high $P^*$ values, on the other hand, do not enforce a decrease in sea ice thickness within that area but simply reduce convergent sea ice drift and keep the ice thickness at the current level. Therefore, even for symmetric perturbations, the tendency is toward locally increased sea ice thickness and decreased sea ice concentration, which leads to a slight increase in total Arctic sea ice volume.

For the cases of global parameter changes of $P^*$ (e.g., REF2) all Arctic sea ice is weakened compared to the reference run REF. This leads to the growth of thicker ice through convergence and a resulting opening of sea ice cover. While this is a large-scale effect, in the simulations with symmetric perturbations of $P^*$ the effects are very localized, which might lead to a hindered increase in sea ice thickness at one point in time and space (high $P^*$ value) but also to a more than compensating increase in ice thickness at another point (low $P^*$ value).

Generally the effect of the stochastic perturbations on the sea ice volume is largest during the melting season in spring, while the total sea ice area shows the strongest response in the summer months, as will be discussed in section 3.5.2 for the ensemble simulation.

For MTSP0 figure 3.3 shows the evolution of the mean monthly difference in total ice (right) area and (left) volume with respect to the reference run REF for 17 yr. It takes about 3 yr until the perturbed simulation run reaches a new quasi-steady state. There is an anomaly in the modeled sea ice volume difference around the year 1997 due to a rapid decrease in the total REF and also MTSP0 sea ice volume in 1995 and 1996.

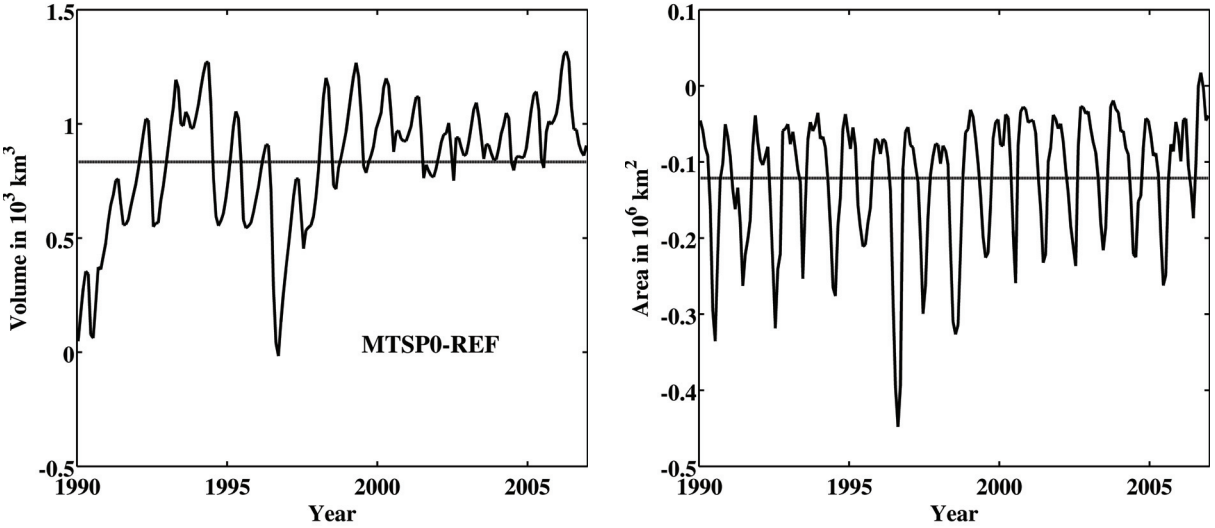


Figure 3.3: Differences in total Northern Hemisphere sea ice (left) volume and (right) area between MTSP0 and REF for 17 years. The difference is taken between respective monthly mean values. Horizontal lines give the mean deviations for the entire period.

The mean total change in Arctic ice volume for the 17 yr simulated ($+0.83 \times 10^3$ km$^3$) makes up about 4% of the reference run's sea ice volume. For the total sea ice area the mean value of the decrease is $-0.12 \times 10^6$ km$^2$, which is only about 1% of the reference run's mean sea ice area.

Figure 3.4 shows the local effect of the three different approaches RP0, MTP0, and MTSP0, revealed by the differences in monthly mean sea ice thickness and concentration between the stochastic model runs and the reference run for the summer 1992 (June–August (JJA)). As can be clearly seen, the magnitude of the local thickness and concentration changes is increased by the inclusion of time and especially space correlation within the stochastic perturbations. Especially along coastlines, in areas of convergent drift and with multiyear ice coverage, the sea ice thickness is increased.

As the sea ice concentration is high in the central Arctic Ocean, changes of ice concentration mostly occur along the ice edge and in areas of lower concentration where there is also convergent drift (increase of concentration) or even divergent drift or reduced convergent drift relative to the reference run, newly created by drift pattern changes in nearby areas. For winter months the changes in sea ice concentration are mostly confined to a small front parallel to the eastern Greenland coast and within the Bering Strait, as modeled sea ice concentrations farther north are around 95%–100% in winter (not shown) and thus do not leave much space for a further increase of concentration in convergent drift.

In summary, the effect of the stochastic perturbations on the local sea ice concentration is rather small, with the strongest influence during the summer months. The influence on the location of the ice edge is very limited, as the changes in sea ice concentration especially during the winter months but also in summer are for most places not strong enough to fully remove the sea ice cover in the monthly means.

The choice of the distribution function used for stochastic perturbations only has a moderate

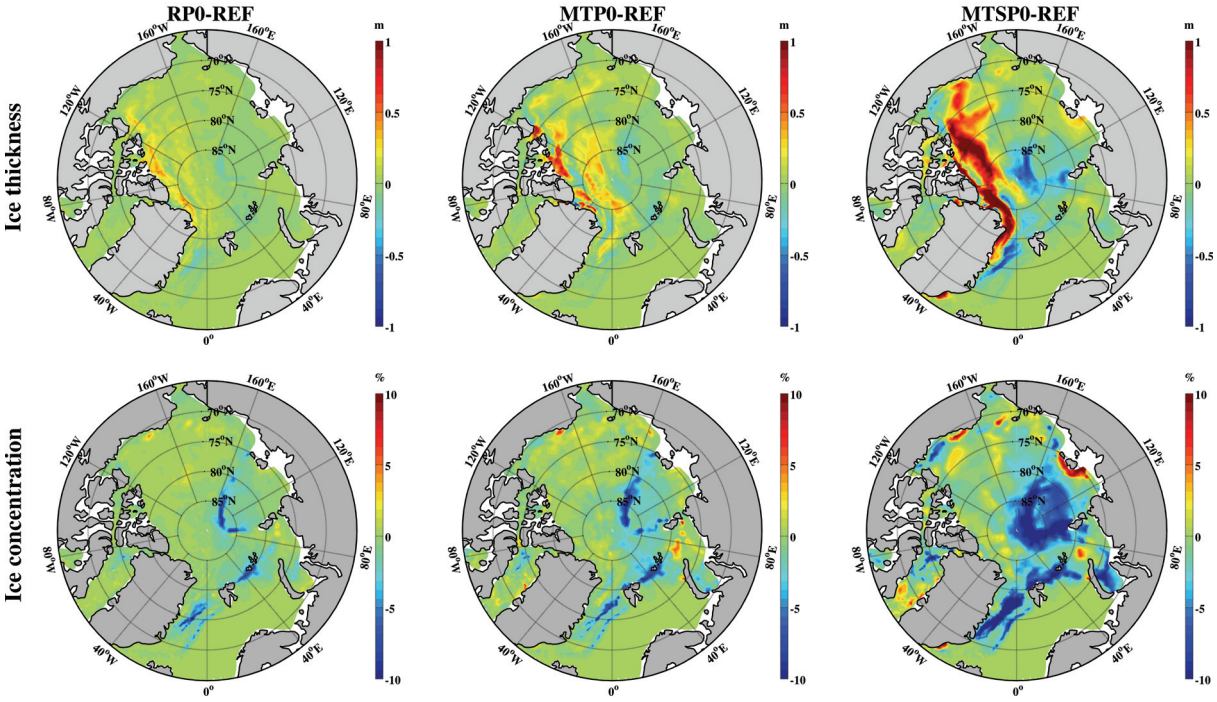


Figure 3.4: Differences in effective sea ice (top) thickness and (bottom) concentration between (left) reassignment time step perturbation RP0, (middle) Markov process time correlated perturbation MTP0, and (right) Markov process time and space correlated perturbation MTSP0 and the reference run REF with $P^* = 20000$ N m$^{-2}$, respectively. The difference is taken between the summer 1992 (JJA) mean values at all nodes.

effect on changes in total ice concentration and volume. Especially for MTP and MTSP, the transformation into the $x$-truncated Gaussian distribution shows the biggest difference in comparison to the reference run (not shown). This is because the truncated Gaussian distribution function assumes a relatively flat shape with the time-step-dependent increase in variance as given by equation (B.3) (see appendix B). As mentioned before, the small $P^*$ values have a bigger influence on the changes in sea ice concentration and volume than the high values, both of which occur more often with random numbers that follow a distribution function with a broad maximum.

From here on the $x$-truncated Gaussian distribution function will be generally used. Similar results with a slightly smaller difference between reference run and stochastic run can be obtained with the simpler transformation given by equation (A.1) (see appendix A) or the transformation into the $y$-truncated Gaussian distribution (not shown).

The last two columns of table 3.1 show the mean deviations in sea ice volume and area of the stochastic experiments from the reference run REF for the time period 1990 to 1992.

These sensitivity studies revealed that the most sensitive parameters in the MTSP are the limiting value $a$ for the range of $P^*$ (MTSP1 and MTSP2) and the correlation distance $d_{corr}$ especially between values of 10 to 100 km (MTSP8 and MTSP0).

A further increase in correlation distance to 1000 km (MTSP9) does not lead to a more pronounced impact on changes in ice volume and area compared to MTSP0 with 100-km correlation distance. These results provide insight into the range of spatial correlations within the

perturbations that are influencing the general sea ice thickness and concentration patterns.

The correlation time $\tau$ for MTP and MTSP has a quite small effect when it is varied in the limits investigated by *Lemke et al.* (1980). Only very small values can decrease the influence of the temporal correlation in a way that reduces the effect toward a no-time-correlation approach (e.g., MTSP5 and MTSP6). Changes in the redistribution time interval $(\Delta t)_{pert}$ for RP also have a small influence on the difference between reference run and stochastic run, with an increasing difference occurring with an increasing redistribution time interval size (not shown). The parameter that has a strong effect on the form of the distribution function after transformation is the variance $\tilde{\sigma}^2$ of the applied perturbations in MTP and MTSP, which itself can be regulated through the parameters $(\Delta t)_{pert}$ (MTSP3 and MTSP4) and $\sigma$ (see equation (3.11)).

As the time dependent total variance given by (B.3) rises quickly in the beginning but then tends asymptotically toward its limiting value (B.4), the limiting value is of importance when it comes to the form of the distribution function that most long-time ice-covered nodes share after transformation. Most values for $\tilde{\sigma}$ used in this study are relatively high. Because of the design of the transformations, the resultant form of the chosen bounded distribution function does not vary much for high values of the total variance (B.4) of the underlying Gaussian distribution. In our sensitivity studies medium to high values for variance lead to the biggest difference in sea ice volume and extent. Very high total variance values that are for example reached with $(\Delta t)_{pert} = 1\,\mathrm{h}$ (MTSP3) do not only seem unlikely but also do not show a stronger impact than values that are quite a bit smaller because the transformed distribution functions do not differ much. Only small $\tilde{\sigma}$ and therefore total variance values actually lead to a considerable decrease in the impact of the stochastic perturbations (e.g., with $(\Delta t)_{pert} = 7\,\mathrm{days}$ (MTSP4)).

### 3.5.2. Ensemble run

#### General evaluation

The ensemble experiment with eight ensemble members is used to analyze the mean effect of the Markov process time and space correlated perturbations of $P^*$. Furthermore, we are interested in the spread generated by the ensemble.

The parameter choice for the members is the same as for MTSP0 in table 3.1.

Figure 3.5 shows the impact of the stochastic perturbations on the monthly mean Northern Hemisphere ensemble mean sea ice volume and area compared to the reference run for the first 6 yr. Also shown are the differences of deterministic runs with fixed parameter values for $P^*$ (REF1 with 12500 N m$^{-2}$, REF2 with 15000 N m$^{-2}$ and REF3 with 17500 N m$^{-2}$) to the reference run REF with $P^* = 20000$ N m$^{-2}$. It can be seen that the changes in Arctic sea ice volume (increase) and area (decrease) that occur due to the stochastic perturbations are persistent even after performing the ensemble mean and cannot be reproduced by simple recalibration of fixed parameter values.

Figure 3.6 shows the changes in local sea ice thickness due to the stochastic perturbations for the mean of ENS (top left) compared to changes produced by the fixed parameter value run REF2 with 15000 N m$^{-2}$ (top right) for March 1995. While the changes due to the constant modification of the parameter value are very smooth in their spatial distribution in the central

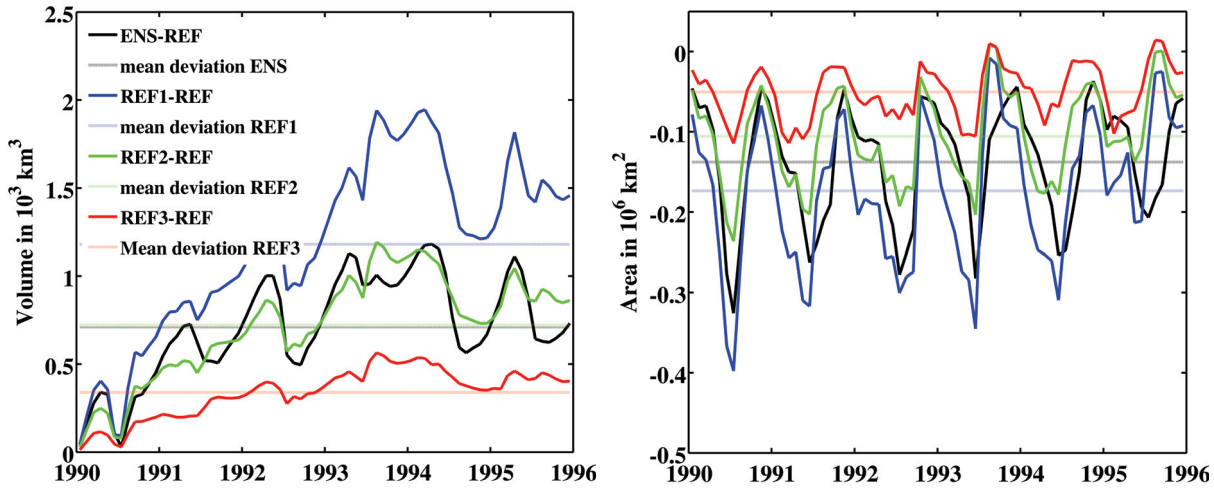


Figure 3.5: Differences in total Northern Hemisphere sea ice (left) volume and (right) area between the mean of the stochastic ensemble ENS (black) with Markov process time and space correlated perturbations, REF1 ($P^* = 12500$ N m$^{-2}$, blue), REF2 ($P^* = 15000$ N m$^{-2}$, green), REF3 ($P^* = 17500$ N m$^{-2}$, red), and the reference run REF with $P^* = 20000$ N m$^{-2}$, respectively. The difference is taken between monthly mean values. Light-colored horizontal lines give the respective mean deviations for the entire 6-yr period.

Arctic, the stochastic perturbations act locally and thus introduce considerable smaller-scale variability. The tendency toward increased multiyear ice thickness is consistent in both experiments. This is also visible when looking at the modeled ice thickness distribution of the reference run REF (figure 3.6, bottom left), the ensemble mean (figure 3.6, bottom middle), and REF2 (figure 3.6, bottom right) for the entire Arctic. As can be seen, the ice thickness distribution of the ensemble mean shows a longer right tail similar to REF2 with 15000 N m$^{-2}$ when compared with REF. Sea ice thickness in the ensemble can reach more than 9 m. On the other hand, while the general structure of the distribution is the same for the three simulations, with a peak for thin first-year ice and another one for the thicker multiyear ice with a thickness of about 2 m, both peaks are more pronounced for the ensemble mean (figure 3.6, bottom middle). All three distributions are reasonable when compared to measurements, as multiyear and first-year ice are clearly distinguishable, even though the location and height of the peaks might be slightly different in measured samples depending on sampling time and place (S. Hendricks 2012, personal communication; *Yu et al.*, 2004).

The difference in monthly mean sea ice thickness averaged for the entire Arctic (monthly mean total sea ice volume divided by monthly mean sea ice area) between the mean of the ensemble run ENS and the reference run REF with $P^*_{ref}$ ranges from about +0.08 m (about +5% of reference run mean sea ice thickness) in January to more than +0.26 m (more than +11%) in September, here discussed for 2004. This implies that the biggest effect of the perturbations pertains to thick multiyear ice that survives the spring melt. The ratio of the area of multiyear ice to the area of first-year ice increases in spring toward summer when the total sea ice area decreases.

Moreover, the changes in multiyear ice thickness are strong enough to increase the relative

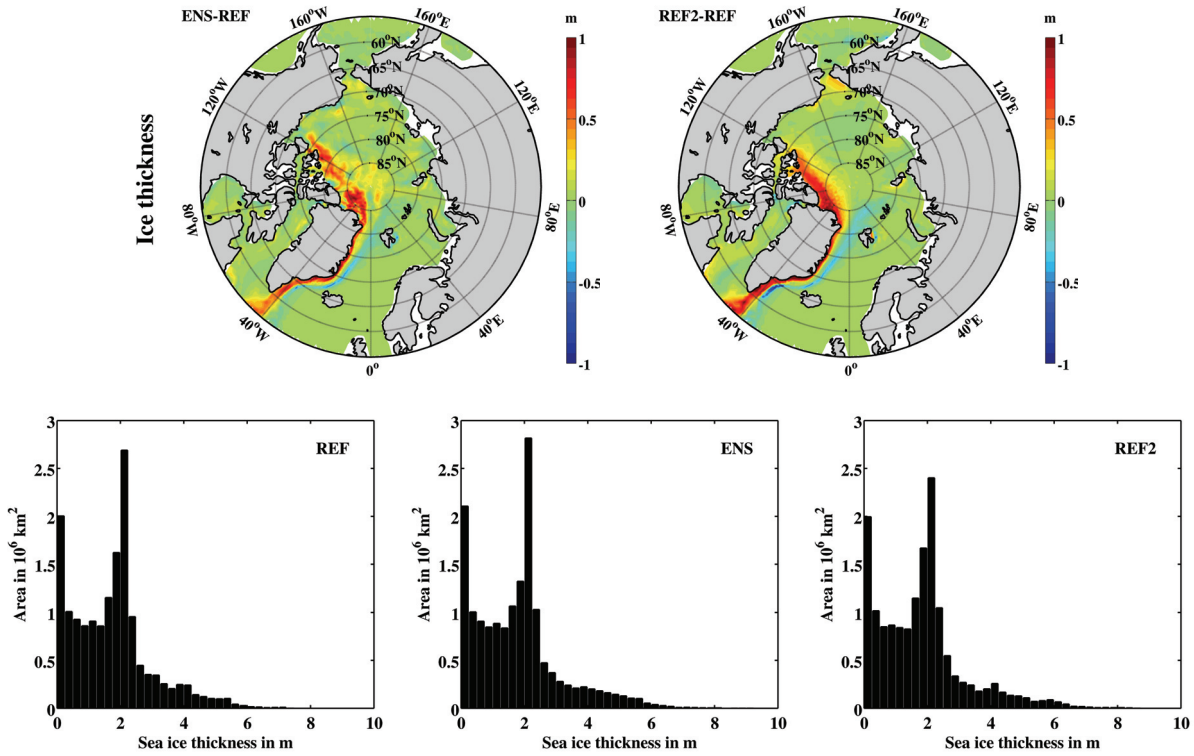


Figure 3.6: (top) Differences in effective sea ice thickness between the mean of (left) the stochastic ensemble ENS and (right) REF2 ($P^* = 15000$ N m$^{-2}$) and the reference run REF with $P^* = 20000$ N m$^{-2}$, respectively. The difference is taken between March 1995 mean values at all nodes. (bottom) Northern Hemisphere sea ice thickness distribution, March 1995, for (left) the reference run REF, (middle) the mean of the ensemble ENS, and (right) REF2. Open water is not considered.

difference between ensemble and deterministic run even though the mean monthly ice thickness of both experiments increases substantially during spring from about 1.7 m in November to about 2.6 m in July 2004. In figure 3.7 the relative influence of the ensemble run on sea ice volume and area compared to the reference run can be seen. Once again this figure shows the increased influence of stochastic perturbations in the late spring and summer months.

As the effects of the stochastic perturbations in the dynamics scheme of the model add up over time when it comes to sea ice thickness, regions with all-year ice coverage produce a pronounced difference in ice thickness compared to the reference run REF. Figure 3.8 illustrates this for the 14-yr mean seasonal difference between the reference run REF and the mean of the ensemble ENS.

The first three years (1990–92) have been omitted in the averaging for figure 3.8, as the quasi-steady state of the difference is reached around 1993.

The effect of the stochastic perturbations on the multiyear ice is of comparable magnitude in winter and summer, whereas first-year ice exhibits only a minor response to the parameter perturbation in the long-term mean.

In addition to the long-term means of figure 3.8, figure 3.9 presents the monthly mean sea ice thickness standard deviations of the stochastic ensemble for the Arctic for March 1996 (top

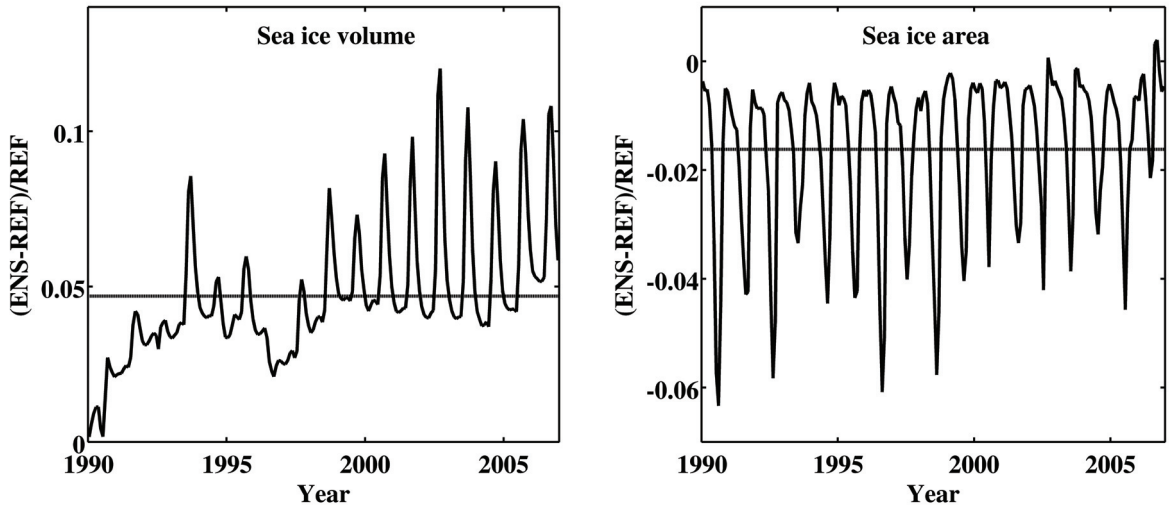


Figure 3.7: Relative influence of the ensemble mean of ENS on the Northern Hemisphere sea ice (left) volume and (right) area compared to the reference run REF with $P^* = 20000$ N m$^{-2}$, (ENS-REF)/REF. The relative difference is taken between monthly mean values. Horizontal lines give the respective mean deviations for the entire period 1990 to 2006.

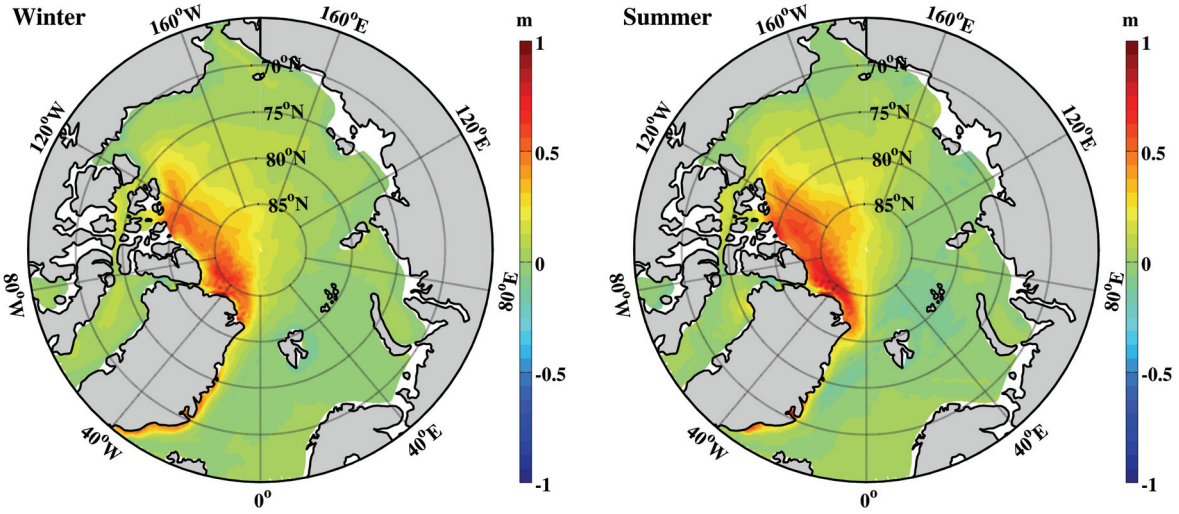


Figure 3.8: Differences in effective sea ice thickness between the mean of the stochastic ensemble ENS and the reference run REF with $P^* = 20000$ N m$^{-2}$ for (left) winters (December–February (DJF)) and (right) summers (June–August (JJA)) 1993 to 2006. The difference is taken between mean values at all nodes.

left) and March 2004 (top right). Furthermore the long-term mean standard deviation within the ensemble for the months of March 1993 to 2006 is illustrated by the bottom left panel of figure 3.9. Its magnitude is comparable to the modeled interannual variability of the reference run, shown in the bottom right panel as the sea ice thickness standard deviation for March 1993 to 2006.

The ensemble-generated spread is large in regions where dynamics has a strong influence during the whole year, while it is low in regions with a strong impact of seasonal melting and freezing

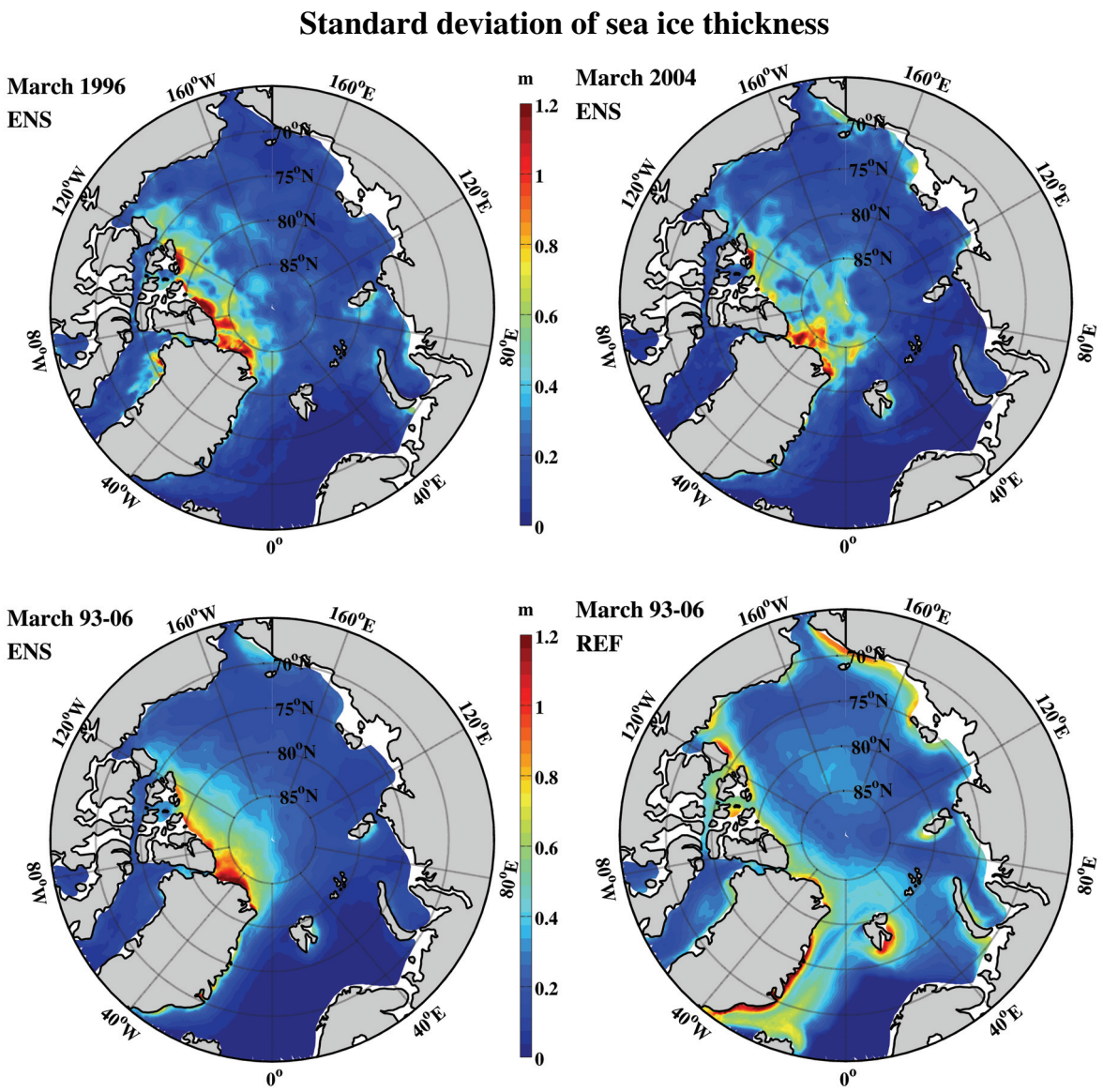


Figure 3.9: Ensemble- and model-generated spread. (top) The monthly mean linearly interpolated nodal sea ice thickness standard deviation of the stochastic ensemble ENS in the Arctic for (left) March 1996 and (right) March 2004. (bottom) (left) The ensemble-generated mean standard deviation for March of 1993 to 2006 and (right) the standard deviation of March from the reference run REF for the same time period.

processes and especially where the sea ice completely melts in summer. In the high-deformation region north of Greenland the ensemble-generated variability exceeds the interannual variability in the reference run by a factor of 2. The small ensemble spread for regions with predominantly first-year ice is even more visible in the summer months, even though the modeled interannual variability of REF is high in those months, especially in September (not shown).

### Comparison to observations

The effect of the stochastic perturbations on changes in sea ice concentration is small compared to changes in the sea ice thickness distribution.

Comparing model sea ice concentration data with satellite data from *Cavalieri et al.* (1996), the reference FESOM model run REF tends to overestimate the sea ice concentration, especially in Fram Strait and in the Greenland Sea (not shown). The stochastic ensemble exhibits only very marginal improvements in those regions during the winter months and no noteworthy improvements during the summer months (not shown).

Changes in sea ice velocities are generally small as well (not shown). The perturbations influence the sea ice velocities on rather short time scales, which has an influence on the sea ice thickness and concentration distribution, as changes concerning those variables can add up over time. Only strong changes in the sea ice thickness may (through sea ice rheology) cause changes in velocities that last for longer times.

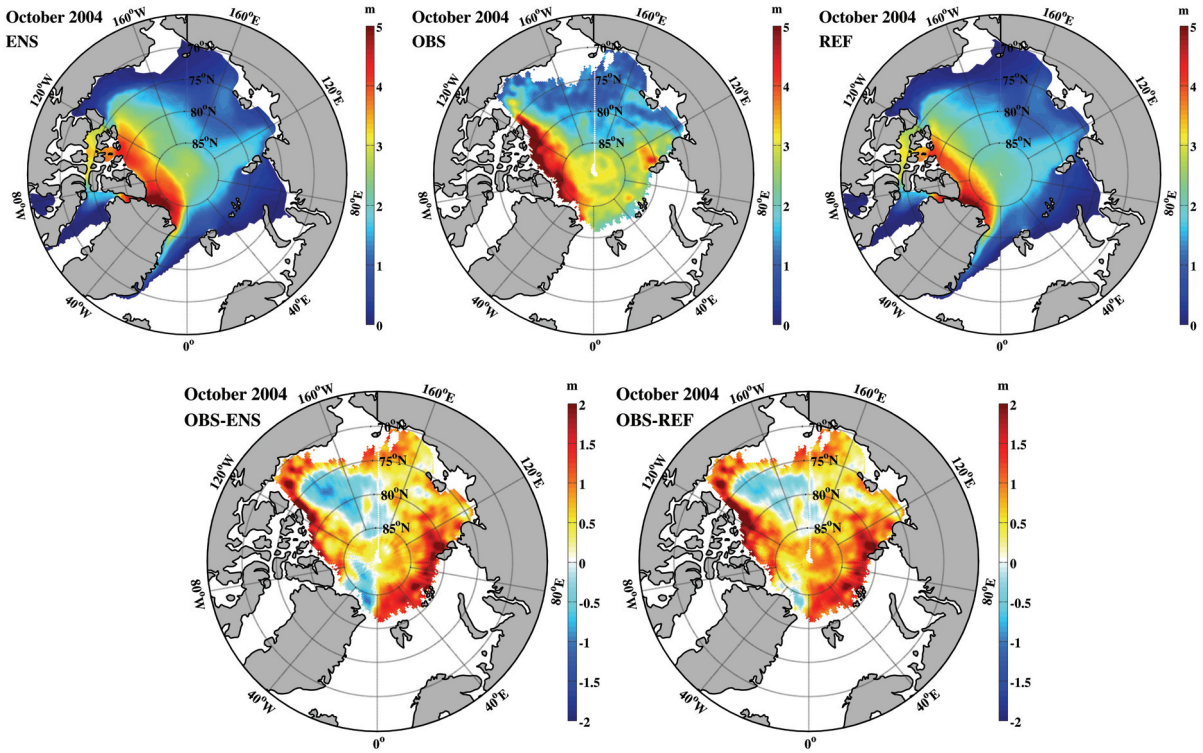


Figure 3.10: (top) Mean sea ice thickness distribution for the ensemble mean of (left) ENS, (right) the reference run REF, and (middle) the observation OBS (*Kwok et al.*, 2007, 2009) in the time interval 3 October to 8 November 2004. Observational data is restricted to the central Arctic Ocean. (bottom) The difference between the observation and (left) the ensemble as well as (right) the reference run. Modeled data has been interpolated to the grid of the observational data in the bottom row.

Comparing reference and ensemble experiments to satellite data for sea ice thickness (e.g., 3 October to 8 November 2004, derived by *Kwok et al.* (2007, 2009) from the Ice, Cloud, and Land Elevation Satellite (ICESat)), the ensemble is in better agreement with the observations for the multiyear ice north of Greenland, while the underestimation of the sea ice thickness in the eastern Arctic remains mostly unaffected (figure 3.10, bottom row). This holds for most of the five autumn and five winter months of the years 2003 to 2008, for which *Kwok et al.* (2007, 2009) presented observational data. The general distribution with the high sea ice thickness

along the northern Greenland coast and the Canadian Arctic Archipelago is reproduced by the reference run REF as well as by the mean of the ensemble run ENS (figure 3.10, top row).

When it comes to the comparison of local sea ice thickness with upward looking sonar (ULS) data, which give time series of observed sea ice draft at fixed locations, changes due to the stochastic perturbations are small and no general improvement of the ensemble mean compared to the reference run can be seen. This is mostly due to the fact that the ULS data points available for this study are located in regions where the impact of the stochastic perturbations is low (i.e., in the Beaufort Sea, Fram Strait, and Greenland Sea).

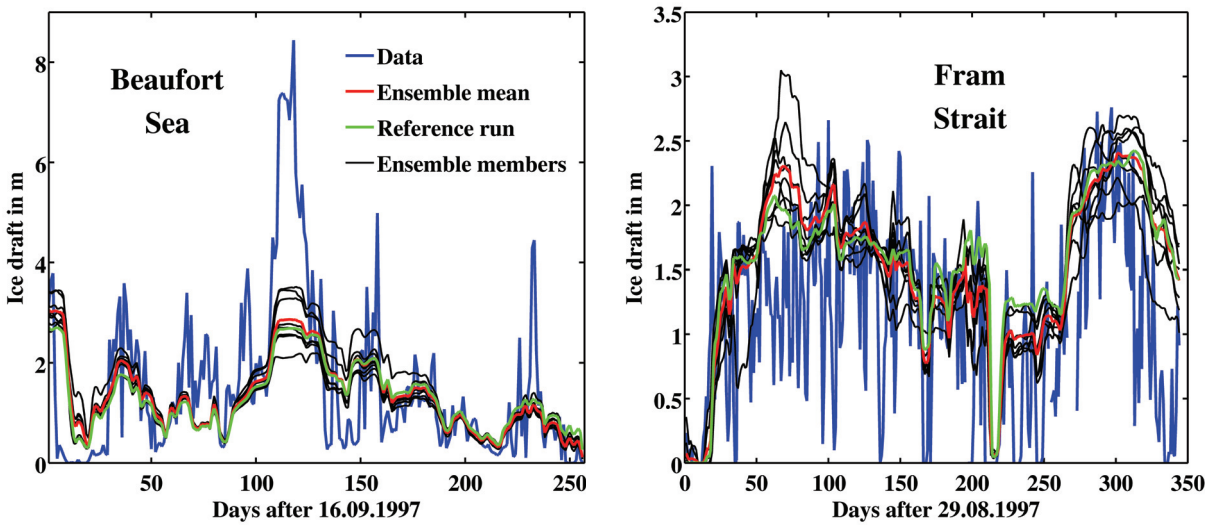


Figure 3.11: Time series of sea ice draft at (left) one location in the Beaufort Sea (*Melling and Riedel*, 2008) (74.15°N, 125.91°W, starting 16 Sep 1997) and (right) one in Fram Strait (*Witte and Fahrbach*, 2005) (79.01°N, 2.04°W, starting 29 Aug 1997). The measured data are shown in blue, the reference model REF data in green, the mean of the ensemble ENS data in red, and the eight ensemble members in black. The right panel has some data gaps (e.g., around days 250-270). Shown are daily averaged values.

As can be seen in figure 3.11 for two ULS data series, one in Fram Strait (right) and the other in the Beaufort Sea (left), the differences between the ensemble members of the stochastic model run are small and decrease in times of increased thermodynamic influence or divergent drifts, when the value of the ice strength is of little importance (e.g., around day 10 and day 130 in figure 3.11, left). The seasonal cycle has a strong effect on the ensemble spread, which goes down to zero when the sea ice melts in summer.

We have performed root-mean-square and mean difference calculations between the observations (9 ULS data series in the Beaufort Sea (*Melling and Riedel*, 2008) and 11 ULS data series in the Fram Strait and Greenland Sea (*Witte and Fahrbach*, 2005)) and the corresponding modeled ensemble mean time series. The same has been done between observations and the modeled reference run time series. Comparing the results indicated minor improvements for some time series due to the stochastic perturbations but also some minor worsening of results for other locations. Generally the ensemble spread is very small in these regions.

On the other hand, figure 3.12 shows that the sea ice thicknesses produced by the ensemble members at a location near the northern Greenland coast vary considerably. This is also true

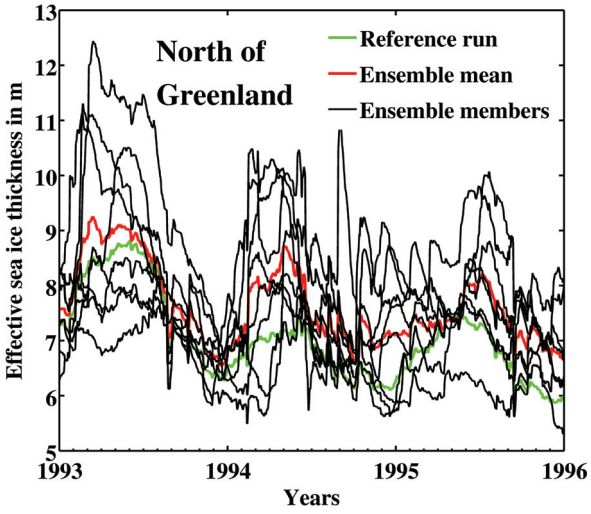


Figure 3.12: Time series of sea ice thickness at 84°N, 40°W of the reference run REF (green), the mean of the ensemble ENS (red) and the ensemble members (black) for three years starting at 1 Jan 1993.

when the ensemble mean is compared to the reference run. Standard deviation of the ensemble for the time series at 84°N, 40°W reaches, for example, 2.25 m and more in January 2002, while the mean difference between ensemble mean and reference run in, for example, the year 1994, is 0.79 m (about 12% increase). The cause for this is the reduced seasonal variability produced by thermodynamic melting and freezing compared to the variability due to dynamics in the central Arctic Ocean. Furthermore, the high amount of multiyear ice is of major importance, especially for the sea ice rheology.

Unfortunately, sea ice thickness data in the region north of the Greenland coast are not available in a way that allows for a meaningful comparison. This is also true when it comes to data necessary for calibrating the perturbation scheme correctly, with respect to the relation between ensemble mean error and ensemble spread.

## 3.6. Summary and outlook

Three different approaches to randomly perturb the parameter $P^*$ of the ice strength parameterization of the sea ice dynamics module in FESOM have been presented, with increasing complexity concerning temporal and spatial correlation. Because of the nonlinearity of the sea ice rheology, a symmetric perturbation of $P^*$ leads to a general increase in Arctic sea ice volume and a decrease in the sea ice area compared to a deterministic reference run. Inclusion of some temporal correlation via a Markov process and especially a spatial correlation between nodes with common neighbors proved to have a strong influence on the changes in the sea ice thickness and concentration distribution compared to the reference run. These changes cannot be reproduced by a global reassignment (reduction) of constant parameter values for $P^*$ in the purely deterministic model.

Especially in regions where the influence of sea ice dynamics is high and where there is

no complete melting of sea ice during summer, the most sophisticated stochastic parameter perturbation of this study, MTSP, with a Markov process time correlation and also a spatial correlation of nodes with common neighbors, shows a strong impact. The difference of the ensemble mean compared to the reference run, as well as the generated ensemble spread, is of considerable magnitude. Both increase during long-lasting periods of convergent drift and constant ice coverage. This reflects the cumulative nature of the deformation processes in the sea ice cover. On the other hand, the influences of melting and freezing as well as divergent drift patterns lead to a decrease in the ensemble spread and also in the mean influence of the $P^*$ perturbations.

Because of the lack of appropriate data, especially in regions with multiyear ice where the influence of the perturbation schemes is strongest, we cannot derive an exact calibration of spread compared to the ensemble mean error, either for sea ice thickness or for concentration. Compared to the model's interannual spread in sea ice thickness, though, the ensemble spread is of comparable magnitude. Using this finding as a first indication, the ensemble spread seems to be reasonable. The spread of sea ice thickness within the ensemble produced by the various $P^*$ perturbations applied may indicate a range of possible $P^*$ values for future data assimilation studies. It shows the general influence local changes of $P^*$ can have on the sea ice thickness distribution patterns within the model. Within this study an appropriate range of values seems to be $P^* \in (5000 \text{ N m}^{-2}, 35000 \text{ N m}^{-2})$.

To summarize the results of this paper, first of all it would be good to have a more extensive dataset for sea ice thickness, to be able to evaluate (not only) stochastic sea ice parameterization schemes more thoroughly. Long-time measurements at fixed locations such as ULS data are of great value for this purpose but are hard to obtain in regions with a thick perennial ice cover.

Nevertheless, even without such observations our results prove that it is of importance to look at the inherent uncertainties of parameterizations. One approach to do so is to include stochasticity in the formulation of parameterizations, as *Palmer* (2012) suggests in view of a probabilistic Earth-system simulator. The effect of parameterization uncertainties is going to be even stronger in fully coupled atmosphere–ocean–sea ice models and will influence the potential of the model to predict future states of the climate system. We are currently working on the inclusion of stochastic sea ice parameterizations in such a fully coupled model.

Even though we have as yet only presented a first approach to stochastic perturbations in a sea ice model, we think that such probabilistic parameterizations should be implemented in future climate ensemble prediction systems to include the model uncertainty at a level where it first appears in the equations. This is especially of importance when it comes to seasonal and interannual predictions.

In the process of developing parameterizations and assessing their inherent uncertainties it is essential to think about model resolution, as increased model resolution has an impact on the statistics the parameterizations are based upon. These changing statistics might be more readily applied to a stochastic parameterization than a purely deterministic one.

Perturbing $P^*$ in a sea ice model is a first step toward addressing these topics and serves as a tool to test and evaluate the sensitivities of the model and the mesh it uses. Even though a constant $P^*$ value might be sufficient for many problems, it should be kept in mind what an

influence slightly perturbed parameters may have, even if the perturbations are symmetric.

Further work will now be directed toward other perturbation schemes, especially concerning spatial correlation, and toward other parameters of the sea ice model, especially toward thermodynamic parameters such as the sea ice albedo. In a first step, we compared our approach of a stochastically perturbed $P^*$ with a realization of the stochastically perturbed parameterization tendencies (SPPT) scheme by *Buizza et al.* (1999). Here, the parameterization of the internal forces $\vec{\mathbf{F}}_{int}$ in equation (3.1) has been perturbed by multiplicative noise. In our experiment with the SPPT scheme there was no spatial correlation between nodes and the reassignment time steps used were similar to those of our reassignment time step perturbation approach, RP. The results of this first application of the SPPT scheme to sea ice dynamics showed changes of similar magnitude as the RP approach (not shown). Therefore implementation of temporal correlation in the Markov process time correlated approach, MTP, and implementation of temporal and spatial correlation in the MTSP approach proved to be much more influential concerning sea ice dynamics than this specific realization of the SPPT scheme. We have also started to apply the general idea of perturbing traditionally fixed parameters in some preliminary experiments to the parameter $C$ in equation (3.7) of the sea ice rheology and also to the lead closing parameter $h_0$ used in the parameterizations of the continuity equation for the sea ice concentration. The latter parameter influences the relation between increase in sea ice thickness and increase in sea ice concentration (lead closing) during freezing conditions.

First results have shown that parameter perturbations concerning $C$ are of less importance compared to $P^*$, whereas the perturbations of $h_0$ show quite a strong response with respect to the sea ice concentration in the Southern Hemisphere (not shown). For Southern Ocean sea ice, the influence of $P^*$ perturbations is small, which is partly due to the small amount of modeled multiyear ice in this FESOM version, but probably also reflects the natural differences between Arctic and Antarctic. Further studies connected to these first results will be directed toward the different influences parameter perturbations have on changes in ice thickness and concentration distribution in the Northern and Southern Hemisphere, which have shown quite diverging results so far.

Another issue that will be investigated in the future is the influence of methods that can be used to include spatial correlation of random values. It is of great interest to see how this correlation, and therefore the entire stochastic parameterization, is influenced by the varying mesh resolution in a finite element model. For investigations of the resolution-dependent behavior of stochastic and also deterministic parameterizations FESOM is an excellent tool.

***Acknowledgments.*** We thank Sergey Danilov, Thomas Jung, and Martin Losch for their help and advice in preparing this publication. Our thanks go to Hannelore Witte for providing the Greenland Sea and Fram Strait ULS data and to Stefan Hendricks, who helped us with his knowledge of Arctic sea ice thickness distributions. Finally, we thank the two anonymous reviewers for their helpful comments and advice. The Beaufort Sea ULS data and the sea ice concentration data were obtained from the National Snow and Ice Data Center (NSIDC), Boulder, Colorado (`http://www.nsidc.org/`). The sea ice thickness ICESat-data were obtained from the NASA Jet Propulsion Laboratory (`http://rkwok.jpl.nasa.gov/`).

# 4. Influence of stochastic sea ice parametrization on climate and the role of atmosphere–sea ice–ocean interaction[11]

[11]This chapter has been published under the title *Influence of stochastic sea ice parametrization on climate and the role of atmosphere–sea ice–ocean interaction* in the *Philosophical Transactions of the Royal Society A: Mathematical, Physical and Engineering Sciences* (see reference *Juricke and Jung*, 2014). The original layout of the article was changed to match the layout of the dissertation. No changes to the text were made, though, except for minor misspelling corrections. Additionally, referencing to figures, equations and tables as well as citations were altered. They have been changed to match the respective layout in the rest of the dissertation. The following figures differ slightly from the original publication, owing to the editing by the publisher. In addition, the bibliography of the publication has been merged with the bibliography of the dissertation. The abstract of the article was retained. My contributions to this article include all the necessary implementations and model adjustments, the experimental set-up and initialization as well as monitoring of the simulations. I carried out all of the diagnostics and the plotting of the results. The concept for the experimental set-up as well as the evaluation, assessment, and interpretation of the results were developed and conducted in discussions with my coauthor Thomas Jung. He has also corrected my original manuscript before submission to the journal. In addition, I would like to point to the acknowledgments at the end of the article.
Please excuse any remaining inconsistencies with the other chapters of this dissertation originating from the general layout of the original publication, including differences in spelling, figure layout, acronyms, equations and phrasing.

**Abstract**

The influence of a stochastic sea ice strength parametrization on the mean climate is investigated in a coupled atmosphere–sea ice–ocean model. The results are compared with an uncoupled simulation with a prescribed atmosphere. It is found that the stochastic sea ice parametrization causes an effective weakening of the sea ice. In the uncoupled model this leads to an Arctic sea ice volume increase of about 10–20% after an accumulation period of approximately 20–30 years. In the coupled model, no such increase is found. Rather, the stochastic perturbations lead to a spatial redistribution of the Arctic sea ice thickness field. A mechanism involving a slightly negative atmospheric feedback is proposed that can explain the different responses in the coupled and uncoupled system. Changes in integrated Antarctic sea ice quantities caused by the stochastic parametrization are generally small, as memory is lost during the melting season because of an almost complete loss of sea ice. However, stochastic sea ice perturbations affect regional sea ice characteristics in the Southern Hemisphere, both in the uncoupled and coupled model. Remote impacts of the stochastic sea ice parametrization on the mean climate of non-polar regions were found to be small.

## 4.1. Introduction

Accurately simulating sea ice is an essential part of coupled Earth system modelling. Sea ice has a strong impact on the heat and momentum exchange between the atmosphere and ocean. As an insulating layer, sea ice can partially decouple the atmosphere from the ocean, and through the albedo feedback, it influences the radiation balance at the surface.

Sea ice also alters the freshwater content of the upper ocean and hence ocean deep convection; therefore, sea ice is an important driver of changes in the global overturning circulation of the ocean. Sea ice is also considered to be a main factor for the Arctic amplification of anthropogenic climate change.

Sea ice is known to show changes on a wide range of temporal scales. There is evidence, for example, for high interannual variability, both locally (*Hendricks et al.*, 2011) and Arctic wide (*Laxon et al.*, 2003). Furthermore, recent years have shown a strong decrease in Arctic sea ice volume (*Kwok and Rothrock*, 2009; *Kwok et al.*, 2009) and area, which is only partly captured by models (*Turner et al.*, 2013; *Johnson et al.*, 2012; *Stroeve et al.*, 2012). Potential predictability studies for the Arctic reveal the importance of an accurate simulation of the prevailing sea ice thickness conditions to allow for skilful seasonal and interannual predictions of Arctic sea ice (*Holland et al.*, 2011; *Chevallier and Salas-Mélia*, 2012).

To simulate sea ice thickness and concentration fields realistically, it is crucial to adequately capture the drift of the sea ice (*Fichefet and Maqueda*, 1997). Sea ice drift is strongly influenced by the sea ice dynamics which, in turn, hinges on the formulation of the sea ice rheology that describes the deformation behaviour in the presence of convergent flow. Most climate models use the widely used viscous–plastic rheology by *Hibler* (1979) or the modified elastic–viscous–plastic rheology (*Hunke and Lipscomb*, 2010); other formulations are being tested (*Girard et al.*, 2011), and different ways of solving the highly nonlinear equations are emerging from the viscous–plastic formulation (*Lemieux et al.*, 2012; *Losch et al.*, 2013). Still, all existing parametrizations have certain shortcomings when it comes to the representation of sea ice deformation and the resulting sea ice drift. Therefore, the sea ice rheology has to be considered as a significant source of uncertainty in coupled climate models.

In the past two decades or so, the representation of model uncertainty in models has become a major area of research. Studies with simplified models such as the Lorenz '96 system (*Lorenz*, 1996) emphasize the importance of developing and analysing stochastic parametrizations as a promising alternative to deterministic schemes (*Wilks*, 2005; *Arnold et al.*, 2013). A lot of progress in this field has been made in atmospheric modelling and especially weather forecasting. Different studies have shown the importance of stochastic approaches when it comes to accounting for model uncertainty and for accurately representing subgrid scale processes. Approaches range from estimating the accumulated physical tendency uncertainty in the formulations of the discretized prognostic equations (*Buizza et al.*, 1999; *Weisheimer et al.*, 2011) to a stochastic kinetic energy backscatter scheme which simulates the backscatter of dissipated energy from unresolved to resolved scales (*Shutts*, 2005; *Jung et al.*, 2005; *Berner et al.*, 2009). Moreover, stochastic parametrizations have been developed for non-orographic gravity waves (*Lott et al.*, 2012), convection (*Lin and Neelin*, 2002), and deep convection (*Plant and Craig*,

2008). In addition, stochastic perturbations have been applied to a variety of parameters within deterministic parametrizations (*Lin and Neelin*, 2000; *Bright and Mullen*, 2002; *Li et al.*, 2008).

While the emphasis of previous research has been on the atmosphere, more recently stochastic approaches have also been developed for other parts of the Earth system. Examples include the stochastic representation of the ice strength parameter in sea ice–ocean models (*Juricke et al.*, 2013), the use of stochastic perturbations for oceanic temperature and salinity fields in the computation of the horizontal density field (*Brankart*, 2013) and the stochastic representation of turbulent surface fluxes at the atmosphere–ocean interface in a coupled model (*Williams*, 2012). Those studies demonstrate that the explicit representation of model uncertainty in models has not only the benefit of improved ensemble prediction capabilities, but that stochastic parametrizations also have the potential to change the climate of models. It has been argued, therefore, that stochastic parametrizations should be incorporated in the next generation of climate models (*Palmer*, 2012).

In this study, the influence of using stochastic dynamical formulations in sea ice models will be further explored building on the work of *Juricke et al.* (2013), in which stochastic perturbations have been applied to the sea ice strength parametrization of the sea ice rheology formulation in a sea ice–ocean model. Here, a slightly modified stochastic parametrization is tested. Furthermore, it is investigated whether the substantial changes in the mean climate state caused by the stochastic sea ice parametrizations in a sea ice–ocean model found by *Juricke et al.* (2013) also translate to fully coupled climate models. It is of importance, also for future ensemble simulations, to be aware of any impact on the mean climate owing to uncertainty estimates in parametrizations and in this context to understand effects of perturbations in highly nonlinear systems. This study also aims at detecting the possibly differing impacts in the more complex coupled system compared with uncoupled models. To this end, the coupled atmosphere–ocean–sea ice–land surface system ECHAM6-FESOM is used in a configuration with relatively high resolution in the Arctic ocean (*Sidorenko et al.*, 2014). More specifically, single climate simulations are conducted to analyse the impact of the stochastic parametrization on the mean state of the system. The atmospheric fluxes generated by a coupled reference simulation are then used to carry out experiments with the uncoupled sea ice–ocean model with stochastic sea ice strength parametrization. In this way, it is possible to explore the role of atmospheric feedback processes in determining the response of the climate system to stochastic sea ice perturbations. As only one single parametrization is affected by perturbations, it is still feasible to find some detailed physical explanations for the workings and effects of the perturbations on sea ice variables in the uncoupled as well as the coupled system.

The structure of this paper is as follows: section 4.2 gives a short summary of the model and the stochastic parametrization, including a description of the modification of the spatial correlation procedure for the stochastic perturbations originally developed by *Juricke et al.* (2013). Furthermore, the experimental set-up is explained. In section 4.3, the impact of the stochastic parametrization on the global mean climate is analysed and discussed. Detailed explanations of the differing effects in the coupled and uncoupled simulations are given. Finally, section 4.4 gives a summary, some concluding remarks and an outlook for future work.

## 4.2. Experimental set-up

In this study, the coupled model ECHAM6-FESOM is used. ECHAM6 is the spectral atmospheric climate model of the Max Planck Institute for Metereology in Hamburg (*Stevens et al.*, 2013). It is coupled through the OASIS3–MCT coupler (*Valcke*, 2013) to the finite-element sea ice ocean model (FESOM) of the Alfred Wegener Institute in Bremerhaven (*Danilov et al.*, 2004; *Wang et al.*, 2008; *Timmermann et al.*, 2009; *Sidorenko et al.*, 2011; *Wang et al.*, 2013). While ECHAM6 uses a T63L47 grid with a resolution of about 1.85° and 47 vertical levels, FESOM uses an unstructured triangular finite-element grid for the ocean surface and the sea ice model, with resolutions ranging from over 150 km in the open oceans to about 25–10 km in the Arctic and near the coasts. In addition, there is a gradual increase in resolution along the equatorial belt in the tropics to about 25 km (see figure 1 in *Sidorenko et al.*, 2014). The three-dimensional ocean model uses a tetrahedral grid of 46 unevenly spaced $z$-levels. The timestep of FESOM is 30 min, whereas ECHAM6 uses a timestep of 10 min. Coupling takes place every 6 h. Further details on ECHAM6-FESOM, its set-up and mean-state performance are discussed by *Sidorenko et al.* (2014). The climate variability of the model is described in *Rackow et al.* (2014).

The prognostic variables of the sea ice model are the effective (mean) sea ice thickness, $h_{ice}$, the lateral sea ice velocities, $u_{ice}$ and $v_{ice}$, and the sea ice concentration, $A$, as well as the mean snow layer thickness, $h_s$. The evolution of $h_{ice}$, $h_s$ and $A$ is described by equations for advection as well as freezing and melting processes. Changes in sea ice velocities are calculated using the equation of momentum balance.

### 4.2.1. Stochastic sea ice strength parametrization

The stochastic parametrization used in this study is described in detail by *Juricke et al.* (2013). In the following, therefore, only a brief explanation is given, and differences to the original formulation are highlighted.

The equation of momentum balance for the lateral sea ice velocities is given by

$$m\frac{\partial \vec{\mathbf{u}}_i}{\partial t} = \vec{\boldsymbol{\tau}}_{air} + \vec{\boldsymbol{\tau}}_{ocean} - mf\vec{\mathbf{k}} \times \vec{\mathbf{u}}_i - mg\nabla\eta_o + \vec{\mathbf{F}}_{int}. \tag{4.1}$$

In (4.1) $m$ is the mass per unit area, $\vec{\mathbf{u}}_i$ is the horizontal sea ice velocity vector, $\vec{\boldsymbol{\tau}}_{air}$ and $\vec{\boldsymbol{\tau}}_{ocean}$ are the atmospheric and oceanic stress, respectively, $f$ is the Coriolis parameter, $\vec{\mathbf{k}} = (0, 0, 1)$, $g$ is the gravitational acceleration and $\eta_o$ is the sea surface height of the ocean.

The internal forces $\vec{\mathbf{F}}_{int} = (F_1, F_2)$ are parametrized using the highly nonlinear elastic–viscous–plastic rheology (*Hunke and Lipscomb*, 2010) which is based on the viscous–plastic rheology by *Hibler* (1979). Some further adjustments have been made by *Harder* (1996). Within this parametrization, the so-called internal ice strength $P$ can be interpreted as a regularization factor for the yield curve which describes all possible combinations of stresses that lead to the yielding of the sea ice. Therefore, large values of $P$ lead to an increased resistance of the ice when it comes to convergent motion, whereas small values of $P$ produce weaker sea ice and an earlier onset of plastic deformation. This, by changes in the sea ice velocities, leads to a piling up of sea ice and an increase of sea ice thickness. $P$ itself depends linearly on the factor $P_p$ given

by

$$P_p = P^* \frac{h_{ice}}{A} \cdot \exp(-C(1-A)), \tag{4.2}$$

where $P^*$ and $C$ are dynamic ice strength parameters.

To account for uncertainties in the choice of the empirical parameter $P^*$, including temporal and spatial variability, *Juricke et al.* (2013) have applied a symmetric Markov process time and space correlated perturbation (MTSP) to $P^*$. Adjustments to the spatial correlation of the perturbations are outlined in the following.

For each timestep $j$ and node $i$ of the ice covered triangular surface mesh, a new value,

$$P^*(i,j) = (1 + x(i,j)) \cdot P^*_{ref}, \tag{4.3}$$

is calculated. $P^*_{ref} = 30\,000\,\mathrm{N\,m^{-2}}$ is the reference value of the regular deterministic parametrization and $x(i,j)$ is a random number from a symmetric distribution with zero mean. In addition, $x(i,j) \in (-0.75, 0.75)$ and therefore $P^*(i,j) \in (7\,500\,\mathrm{N\,m^{-2}}, 52\,500\,\mathrm{N\,m^{-2}})$. Note that the value for $P^*_{ref}$ in the three simulations of this study differs from the value of 20 000 N m$^{-2}$ used in MTSP by *Juricke et al.* (2013). As $P^*$ is one of the tuning parameters of the sea ice model, it was used to adjust sea ice extent and volume in the coupled set-up.

In summary, equation (4.3) describes a random perturbation of a previously fixed parameter. To create spatially and temporally correlated perturbations $x(i,j)$ with a bounded distribution, transformations of Gaussian random numbers are used. First, time correlation is generated by

$$y(i,j) = \alpha y(i,j-1) + z(i,j), \tag{4.4}$$

with autocorrelation $\alpha = 0.994$ and $z(i,j)$ an uncorrelated Gaussian-distributed random number with zero mean and standard deviation $\sigma = 0.375$. The timestep of the ocean and sea ice model is $\Delta t = 30\,\mathrm{min}$. These values are within the range of values tested in *Juricke et al.* (2013) even though they differ slightly from their preferred parameter choice, implying a slightly larger maximum variance $\sigma^2_{lim}$ (for $j \to \infty$) for the autoregressive process in (4.4).

The values $y(i,j)$ are then spatially correlated using two correlation matrices $C_{NH}$ and $C_{SH}$, one for the nodes above 45° and one for below −45°, respectively, to ensure that the Northern Hemisphere (NH) and Southern Hemisphere (SH) sea ice are uncorrelated. The entries of each matrix are given by $C^{nm}_X = e^{-d_{nm}/d_{corr}}$, $X = \{NH, SH\}$, where $d_{nm}$ is the distance between node $n$ and $m$, from the respective hemisphere, and $d_{corr} = 1000\,\mathrm{km}$ for both matrices. For this new spatial correlation scheme, $d_{corr} = 1000\,\mathrm{km}$ was chosen to produce large-scale patterns in the variations of $P^*$ and possibly maximize the impact of the perturbations.

Using the Cholesky decompositions of $C_{NH}$ and $C_{SH}$, spatially correlated $\hat{y}(i,j)$ can now be generated for both hemispheres from the temporally correlated $y(i,j)$, by simple matrix–vector multiplication. As the resulting random numbers are still Gaussian distributed, the transformation

$$x(i,j) = -a + \frac{2a}{(1 + e^{(-\beta \hat{y}(i,j))}} \tag{4.5}$$

transforms the numbers into the limited range $(-a, a)$ with $a = 0.75$ and $\beta = 1/\sigma_{lim}$ with

$\sigma_{lim} = \sqrt{\sigma^2/(1-\alpha^2)}$ (*Juricke et al.*, 2013). For the initialization of the random numbers, equation (4.4) is solved successively a couple of thousand times at the beginning of each climate simulation to reach this maximum standard deviation of the autoregressive process.

### 4.2.2. Simulations

To investigate the impact of the stochastic parametrization several multi-decadal integrations have been carried out. A simulation with the coupled ECHAM6-FESOM model *without* stochastic sea ice parametrization serves as the reference integration (REF hereafter). The surface flux fields from REF, saved for every 6 hourly coupling timestep, were used to drive FESOM in uncoupled mode with the stochastic sea ice parametrization switched on (STOCH_UNCPL hereafter). This integration allows for a direct evaluation of the impact of stochastic sea ice parametrization on sea ice distribution and ocean currents without an interactive atmosphere. To analyse the impact of atmospheric feedbacks another experiment with the coupled model ECHAM6-FESOM has been carried out in which the stochastic sea ice strength parametrization has been switched on (STOCH_CPL). The uncoupled experiment STOCH_UNCPL was run for a period of 102 years; the two coupled integrations were extended to 201 years in order to account for the larger uncertainty generated by having two completely different realizations of the atmospheric trajectory (table 4.1). Note that all parameter values and parametrizations in FESOM for STOCH_UNCPL and STOCH_CPL are exactly the same, except for the sequences of random numbers that are used. In addition, initial conditions for all three simulations are the same.

Table 4.1: Summary of the experiments used in this study.

| Name | Stochastic | Coupled | Years |
|---|---|---|---|
| REF | No | Yes | 201 |
| STOCH_UNCPL | Yes | No | 102 |
| STOCH_CPL | Yes | Yes | 201 |

## 4.3. Results

In the following, the impact of the stochastic sea ice strength perturbations are described separately for Arctic and Antarctic sea ice. Effects on integrated quantities such as sea ice volume as well as regional impacts on variables such as sea ice thickness are analysed. Some explanations on how the stochastic sea ice strength perturbation affect Arctic and Antarctic sea ice will be proposed, focusing on the differing impacts of the stochastic parametrization in the uncoupled compared with the coupled simulation. Furthermore, the remote influence of the stochastic scheme on the climate in non-polar regions is explored.

### 4.3.1. Arctic sea ice

#### Volume

Figure 4.1 (*a*(i,ii)) shows the Northern Hemisphere sea ice volume and area of the two stochastic simulations and the reference simulation REF for March and September. Evidently, ECHAM6-FESOM simulates substantial Arctic sea ice variability throughout the year across a wide range of timescales. This appears to be rather consistent with observations and is discussed in more detail in *Sidorenko et al.* (2014) and especially by *Rackow et al.* (2014). The Arctic sea ice volume in the uncoupled set-up STOCH_UNCPL is highly correlated to that of REF owing to the fact that the sea ice has experienced effectively the same atmospheric forcing. However, STOCH_UNCPL shows a clear increase in Arctic sea ice volume when compared to REF (figure 4.1 (i)). The first 20–30 years can be seen as a transient phase during which Arctic sea ice volume builds up slowly. It is worth pointing out that the year-to-year increase in the sea ice volume is rather small during the transient phase; the fact that the quasi-equilibrium response in the Arctic owing to the stochastic sea ice scheme amounts to 10–20% after the first three decades of the integration can be explained through accumulation.

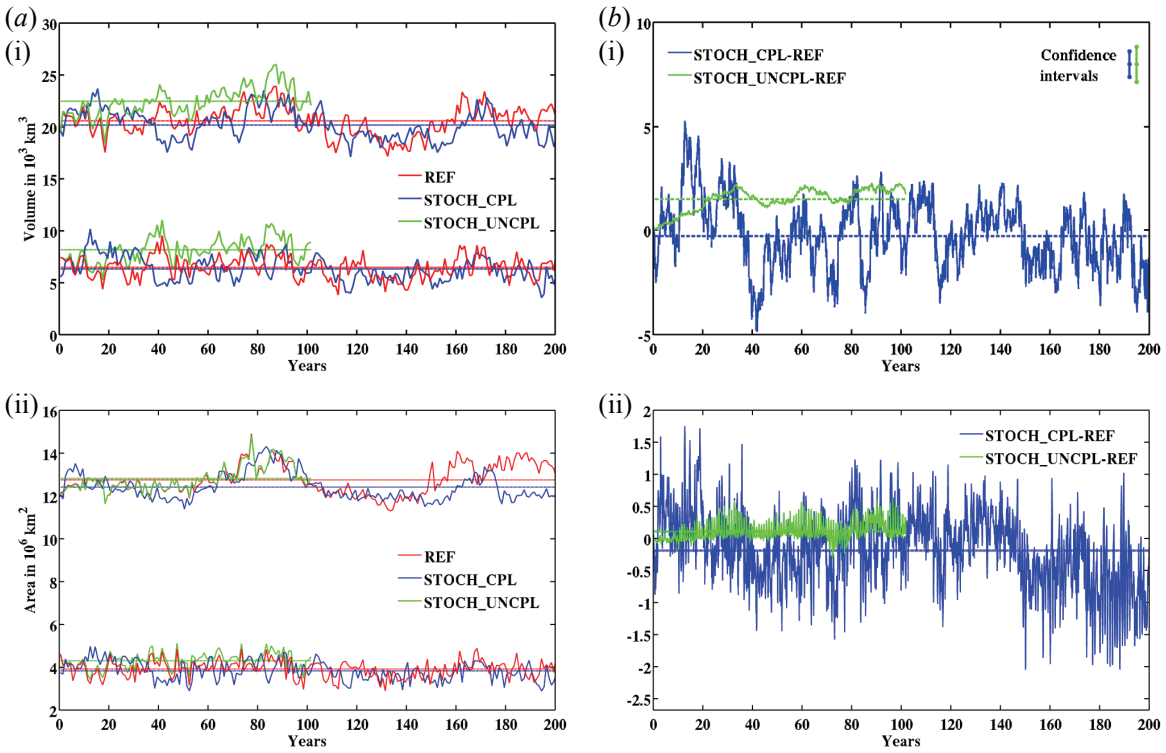


Figure 4.1: (*a*) Northern Hemisphere total (i) sea ice volume ($10^3$ km$^3$) and (ii) sea ice area ($10^6$ km$^2$) for REF (red), STOCH_CPL (blue) and STOCH_UNCPL (green); results are shown for March (upper curves) and September (lower curves). (*b*) Monthly mean difference in Northern Hemisphere (i) sea ice volume ($10^3$ km$^3$) and (ii) sea ice area ($10^6$ km$^2$) between STOCH_CPL and REF (blue) as well as STOCH_UNCPL and REF (green). Coloured horizontal lines show respective mean values. 95% confidence intervals—using a *t*-test with consideration of the reduction of effective sample size owing to a lag-1 autocorrelation (*Wilks*, 2011)—are given as vertical bars.

A possible explanation for the increase in sea ice volume with the stochastic sea ice strength parametrization has been given by *Juricke et al.* (2013). In summary, the symmetric stochastic perturbations of the sea ice strength effectively lead to a weakening of the ice cover owing to the highly nonlinear formulation of the internal forces of the sea ice. Low $P^*$ values are more effective at reducing sea ice strength and increasing plastic deformation under convergent drift than the high $P^*$ values are at preventing sea ice from piling up. Newly created areas of open water owing to the increased drift then enable increased sea ice production. After the transient phase, during which the sea ice volume has increased, a new mean state is established in which increased sea ice volume counteracts the effective reduction of sea ice strength. The sea ice thickness distribution function of STOCH_UNCPL is shifted towards higher ice thicknesses (not shown). Because sea ice thickness as well as the $P^*$ value act linearly on the value of the sea ice strength, larger ice thicknesses can compensate for low $P^*$ values.

In contrast to the uncoupled experiment, the mean sea ice volume in STOCH_CPL shows a slight decrease compared with REF. The 95% CIs included in figure 4.1 ($b$(i)) for the difference between STOCH_UNCPL and REF as well as STOCH_CPL and REF do not overlap. This indicates that the response of the Arctic sea ice volume to the stochastic sea ice parametrization in the coupled model is significantly different from that in the uncoupled set-up. This, in turn, suggests that a negative feedback involving the atmosphere is operating in the coupled system that prevents the Arctic sea ice volume from accumulating as observed in the uncoupled system. Given that the accumulation of sea ice in the uncoupled system is rather slow, a relatively weak negative atmospheric feedback would be sufficient to prevent the ice from accumulating in the coupled model. As a variety of strong feedback mechanisms are known to be present in the Arctic, it is difficult to provide a conclusive answer as to which negative feedback mechanism is crucial to explain the above results. Nevertheless, at the end of this section, a possible negative feedback is proposed that could serve as an explanation for the above-mentioned results.

### Area

Time series of Arctic sea ice area and changes therein owing to the use of the stochastic scheme are shown in figure 4.1 ($a$(ii),$b$(ii)). STOCH_UNCPL shows a slight increase in area at the end of the transient phase whereas sea ice area does not show a discernable trend for STOCH_CPL. The strong seasonal dependence of the impact of the stochastic perturbations on sea ice area has been described in *Juricke et al.* (2013) although the sign of the changes is different in this study. *Juricke et al.* (2013) explained the sea ice area decrease by an increased drift, away from areas of low concentration and divergence, towards coastlines and generally the western Arctic. This leads to reduced sea ice concentrations along the ice edge and in the eastern Arctic. Basically, this explanation also holds for STOCH_UNCPL during the first few years, when the stochastic sea ice parametrization also reduced the sea ice area. It should be noted, though, that the length of the integration in *Juricke et al.* (2013) is considerably shorter (17 years) and was forced by common ocean ice reference experiments (CORE) version 2 atmospheric forcing (*Large and Yeager*, 2009) which accounts for changes in atmospheric conditions owing to rising $CO_2$ concentrations.

### Regional impacts

Figure 4.2 highlights the regional changes in Arctic sea ice thickness and concentration. The left column shows the annual mean sea ice thickness and concentration distribution of the Arctic for REF, years 1–201. The middle and right columns illustrate the differences in the two distributions between STOCH_UNCPL and REF for years 1–102 and between STOCH_CPL and REF for years 1–201, respectively. Sea ice thickness shows a uniform increase throughout the entire Arctic in STOCH_UNCPL when stochastic sea ice perturbations are used. The increase in sea ice concentration occurs primarily in areas where the ice edge can be found during the melting and freezing seasons.

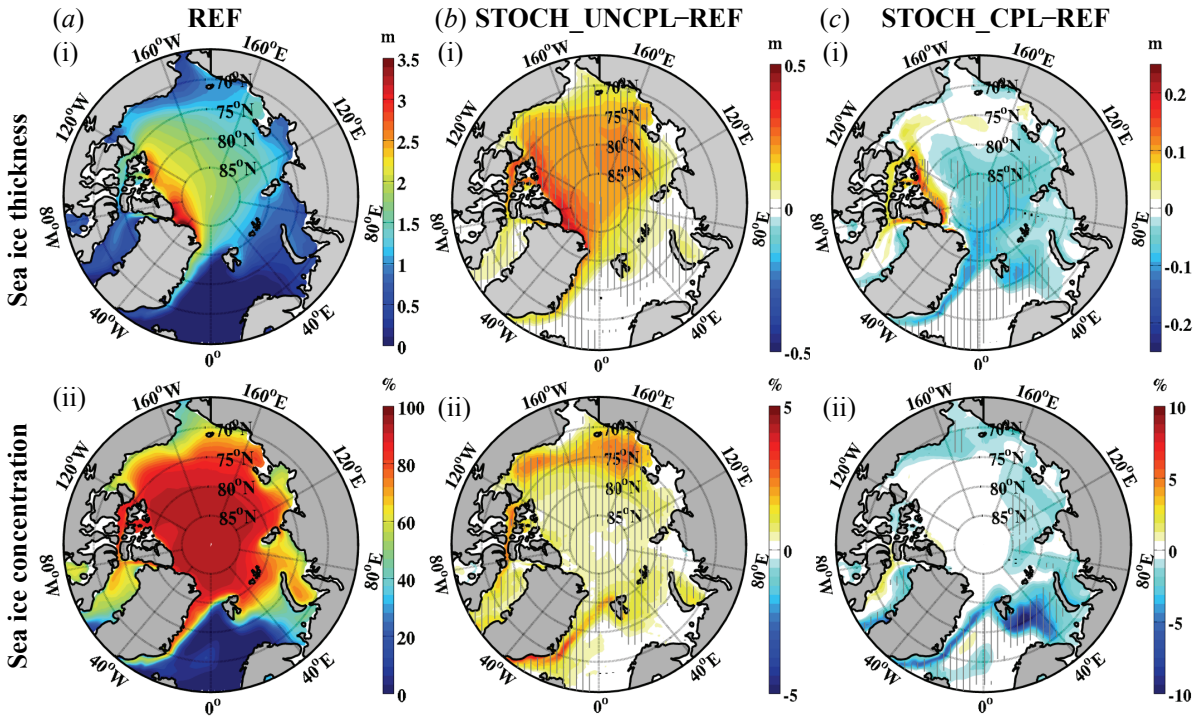


Figure 4.2: (*a*) Annual mean (i) sea ice thickness (m) and (ii) sea ice concentration (%) for REF, years 1–201. (*b*) Difference in annual mean (i) sea ice thickness (m) and (ii) sea ice concentration (%) between STOCH_UNCPL and REF, years 1–102. (*c*) Same as (*b*), but for the difference between STOCH_CPL and REF, years 1–201. Hatched areas indicate differences statistically significant at the 5% level, using a Wilcoxon signed-rank test for the paired samples of STOCH_UNCPL−REF and a Wilcoxon–Mann–Whitney rank-sum test for the independent samples of STOCH_CPL−REF (*Wilks*, 2011). Note the different contour intervals.

For the coupled stochastic simulation, a completely different picture emerges. For STOCH_CPL, sea ice thickness increase is limited to an area along the north coast of Greenland and the Canadian Arctic Archipelago area. The central and eastern Arctic, on the other hand, show reduced sea ice thicknesses. A somewhat similar pattern is found for sea ice concentration changes in STOCH_CPL. These patterns point towards a redistribution of sea ice cover and thickness from the east to the west as discussed above. Owing to the weakened ice, sea ice drift is increased. But while in the uncoupled case STOCH_UNCPL, this redistribution seems to

lead to an increase in sea ice production during the freezing season, which compensates for the drift and opening of leads, some atmospheric feedback mechanism appears to counteract this increased sea ice production in STOCH_CPL. As a consequence, sea ice is redistributed without any build-up in sea ice volume.

This hypothesis is further substantiated by figure 4.3, which shows sea ice drift along with its changes owing to the stochastic scheme. While in STOCH_UNCPL, sea ice velocities are slightly decreased in the central Arctic (anticlockwise arrows), they are increased in STOCH_CPL (clockwise arrows). The differences between the simulations can be explained as follows: during the transient phase of the integration, STOCH_UNCPL experiences a slight increase in sea ice velocities (not shown). The increased sea ice thickness distribution is still accumulating and increased sea ice thicknesses do not yet balance the influence from the effective weakening of the sea ice strength owing to the stochastic perturbations. After this transient phase, though, sea ice drift tends to be reduced, because thicker sea ice is capable of balancing the direct impact of the $P^*$ perturbations.

The velocity changes in STOCH_CPL are quite different. Most of the drift in the central Arctic is increased or slightly redirected towards the north coasts of Canada, the Canadian Arctic Archipelago and Greenland. Due to the fact that there is no accumulation in Arctic sea ice, the effective decrease in sea ice strength is not balanced. Therefore, the changes in the sea ice velocity field resemble more the transient phase of STOCH_UNCPL.

**Annual cycle**

Figure 4.4 illustrates the annual cycle of monthly mean sea ice volume, sea ice area and the thermodynamic growth rate for REF for the Northern as well as for the Southern Hemisphere ($a$(i– iii)); also shown are their changes when the stochastic sea ice parametrization is used ($b$(i–iii)). Sea ice volume in the Southern Hemisphere is only a fraction of that in the Arctic. This is especially true when the respective summer months are compared. For sea ice area, a similar behaviour is found with the exception that wintertime sea ice extent in the Antarctic exceeds that in the Arctic. The annual cycle of thermodynamic growth rates is very similar in the two hemispheres.

The influence of the stochastic sea ice parametrization on the annual cycle of Arctic sea ice volume in the coupled model follows that of the sea ice volume in REF (figure 4.4, bottom row) with the largest (smallest) absolute differences found in winter (summer). The influence of the stochastic parametrization in the uncoupled integration mostly lacks any seasonality and is much larger in magnitude. The response in STOCH_UNCPL, however, took several decades to fully develop. A comparison for the first few years of the STOCH_UNCPL integration yields much more similar results in the magnitude of changes for the coupled and uncoupled model (not shown). The seasonality of the response for sea ice area in both models is more similar than that for the volume. However, the response is shifted by about 0.3–0.4 $10^6$ km$^2$.

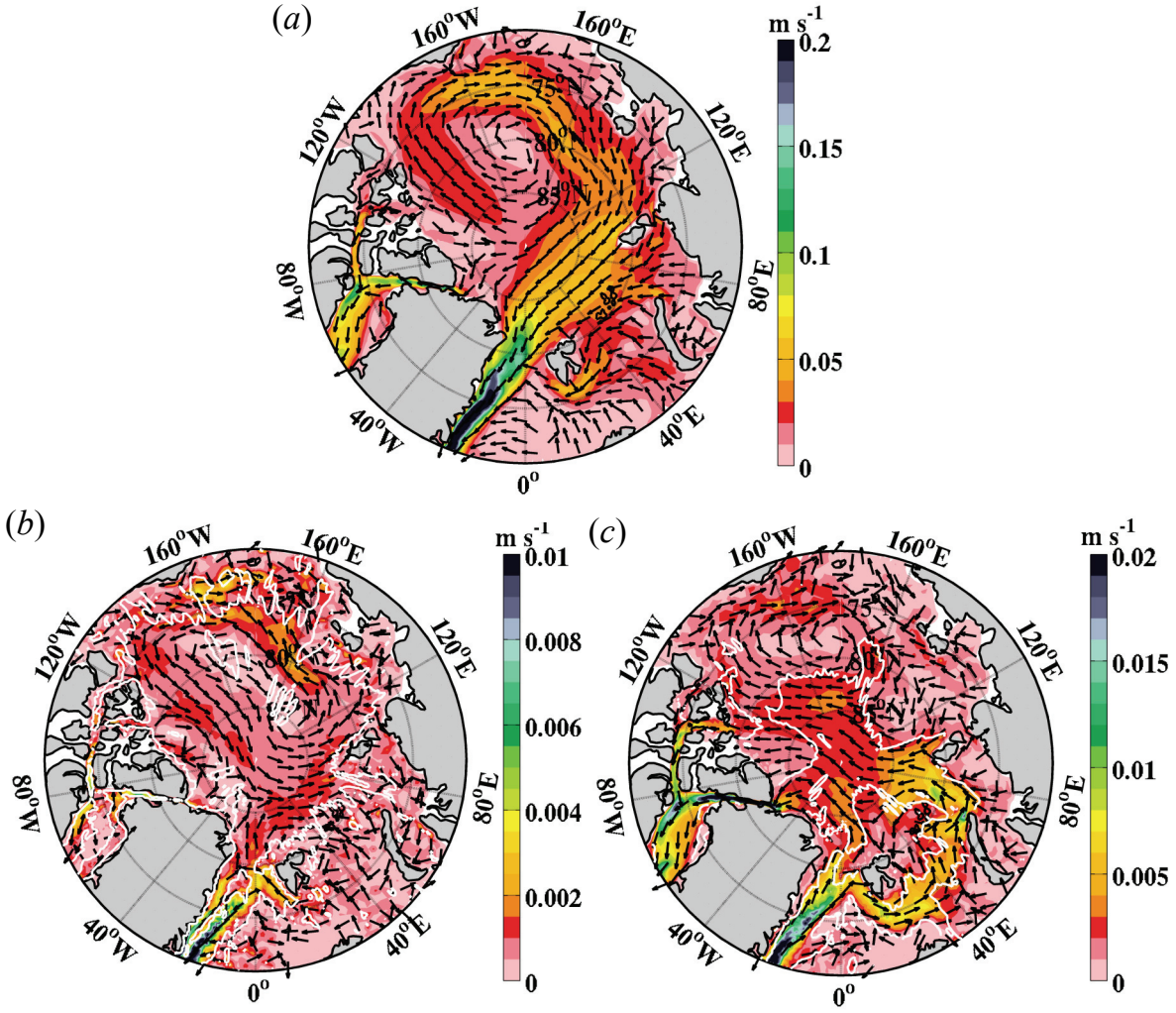


Figure 4.3: (*a*) Annual mean sea ice velocity ($\mathrm{m\,s^{-1}}$) for REF, years 1–201. (*b*) Difference in annual mean sea ice velocity ($\mathrm{m\,s^{-1}}$) between STOCH_UNCPL and REF, years 1–102. (*c*) Same as (*b*), but for the difference between STOCH_CPL and REF, years 1–201. Arrows are normalized and white contour lines enclose areas where the zonal and/or meridional velocity component is significantly different from zero at the 5% level, using the same tests as in figure 4.2. Note the different contour intervals.

### Growth rates and atmospheric feedback

Changes in the thermodynamic growth rates in the bottom right panel of figure 4.4 hint at a negative atmospheric feedback mechanism in STOCH_CPL. While for STOCH_CPL melting is reduced in spring and summer and freezing is reduced in autumn and winter, the opposite changes are found for STOCH_UNCPL. The behaviour of the response for STOCH_UNCPL can be explained as follows: shifting of sea ice during the freezing season opens up leads and creates open water areas. As fluxes are fixed and the atmosphere is seen as an infinite source or sink of heat in the uncoupled set-up, open water can freeze over and quickly produce more ice. This newly created ice then drifts away, and the process is repeated. On the other hand, sea ice thickness and concentration is increased in the areas of convergent motion, which leads

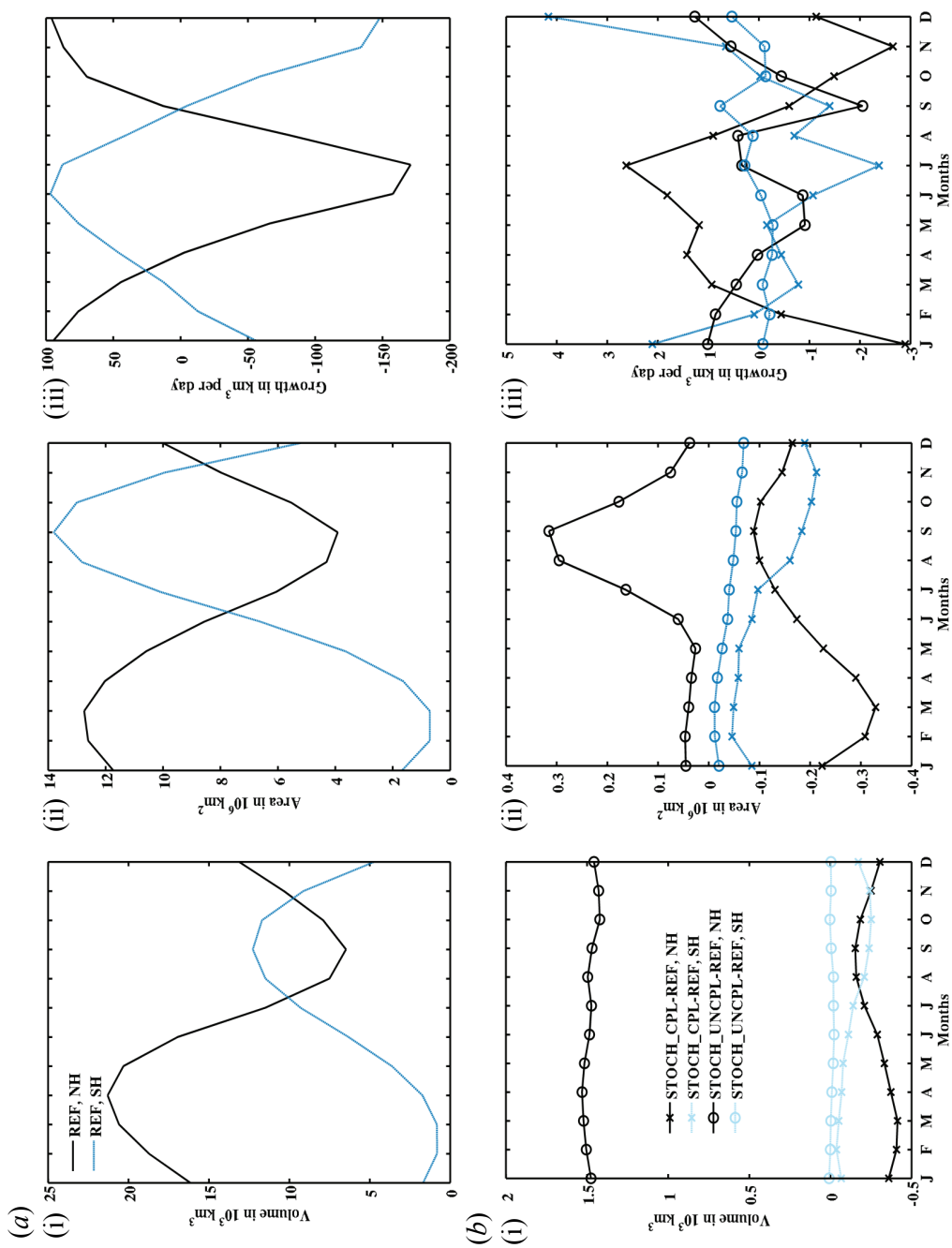


Figure 4.4: (*a*) Annual cycle of monthly mean (i) sea ice volume ($10^3\,\mathrm{km}^3$), (ii) sea ice area ($10^6\,\mathrm{km}^2$) and (iii) thermodynamic growth rates ($\mathrm{km}^3\,\mathrm{day}^{-1}$) for REF, years 1–201. (*b*) Difference in the annual cycle of monthly mean (i) sea ice volume ($10^3\,\mathrm{km}^3$), (ii) sea ice area ($10^6\,\mathrm{km}^2$) and (iii) thermodynamic growth rates ($\mathrm{km}^3\,\mathrm{day}^{-1}$) between STOCH_CPL and REF (crosses), years 1–201, as well as STOCH_UNCPL and REF (circles), years 1–102. Black is for the Northern Hemisphere and blue for the Southern Hemisphere.

to decreased growth rates in those regions. Still, the enhanced production of sea ice in areas of open water is stronger than the reduction of growth rates owing to increased plastic deformation. As a result mean growth rates and therefore sea ice volume are increased compared with the reference simulation. In the annual mean, the increase in sea ice growth rates during freezing seasons has a larger impact than the increase in melt during spring and summer, especially during the first 20–30 years of the transient phase.

For STOCH_CPL, the response to the stochastic sea ice parametrization is different. The atmosphere is no longer an infinite source or sink of energy, because it can respond to the sea ice changes. A feedback mechanism that explains the differences in the coupled and uncoupled set-up is connected to the sea ice thickness and opening of leads during autumn and winter. At the beginning of the freezing season production of sea ice is increased in the areas of open water created in the east by enhanced sea ice drift. But because the atmosphere in STOCH_CPL is now heated from the ocean, it reacts in the coupled system and becomes warmer over open water. This will reduce the heat loss of the ocean and hence freezing rates in open water; sea ice production in open water areas, consequently, is no longer sufficiently strong to compensate for the effect of reduced ice growth owing to piled up ice further to the west. Therefore, the mean growth rate is reduced in STOCH_CPL when compared with REF. Further support for the existence of such a negative feedback mechanisms comes from a slight increase in near-surface atmospheric air temperatures in January and February over the eastern Arctic, slightly increased (reduced) ocean temperatures in most of the eastern (western) Arctic and slightly reduced mixed layer depth in the central Arctic owing to reduced growth rates (not shown). In STOCH_UNCPL, these changes are very different, with generally slightly decreased ocean temperatures and increased mixed layer depth owing to an increase in growth rates and lower water temperatures (not shown). In summary, it is argued that in the coupled model the slight decrease in sea ice growth during winter owing to the stochastic sea ice scheme is sufficient to prevent a gradual build-up of sea ice volume in the Arctic that is observed in the uncoupled model.

### 4.3.2. Antarctic sea ice

#### Volume

The difference in effects between Northern and Southern Hemisphere sea ice is especially pronounced when the impact of the stochastic sea ice parametrization is considered in the uncoupled simulation (figure 4.4). While the volume increase in the Arctic is able to accumulate over time this is not possible in the Antarctic owing to the almost complete loss of sea ice in austral summer. Figure 4.5 shows the time series of monthly mean sea ice volume for the Southern Hemisphere, for March and September and all three simulations. The Antarctic sea ice volume strongly increases from its minimum in March to its maximum in September (see also figure 4.4 ($a$(i–iii))). Antarctic sea ice volume shows substantial interannual to decadal variability. Compared with the Arctic (figure 4.1), however, there is much less multi-decadal variability which again is consistent with a relative lack of memory owing to Antarctic sea ice loss in summer.

The right panel of figure 4.5 illustrates the differences in sea ice volume between the in-

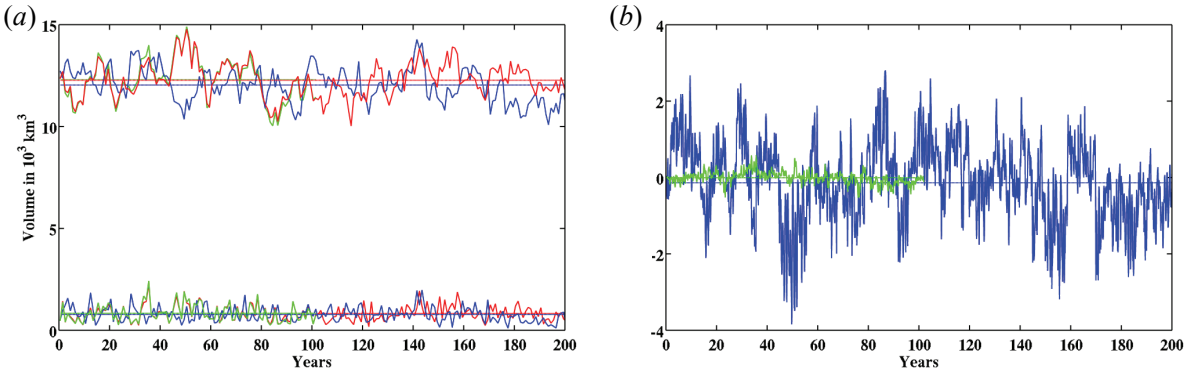


Figure 4.5: (*a*) Southern Hemisphere total sea ice volume ($10^3$ km$^3$) for REF (red), STOCH_CPL (blue) and STOCH_UNCPL (green); results are shown for March (lower curves) and September (upper curves). (*b*) Monthly mean difference in Southern Hemisphere sea ice volume ($10^3$ km$^3$) between STOCH_CPL and REF (blue) as well as STOCH_UNCPL and REF (green). Coloured horizontal lines show respective mean values.

tegration with and without the stochastic ice strength scheme for the uncoupled and coupled model. It is confirmed that in contrast to the Arctic there is no change in the mean Southern Hemisphere sea ice volume, neither for STOCH_UNCPL nor for STOCH_CPL. As sea ice area and volume are strongly reduced during the summer months changes in sea ice thickness can hardly accumulate over time.

### Regional impacts

The annual mean sea ice thickness distribution of REF and its changes resulting from the use of the stochastic parametrization are shown in figure 4.6. Sea ice is about two to three times thinner in the Southern Hemisphere than it is in the Northern Hemisphere. As a result, changes in thickness owing to the stochastic perturbations are also smaller than in the Northern Hemisphere. In addition, the distribution of landmasses is very different in the Northern Hemisphere; whereas the coastlines of the Canadian Arctic Archipelago present ideal conditions for a stochastic sea ice strength parametrization to have an impact on the mean state, such confining topographic structures are largely absent in the Southern Hemisphere high latitudes. Interestingly, the largest thickness changes in STOCH_UNCPL are located along the coast of Antarctica, where the stochastic scheme leads to increased sea ice thickness. Those are areas of convergent or shear drift where sea ice might also survive the melting season.

For STOCH_CPL, the changes are again somewhat different. Instead of sea ice piling up near the east coast of the Antarctic Peninsula, sea ice is drifted eastward. This leads to a shift of ice from the west to the east. In addition, the changes are larger in amplitude and in scale than in STOCH_UNCPL. One reason might be the stronger increase in eastward sea ice drift and the change in vertically integrated barotropic streamfunction of the ocean (not shown). The latter shows an enhanced eastward flow and enhanced gyre strength. Even though this is also observable in STOCH_UNCPL, the impact in STOCH_CPL is larger, with an annual mean increase of about 0.5–1 Sv compared with about 2 Sv for the Weddell Gyre, respectively.

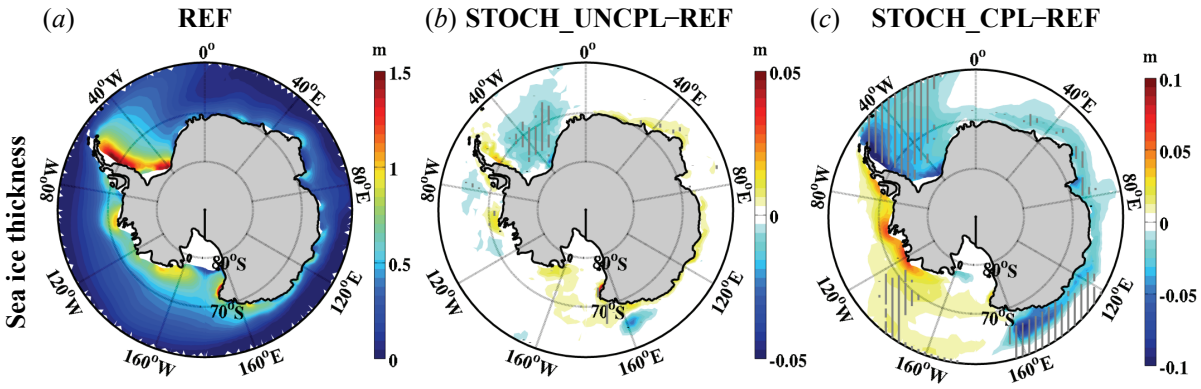


Figure 4.6: (*a*) Annual mean sea ice thickness (m) for REF, years 1–201. (*b*) Difference in annual mean sea ice thickness (m) between STOCH_UNCPL and REF, years 1–102. (*c*) Same as (*b*), but for the difference between STOCH_CPL and REF, years 1–201. Hatched areas indicate differences statistically significant at the 5% level, using the same tests as in figure 4.2. Note the different contour intervals.

### 4.3.3. Remote impacts

Figure 4.7 shows the time series of the annual mean Atlantic meridional overturning circulation (AMOC) at about 45°N and 1 km depth for all three simulations. As has been the case for the Arctic sea ice volume and area, the AMOC is highly variable with large variations from year to year. It should also be noted that the AMOC is correlated to the Arctic sea ice volume and area, as it transports heat to the north and is driven by the North Atlantic Deep Water formation which, in turn, influences or is influenced, respectively, by sea ice cover and growth rates (*Mahajan et al.*, 2011; *Jahn and Holland*, 2013).

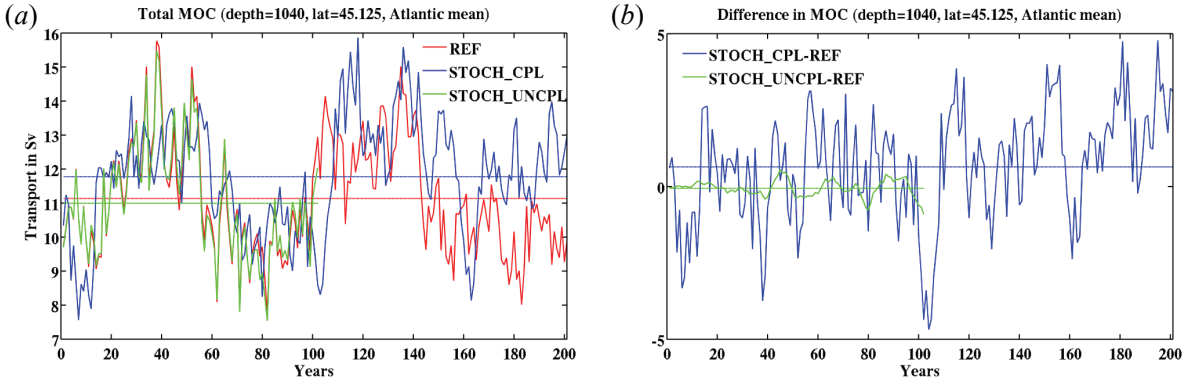


Figure 4.7: (*a*) Time series of the annual mean AMOC (Sv) at 45°N and a depth of approx. 1000 m for REF (red), STOCH_CPL (blue) and STOCH_UNCPL (green). (*b*) Corresponding time series of the difference in AMOC (Sv) between STOCH_CPL and REF (blue) as well as STOCH_UNCPL and REF (green). Coloured horizontal lines show respective mean values.

When looking at the differences between the stochastic simulations and REF in the figure 4.7 (*b*) no large change in the AMOC can be observed for STOCH_UNCPL. This is probably due to the fact that changes in sea ice thickness are mostly occurring in the central Arctic and are quite small from year to year. The increase in AMOC in STOCH_CPL is presumably just a result

of sampling variability caused by the multi-decadal variability of the AMOC. Similar results were found for other oceanic and atmospheric parameters in non-polar regions of the globe (not shown). In summary, it turns out that significant changes in the mean climate caused by the stochastic perturbations are very much confined to high latitudes.

## 4.4. Conclusion

A symmetric stochastic perturbation of the sea ice strength parameter based on *Juricke et al.* (2013) has been implemented in the coupled climate model ECHAM6-FESOM. A set of coupled and uncoupled multi-decadal experiments has been carried out in order to explore the impact that the stochastic sea ice parametrization has on the mean climate in coupled compared with uncoupled models.

In the Arctic, including a stochastic sea ice parametrization in an uncoupled sea ice–ocean model results in an increase in sea ice thickness and volume by some 10–20% (depending on the season). This increase can be explained by the fact that the stochastic perturbations of the sea ice strength lead to an effective weakening of the sea ice, because small stochastic values of the ice strength are more influential than large ones. As a result, convergent sea ice drift is enhanced, which leads to an accumulation of sea ice thickness in the central Arctic and especially along the coastlines in the western Arctic. The first 20–30 years of uncoupled integration with the stochastic scheme can be seen as a transient phase. During this phase, sea ice thickness increase accumulates and increased sea ice production in areas of newly opened water leads to an increase in sea ice volume. After the transient phase, the sea ice–ocean system reaches a new quasi-equilibrium state in which the increased sea ice thickness counteracts the effective weakening of the sea ice caused by the ice strength perturbations. Sea ice volume is no longer increased. In contrast to the Arctic, the influence of the stochastic sea ice parametrization on the mean climate of the Antarctic is relatively small in the uncoupled model. This can be explained by the fact that Antarctic sea ice almost completely vanishes during austral summer which inhibits the small temporal accumulation of stochastic effects.

The impact of the stochastic sea ice parametrization on the mean climate of the coupled model ECHAM6-FESOM turns out to be very different. The mean sea ice volume in the Arctic and Antarctic remains largely unchanged with the stochastic scheme switched on. In the Arctic, this can be explained by the fact that in an integrated sense the increase of sea ice thickness north of Greenland and the Canadian Arctic Archipelago is accompanied by a loss of sea ice in the central and eastern Arctic. This reflects the increased transport of sea ice from the eastern to the western Arctic which is also reflected in increased sea ice velocities. The same argument holds for the Antarctic. However, in the Southern Hemisphere, sea ice shows evidence of being increasingly transported eastward and changes in thicknesses are smaller than in the north.

The fact that the coupled system responds differently to a stochastic sea ice parametrization compared with an uncoupled model highlights the fact that care has to be taken when results from uncoupled experiments are extrapolated to the coupled climate system. The results suggest that by incorporating the atmosphere a negative feedback is introduced that prevents the stochastic effect in the coupled model from accumulating. Given the slowness of the accumula-

tion process in the uncoupled model (figure 4.1), it is likely that even a relatively weak negative atmospheric feedback would be sufficient to prevent the stochastic sea ice parametrization from influencing the mean climate of the coupled system. Given the strong variability of sea ice on a wide range of timescales, therefore, pinning down the exact negative mechanisms is challenging.

However, one reason for the discrepancies between the coupled and the uncoupled simulation might have to do with the atmospheric response (or lack thereof) to an increased amount of open water during the freezing season owing to the stochastic sea ice parametrization. In the uncoupled stochastic simulation, the fluxes are fixed, and therefore the atmosphere is prevented from adjusting and hence reducing the amount of sea ice production in open water areas. This unrealistically large productivity outweighs the effect of reduced sea ice growth in the western Arctic owing to increased sea ice thickness. In the coupled model, the incorporation of the stochastic scheme also leads to increased sea ice production in open waters; the magnitude of this ice growth, however, is much reduced owing to the adjustment of the overlying atmosphere. The adjustment of the atmosphere helps to reduce the sea ice production increase and, hence, the reduction of growth rates in the western Arctic owing to thicker sea ice becomes comparable or even larger than the increase in growth rates owing to the generation of open water through the stochastic sea ice parametrization.

The remote response of the climate system in non-polar regions to the incorporation of the stochastic sea ice strength scheme turns out to be rather weak. This may be a result of the fact that the mean response in the polar regions to the stochastic sea ice parametrization is relatively low and that the level of natural variability is high. However, it is also possible that the mean influence on the Atlantic overturning circulation is relatively weak, because the coupled model ECHAM6-FESOM is relatively insensitive to buoyancy anomalies in the Labrador Sea region (*Rackow et al.*, 2014). Given that Labrador Sea convection is believed to be strongly affected by freshwater anomalies of Arctic origin (*Dickson et al.*, 1988) a stronger response of the overturning might be found in other more sensitive models.

While the impact of the stochastic sea ice strength parametrization on the mean climate of the coupled model seems to be somewhat reduced when compared to the impact in the uncoupled model, it should be pointed out that tests in an ensemble prediction framework suggest that the stochastic sea ice parametrization does lead to additional spread during the early part of the integration (*Juricke et al.*, 2014). Hence, the stochastic parametrization described here might become useful when it comes to coupled data assimilation and uncertainty estimation in monthly and seasonal polar prediction. Another promising direction of future research will be to look at stochastic formulations of other sea ice aspects. Given the climate relevance of the sea ice–albedo feedback the development of a stochastic sea ice albedo scheme appears to be a promising way forward. In addition, the $P^*$ perturbations presented here might again show quite different effects on the mean climate when combined with other stochastic parametrizations of the sea ice model and/or using a different configuration of the parametrization, for example yet another more sophisticated spatial correlation scheme.

***Acknowledgments.*** We are indebted to our colleagues Dr Helge Goessling, Thomas Rackow and Dr Dmitry Sidorenko for various fruitful discussions during the course of this study.We also

thank the two reviewers for their helpful and much appreciated remarks and comments.

***Funding statement.*** This study benefited from support of the REKLIM and TORUS-MiKlip projects. Computational resources were made available by the German Climate Computing Center (DKRZ) through support from the German Federal Ministry of Education and Research (BMBF), project ba0771, and by the North-German Supercomputing Alliance (HLRN), project hbk00032.

# 5. Potential sea ice predictability and the role of stochastic sea ice perturbations[12]

[12]This chapter is about to be resubmitted to the *Geophysical Research Letters* under the title *Potential sea ice predictability and the role of stochastic sea ice perturbations* (see reference *Juricke et al.*, 2014). The original layout of the article was changed to match the layout of the dissertation. Differences in the text when compared to the final submitted version will most likely be minor. Referencing to figures and tables as well as citations were altered. They have been changed to match the respective layout in the rest of the dissertation. In addition, the bibliography and the supplementary material of the submission have been merged with the bibliography and the appendix of the dissertation, respectively. The abstract of the article was retained. My contributions to this article include most of the necessary implementations and model adjustments (for the exceptions see below), and the initialization as well as monitoring of the simulations. I carried out all of the diagnostics and the plotting of the results. Helge Gössling and I implemented the schemes for the initial condition perturbations together, including the scripts for the automated ensemble set-ups. The concept for the experimental set-up as well as the evaluation, assessment, and interpretation of the results were developed and conducted in discussions with my coauthors Helge Gössling and Thomas Jung. They have also corrected my original manuscript before first submission to the journal.
Please excuse any remaining inconsistencies with the other chapters of this dissertation originating from the general layout of the article, including differences in spelling, figure layout, acronyms, equations and phrasing.

**Abstract**

A stochastic ice strength parameterization is implemented in a global coupled model to assess how inclusion of uncertainty estimates in the sea ice model affects potential sea ice predictability estimates. Sets of ensemble forecasts employing different perturbation methods are investigated with regard to ensemble spread growth for ice thickness and concentration. Spread generated by atmospheric initial perturbations in a perfect model approach is compared to spread generated by ensembles with a relaxed perfect model assumption through incorporation of stochastic ice strength perturbations. 12-months integrations initialized in January and July are carried out. During the first weeks of the forecasts incorporation of ice strength perturbations significantly increases ensemble spread of ice thickness in the central Arctic and along coastlines when compared to ensembles with atmospheric initial perturbations only. The latter produce comparatively larger spread along the ice edge. Applying a combination of both, initial and ice strength perturbations, leads to a summation of spread from both sources during the first forecast weeks. Thereafter, ice thickness spread in the different ensembles converges to a similar level irrespective of the perturbation method. For the Antarctic, inclusion of ice strength perturbations does not lead to increased ice thickness spread for more than one day into the forecasts when compared to atmospheric initial perturbations. Results suggest that existing estimates of potential sea ice predictability on seasonal and annual time scales remain unchanged if uncertainty in the parameterized ice strength is accounted for. Ice strength perturbations become relevant, however, for sub-seasonal sea ice predictions and data assimilation.

## 5.1. Introduction

Predicting the climate of the polar regions is an important element for decision making in the high-latitudes. In this context there has been large increase in the demand for sea ice predictions leading to the development of sea ice prediction systems (e.g., *Chevallier et al.*, 2014; *Sigmond et al.*, 2013).

There will always be limits to the skill of weather and climate forecasts due to the chaotic nature of the climate system (e.g., *Lorenz*, 1963). This raises the question as to how much predictive skill will eventually be achievable. Recently, there have been a number of studies exploring the upper limits of predictability—or potential predictability—in the Arctic (e.g., *Koenigk and Mikolajewicz*, 2009; *Blanchard-Wrigglesworth et al.*, 2011; *Holland et al.*, 2011; *Tietsche et al.*, 2014) and the Antarctic (*Holland et al.*, 2013), on seasonal to interannual time scales. While these studies differ in the details of the approaches, models, and diagnostics used, they are based on the assumption that the model itself does not provide a source of uncertainty, that is, perfect knowledge of the initial state would result in a perfect prediction. In general, to estimate the limits of potential predictability using the perfect model assumption, small perturbations to the initial state are used to generate ensembles. The growth in ensemble spread is then compared to the level of interannual model variability. For example, if the ensemble spread of a seasonal sea ice volume forecast reaches the level of interannual variability, potential predictability of this quantity is lost.

Independently of the above-mentioned studies, there has been an increasing number of publications dealing with ways of how to represent model uncertainty. While in a deterministic model formulation the mean impact of the sub-grid scale processes on the resolved scale dynamics is simulated as best as possible, stochastic methods can be used to include higher order moments into the formulation of sub-grid scale parameterizations. Instead of using grid cell averaged impacts of the sub-grid scale processes, additional information such as the variability within a grid cell can be conveyed to the resolved dynamics. By adding this kind of noise, the simulated climate may be able to leave one trajectory to reach another, a transition that might previously have been unlikely. This is comparable to the idealized situation of two separated local potential minimums where a transition from one to the other can be more easily achieved by adding random perturbations. Including stochastic aspects in the model formulation may therefore not only improve the general representation of the sub-grid scale processes and the related uncertainties, but in addition may also improve the simulation of the large scale flow (*Palmer*, 2012). Uncertainties in the parameterizations of sub-grid scale processes have previously been estimated by the use of stochastic parameterizations (e.g., *Lin and Neelin*, 2002; *Bright and Mullen*, 2002; *Plant and Craig*, 2008; *Li et al.*, 2008; *Lott et al.*, 2012). In weather forecasts, incorporation of uncertainty estimates for the sub-grid scales has lead to an improved model performance (e.g., *Buizza et al.*, 1999; *Shutts*, 2005; *Jung et al.*, 2005; *Weisheimer et al.*, 2011). Furthermore, the impact of incorporating stochastic aspects in climate models has been analyzed in view of changes to the simulated mean climate (e.g., *Williams*, 2012; *Juricke et al.*, 2013; *Juricke and Jung*, 2014; *Brankart*, 2013).

In this study, potential predictability of sea ice is estimated in a coupled climate model

for which the perfect model assumption is relaxed by employing stochastic sea ice strength perturbations to represent uncertainties in the formulation of the rheology of the sea ice model. More specifically, the ensemble spread generated solely by atmospheric initial perturbations is compared to the spread that is generated when model uncertainty is accounted for by including the stochastic sea ice strength parameterization by *Juricke et al.* (2013) and *Juricke and Jung* (2014). In addition, ensembles comprising both, atmospheric initial perturbations and stochastic sea ice dynamics, are analyzed. The objective is to assess the validity of the perfect model assumption for potential sea ice predictability on sub-seasonal to seasonal time scales.

## 5.2. Experimental setup

### 5.2.1. Model

The ensemble experiments of this study were carried out with the global coupled model ECHAM6-FESOM. The atmospheric component ECHAM6 (*Stevens et al.*, 2013) of the Max-Planck-Institute for Meteorology in Hamburg is a spectral model employing a horizontal resolution of about 1.85° with 47 vertical levels up to 0.01 hPa (T63L47). ECHAM6 is coupled to the Finite Element Sea ice Ocean Model (FESOM) (*Danilov et al.*, 2004; *Wang et al.*, 2008; *Timmermann et al.*, 2009; *Sidorenko et al.*, 2011; *Wang et al.*, 2013), which has been developed at the Alfred Wegener Institute, Helmholtz Centre for Polar and Marine Research, through the OASIS3-MCT (*Valcke*, 2013) coupler. The effective resolution of the unstructured triangular ocean surface grid ranges from $\sim 150$ km in the open ocean to $\sim 25$ km near the coasts, in the Arctic, and along the equatorial belt. In the vertical the ocean model uses a tetrahedral grid with 46 unevenly spaced $z$-levels. The timesteps used for FESOM and ECHAM6 are 30 and 10 minutes, respectively, with coupling taking place every 6 hours. The mean sea ice thickness distribution simulated under present-day (1990) forcing is in good agreement with observational estimates (see figures C.1 and C.2 in appendix C), suggesting that the model is well suited for the experiments of this study. Further details regarding the model formulation and its performance in simulating the mean climate will be described in a study by Sidorenko et al. (D. Sidorenko, personal communication, 2014).

### 5.2.2. Simulations

The ensemble size for each of the following configurations and each start date is 10, with 15 start years for each setup, and initialization both on the first of January and first of July at 00:00 UTC. Ensembles are integrated for one year. The 15 start dates are separated by 10 year intervals and the initial conditions are provided by a multi-centennial ECHAM6-FESOM simulation under constant present-day (1990) forcing (D. Sidorenko, personal communication, 2014) after about 440 years into the integration. The 100-year period used for the initial perturbations consists of the first 100 years covered by the ensemble start dates. Sea ice fields are available at a 6-hourly resolution.

Four different sets of ensembles have been generated. In the first ensemble configuration (INI) integrations were initialized with atmospheric initial perturbations for the three-dimensional

wind (i.e. vorticity and divergence) and temperature using the random field method introduced by *Magnusson et al.* (2009). The method creates perturbations "in approximate flow balance" (*Magnusson et al.*, 2009) by adding down-scaled differences between two randomly chosen atmospheric states of the same time of the year (here from a 100-year control integration). The difference fields are scaled with the factor 0.1, giving on average perturbations of a similar magnitude as in *Magnusson et al.* (2009). Other than the described perturbations all initial fields for each of the members of the same ensemble are identical. This ensemble configuration serves as a reference for the estimation of potential sea ice predictability, without accounting for model uncertainty.

In the second ensemble experiment (STOCH) atmospheric and oceanic initial conditions were left unperturbed. Instead, ensemble spread was generated by the use of the stochastic sea ice strength parameterization described by *Juricke and Jung* (2014). This parameterization implements symmetric, Gaussian-like perturbations to the ice strength parameter $P^*$ of the elastic–viscous–plastic sea ice rheology. The parameter $P^*$ is not well constrained and cannot be measured directly, leading to large related uncertainties. Under the same sea ice conditions larger (smaller) values of $P^*$ reduce (increase) convergent sea ice drift, which is why $P^*$ is commonly used as a tuning parameter for the simulated sea ice distribution. The stochastic ice strength parameterization adds symmetric perturbations to the previously constant parameter $P^*$. The stochastic perturbations are correlated in time by a first order Markov process and in space by a predefined correlation matrix (*Juricke and Jung*, 2014). They are transformed into a limited and physically realistic range and applied to every ice covered ocean grid node during the course of the entire integration. The method therefore simulates uncertainties, including spatial and temporal variability, in the choice of the internal ice strength and thus in the resistance of the ice to plastic deformation under convergent motion. Due to the highly nonlinear formulation of the sea ice rheology and its important role in the formation of thick ice under convergence, incorporating this uncertainty estimate in the parameterization of the sea ice rheology is expected to lead to rapid ensemble spread generation in areas of convergent sea ice drift.

In the third ensemble configuration (STOINI) both, the initial perturbations described for INI and the stochastic sea ice strength parameterization used for STOCH, were employed. It therefore combines estimates of atmospheric initial condition uncertainty with estimates of model uncertainty in the simulation of the sea ice dynamics.

Finally, in the fourth ensemble experiment (FULLINI) atmospheric (including land-surface) initial states were chosen randomly (for the same calendar day) from the 100-year control integration also used for INI. This configuration allows to estimate the potential predictability of sea ice arising only from the memory inherent to the sea ice and ocean components, assuming a perfect model. It simulates a maximum level of uncertainty for the atmospheric initial states.

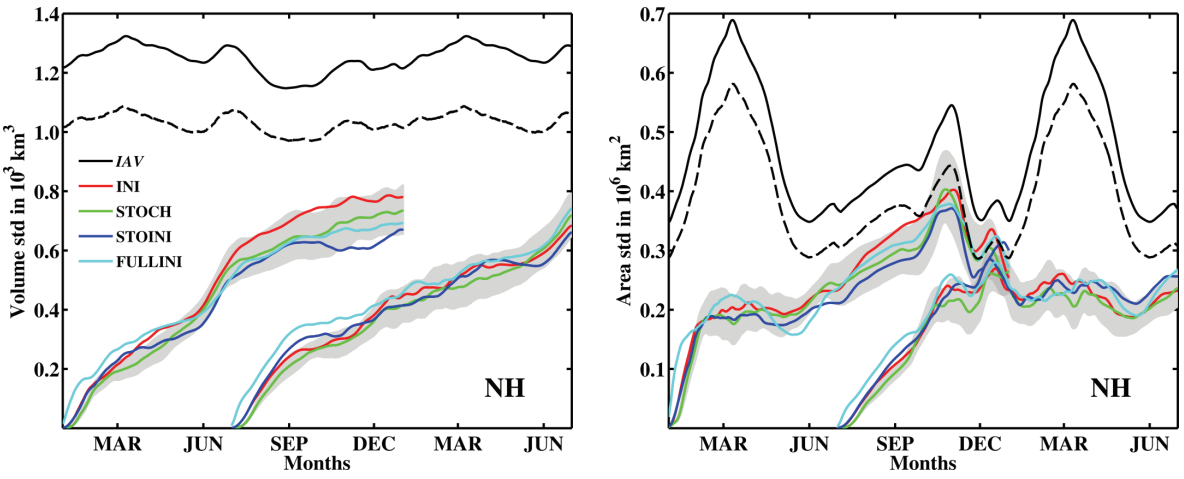


Figure 5.1: Ensemble spread (mean standard deviation of individual forecast ensembles) for Arctic sea ice (left) volume ($10^3\,km^3$) and (right) area ($10^6\,km^2$) for the four different ensemble configurations: atmospheric random field initial perturbations (INI, red), stochastic sea ice strength perturbations (STOCH, green), atmospheric random field initial perturbations combined with stochastic sea ice strength perturbations (STOINI, blue), and initialization with random atmospheric states (FULLINI, cyan). 12-months forecasts were started on 1st January and 1st July, 00:00 UTC. Also shown is the annual cycle of the interannual standard deviation from the control simulation (*IAV*, black). The 6-hourly data have been smoothed by a seven-day running-mean filter. The gray shaded area is the 95% confidence interval for STOCH and the dashed line marks the lower limit of the 95% confidence interval for *IAV*, using bootstrapping with 1000 samples.

## 5.3. Results

### 5.3.1. Arctic

The spread evolution of ensemble predictions for integrated Arctic sea ice quantities as a function of lead time is shown in figure 5.1 for the four different experiments. The ensemble spread of sea ice volume and area in the Arctic stays below the level of interannual variability throughout the 12-months forecast period. Differences between individual ensemble members are smaller than those of randomly drawn sea ice states, suggesting that Arctic sea ice area and especially volume are potentially predictable at least 12 months ahead. This result is consistent with previous studies (e.g., *Tietsche et al.*, 2014).

Large differences between the different ensemble configurations concerning ensemble spread of Arctic sea ice volume and area emerge during the first days and weeks of the forecasts, that is, during a period of relatively strong perturbation growth. Figure 5.1 suggests that the spread grows most rapidly for FULLINI followed by STOINI, INI and STOCH. During the first weeks of the forecast these differences are significant, as the confidence intervals for the ensembles are small.

An important finding of this study is, though, that the growth of the spread for the different ensemble experiments is comparable one month into the forecast and beyond (figure 5.1), as confidence intervals for the ensemble spread increase rapidly. This suggests that previous

estimates of potential seasonal sea ice predictability remain largely unchanged if uncertainty in the sea ice dynamics of the models is accounted for by employing a stochastic sea ice strength parameterization. Furthermore, details on how atmospheric perturbations are generated play a secondary role in estimates of potential sea ice predictability on seasonal to interannual time scales.

The average ensemble spread of sea ice thickness during winter and summer for INI 5 days into the forecasts is shown in figure 5.2 together with the corresponding interannual sea ice thickness variability (top two rows). The ensemble spread is more than one order of magnitude smaller than the interannual variability, highlighting the importance of sea ice initialization for relatively short-term sea ice predictions. The largest ensemble spread is found close to the ice edge, where atmospheric perturbations can have a large impact due to the presence of strong sea ice thickness and concentration gradients; comparably small values are found in the interior of the Arctic where sea ice thickness is relatively homogeneous and concentrations are high.

In figure 5.2, third row, the spread in sea ice thickness generated by the initial atmospheric perturbations is compared to the spread obtained from stochastic sea ice strength perturbations after 5 days. Evidently, the stochastic sea ice scheme provides significantly more spread during boreal winter in the region of large sea ice thickness north of Greenland and the Canadian Arctic Archipelago (CAA), that is, in a region where continuously thick and relatively immobile sea ice prevents atmospheric perturbations from having a sizable impact. Additional spread with stochastic sea ice perturbations is also found in the interior of the Arctic, both during boreal summer and winter. In summary, the stochastic ice strength perturbations of STOCH primarily induce significantly increased sea ice spread in the internal ice pack during the first couple of days, due to the increased variability of the internal ice strength. In these regions the internal forces of the sea ice are the main opposing forces to atmospheric stresses in the simulation of the sea ice dynamics and therefore largely determine sea ice velocities. Atmospheric perturbations transfer rather rapidly to sea ice, though, and propagate from the ice edge towards the central ice pack. Therefore, spread gain in STOCH is surpassed almost everywhere by INI within the first two weeks.

When atmospheric initial and ice strength perturbations are combined in STOINI, the spread generated by the individual configurations adds up and shows generally larger spread in STOINI than in INI after 5 days (figure 5.2, 4th row). This accumulative effect disappears after a few weeks, though, as the spread of STOINI and INI become basically indistinguishable (not shown). The ensemble spread of FULLINI stays significantly above levels of the other three configurations during the first months (not shown), but eventually all configurations settle at a similar level of spread (see figure 5.1).

Given the computational burden of running large ensembles, potential predictability estimates tend to suffer from sampling issues due to the use of relatively small ensemble sizes, especially when it comes to producing spatial maps of potential predictability. The fact that the different ensemble experiments carried out in this study show similar levels of spread several months into the forecasts allows us to generate a super ensemble. The difference between the interannual standard deviation of monthly mean sea ice thickness and the average spread of the super ensemble for monthly mean sea ice thickness for the last forecast month is shown in figure

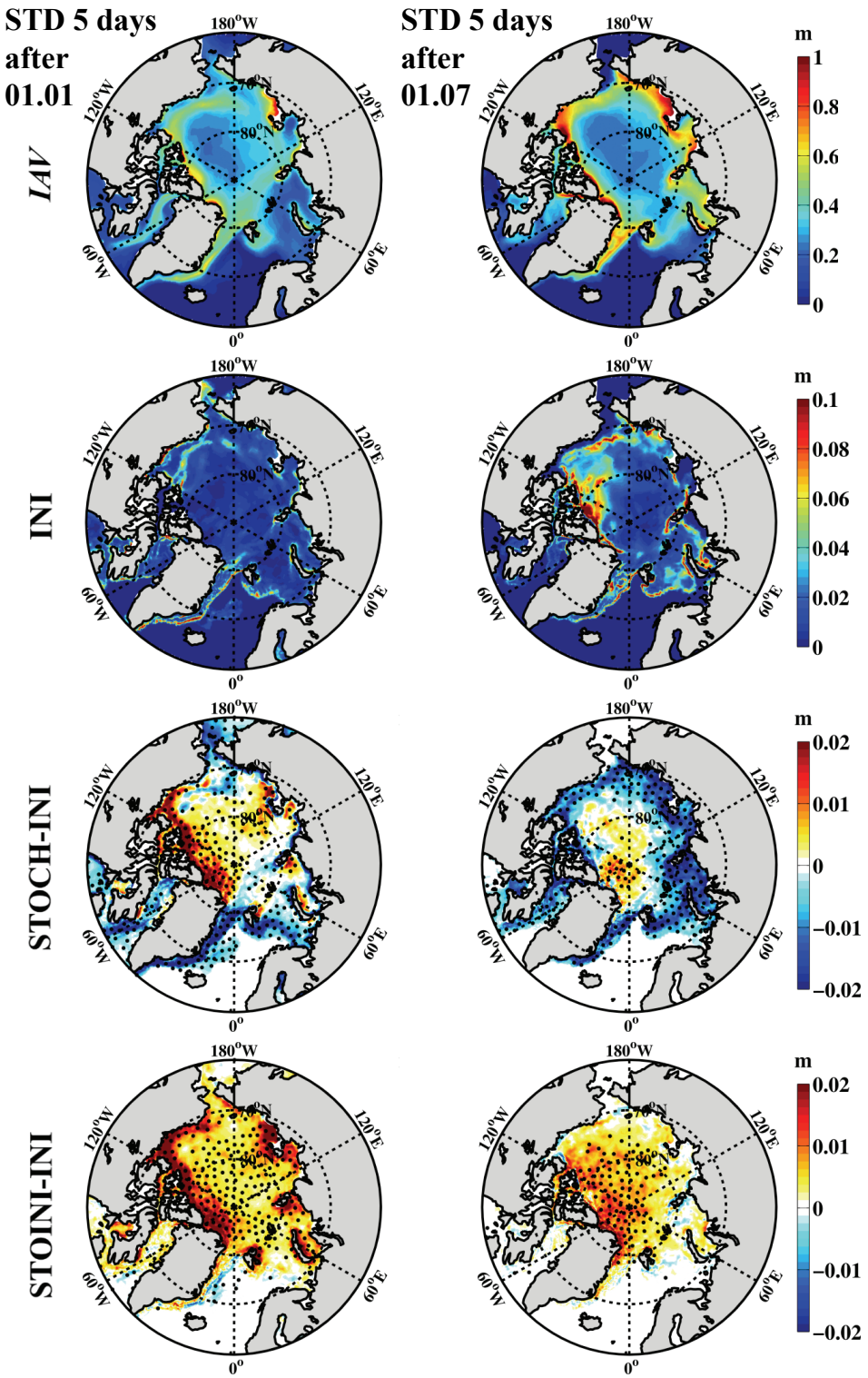


Figure 5.2: Sea ice thickness standard deviation (m) 5 days after the initialization on (left) 1st January and (right) 1st July, 00:00 UTC. Top row: interannual sea ice thickness standard deviation *IAV* of the control integration for the respective day. Second row: mean ensemble spread of INI after 5 days. Third row: difference in mean ensemble spread between STOCH and INI after 5 days. Fourth row: difference in mean ensemble spread between STOINI and INI after 5 days. Stippled areas indicate differences statistically significant at the 5% level, using an $F$-test. Note the different contour intervals.

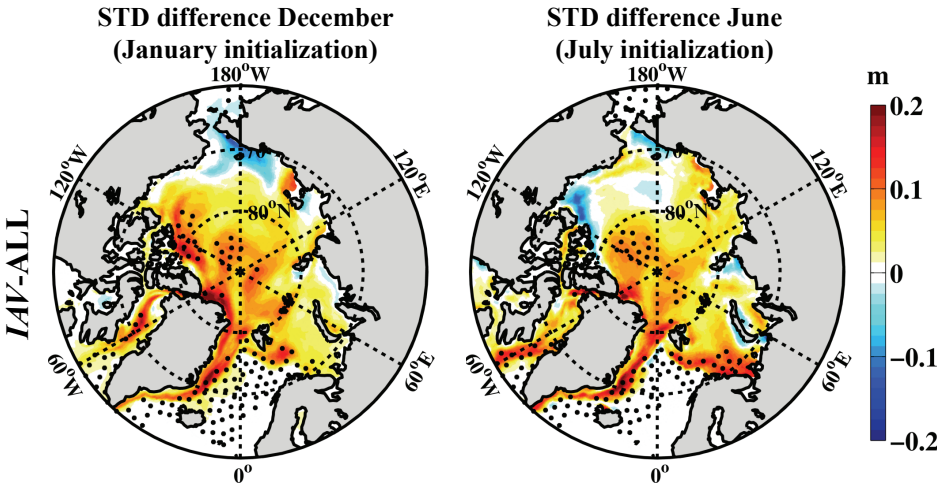


Figure 5.3: Difference between the interannual standard deviation *IAV* of sea ice thickness and the ensemble mean sea ice thickness standard deviation of the super ensemble ALL (m), for the 12th forecast month and each of the two initialization months. Mean standard deviation of ALL is calculated as the mean of the 10-member ensemble standard deviations, averaged over all 15 start dates and all four ensemble configurations (a total of 600 1-year-integrations for each of the two initializations: 4 configurations × 15 start dates × 10 members). Stippled areas indicate differences statistically significant at the 5% level, using an $F$-test with consideration of the reduction of effective sample size of *IAV* owing to a lag-1 autocorrelation (*Wilks*, 2011).

5.3. Although the significant differences (suggesting potential predictability) are confined to the ice edge and the central Arctic, only in the Bering Strait in boreal winter, and in some regions of the southern Beaufort Gyre and close to the coasts in boreal summer, predictability is most certainly lost. Overall, the interannual standard deviation is larger than the spread of the super ensemble for most regions, confirming considerable potential predictability of Arctic sea ice at least one year ahead. This is consistent with the findings of, for example, *Tietsche et al.* (2014).

### 5.3.2. Antarctic

So far, sea ice predictability studies have focused on the Arctic, with some exceptions (*Holland et al.*, 2013). Consequently, relatively little is known about Antarctic sea ice predictability. In the following potential sea ice predictability in the Antarctic will be investigated as well using the experiments described above. Figure 5.4 (left) shows the spread evolution of the ensemble predictions for integrated Antarctic sea ice volume as a function of lead time for all experiments. As was the case for the Arctic, an important result is that ensemble spread of Antarctic sea ice volume stays below the level of interannual variability for the entire 12-months forecast period, suggesting potential predictability for this quantity at least one year ahead. Results are almost identical for Antarctic sea ice area (not shown), because Antarctic sea ice volume and area are strongly correlated due to the virtual absence of thick multiyear ice. The spread generated by the different ensemble configurations converges more rapidly in the Antarctic compared to the Arctic. However, as in the Arctic, initial spread growth in the integrated sea ice quantities in the Antarctic is largest for FULLINI, followed by STOINI and INI, and, lastly, STOCH (not

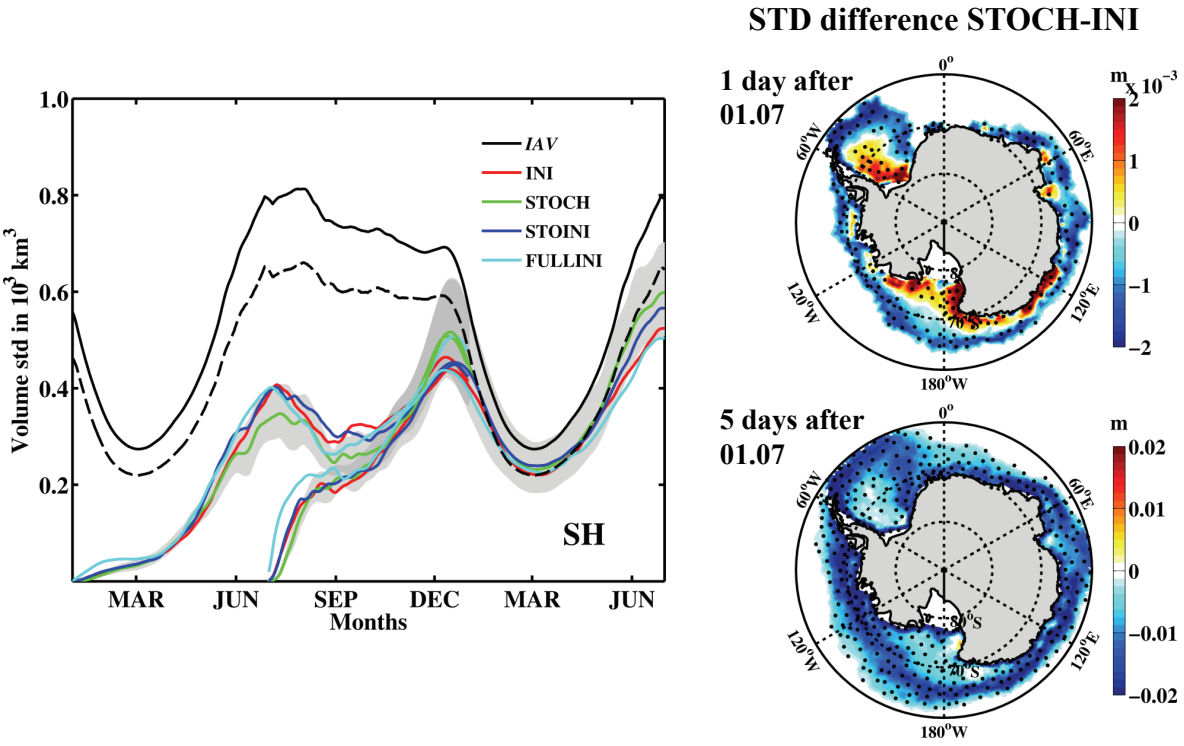


Figure 5.4: Left: as in figure 5.1, but for the entire Antarctic sea ice volume. Right: as in figure 5.2 but for the Antarctic sea ice and the difference between STOCH and INI, (top) 24 hours and (bottom) 5 days after the initialization on 1st July, 00:00 UTC. Note the different contour intervals.

shown).

Regional distributions of Antarctic sea ice spread growth of the four ensemble configurations reveal large differences to the Arctic (figure 5.4, right). Only during the first day of the forecast STOCH produces slightly, but nevertheless significantly larger sea ice thickness spread near coastlines compared to INI (figure 5.4, top right). Thereafter the atmospherically induced sea ice spread of INI is nearly everywhere significantly larger than the spread generated by STOCH (figure 5.4, bottom right). Accordingly, spread levels of STOINI and INI converge within a few days (not shown). The fact that Antarctic sea ice is comparatively thin and exhibits little dynamically formed thick multiyear ice results in a more pronounced impact of atmospheric variability on Antarctic sea ice spread compared to the role of ice strength uncertainties in the sea ice dynamics.

## 5.4. Discussion

The potential predictability of sea ice has been investigated using different atmospheric initial perturbation techniques and by relaxing the perfect model assumption through the use of a stochastic sea ice strength parameterization. It is found that sea ice exhibits considerable potential predictability on seasonal time scales, both for the Arctic and the Antarctic. From the

ensemble experiments of this study it can be concluded that the potential predictability of sea ice at forecast lead times from a few months to a year depends rather little on the details as to how atmospheric initial uncertainty is represented; in this forecast range, adding stochastic sea ice perturbations also has a negligible influence on ensemble spread and hence potential predictability estimates.

On daily to sub-seasonal time scales, incorporation of stochastic sea ice strength perturbations in coupled model forecasts plays a surprisingly large and specific (compared to atmospheric initial perturbations) role in generating ensemble spread, especially for the Arctic. While initial atmospheric perturbations tend to produce large sea ice spread near the ice edge at short lead times, with the induced spread gradually propagating towards the central ice pack, stochastic ice strength perturbations act primarily on deformed ice under convergent motion in the central Arctic and north of Greenland and the CAA. Differences in ensemble spread relatively early on in the forecast may have important implications, given that sub-seasonal prediction is an area of growing relevance (e.g., *Vitart*, 2014) and given that proper representation of initial and model uncertainty is crucial when it comes to developing advanced data assimilation systems.

Because the amount of thick multiyear ice is much larger in the Arctic than in the Antarctic, the impact of stochastic sea ice strength perturbations on initial ensemble spread growth is less pronounced for Antarctic sea ice: the different ensemble experiments (with and without incorporation of atmospheric initial and/or sea ice model uncertainty) converge more rapidly to a similar level of spread. In summary, including stochastic sea ice strength perturbations to account for model uncertainty in the simulation of sea ice dynamics seems to be of greater relevance for the Arctic than for the Antarctic.

In the future, employing a more complete set of uncertainty representations in the sea ice model, for example in the albedo parameterization, might lead to different impacts on potential predictability estimates.

***Acknowledgments.*** This study was supported by the TORUS-MiKlip project. Computational resources were made available by project ba0771 of the German Climate Computing Center (DKRZ) through support from the German Federal Ministry of Education and Research (BMBF), and by project hbk00032 of the North-German Supercomputing Alliance (HLRN).

# 6. Summary and conclusions

The main focus of this dissertation is the application of stochastic sea ice strength perturbations as a measure of model uncertainty in the context of climate and ensemble predictions. To this end I have developed a perturbation scheme and tested it in a sea ice–ocean as well as in a sea ice–ocean–atmosphere model and evaluated the impact of the perturbations with respect to changes in the simulated climate and to the spread generation and evolution in ensemble simulations.

The ice strength parameter is crucial when it comes to simulating the sea ice drift under conditions of convergent motion, where it impacts on the onset of plastic sea ice deformation. Low values of the sea ice strength parameter weaken the ice and lead to a relative increase in sea ice drift under convergence, whereas high values simulate a more compact, resistant sea ice cover where sea ice drift under convergence is more strongly decelerated. As this value is very uncertain due to its role as a tuning parameter and missing observations, a symmetric perturbation during the course of the sea ice simulations was applied to simulate the uncertainty, temporally and spatially.

**Stochastic ice strength perturbations in a sea ice–ocean model**

In chapter 3 of this dissertation three different strategies to perturb the ice strength parameter in the modelling of the sea ice dynamics in a sea ice–ocean model have been introduced. The three perturbation methods differ in the way they simulate spatial and temporal correlations:

- The first method has no spatial correlation for the ice-covered nodes of the mesh. All nodes receive independently perturbed ice strength parameters. A simple time correlation is applied by keeping the perturbations fixed for a given amount of time steps and choosing new, independent perturbations afterwards for the next fixed time interval.
- The second method is similarly not applying any spatially correlated perturbations, but uses a Markov process to generate a more sophisticated temporal correlation for the perturbations.
- The third method applies the same temporal correlation as the second method, but additionally incorporates some form of spatial correlation. Perturbations for nodes with common neighbours are spatially correlated.

All three perturbation schemes have been implemented in the Finite Element Sea ice–Ocean Model FESOM and tested in multi-annual sensitivity simulations. Results showed that all

three perturbation strategies lead to an increase of Arctic sea ice volume and increased sea ice thicknesses in the central Arctic and along coastlines compared to a reference simulation with a deterministic, spatially and temporally fixed ice strength parameter.

The inclusion of spatial correlation has the largest impact when it comes to changes in mean Arctic sea ice distribution caused by the uncertainty estimates for the ice strength parameter, followed by the method using the Markov process time correlation, but no spatial correlation. This shows that a more sophisticated perturbation strategy can have a strong impact on the mean response of the stochastic parameterization.

The general increase of Arctic sea ice volume and central Arctic sea ice thickness is caused by the fact that the parameterization of the sea ice rheology is highly nonlinear. Therefore, changes in the ice strength parameter have a nonlinear impact as well. In this context, randomly small values of the ice strength have a stronger impact on sea ice distributions than large values. When values are small, sea ice drift and plastic deformation under convergence is increased and leads to thicker ice. High values on the other hand decrease sea ice drift and plastic deformation, but do not lead to a decrease in sea ice thickness. Instead they impede the thickness increase, but only as long as high ice strength parameter values prevail. Summarizing, small values lead to increased ice thicknesses that cannot be reversed by high values. Additionally, due to the resulting effectively increased sea ice drift, open water areas emerge where new ice can form rapidly. This is then drifted away and accumulated in the central Arctic, leaving again open water areas to produce more ice. This effect leads to the increase in sea ice volume compared to the deterministic reference simulation with a fixed ice strength parameter.

Furthermore, for the perturbation scheme using temporal and spatial correlations an ensemble simulation was conducted, using for each ensemble member different sets of random numbers for the perturbations. The ensemble simulation showed that the largest sea ice thickness ensemble spread due to stochastic ice strength perturbations is generated in the central Arctic and along the coastlines. It exceeds interannual model spread by a factor of more than 2 along the northern coast of Greenland and the Canadian Arctic Archipelago. Near the ice edge ensemble spread is small. This is owing to the fact that the effects of the uncertainties in the sea ice rheology are of greater relevance in areas of thick, compact sea ice, where the term of the internal ice strength plays a major role in the momentum balance.

**Stochastic ice strength perturbations in a sea ice–ocean–atmosphere model**

In chapter 4 the impact of incorporating spatially and temporally correlated ice strength perturbations in the fully coupled sea ice–ocean–atmosphere model ECHAM6-FESOM was investigated. The purpose was to analyze the responses to the ice strength perturbations in a sea ice–ocean model compared to a sea ice–ocean–atmosphere model in view of atmospheric feedbacks. The spatial correlation strategy introduced in chapter 3 was revised to allow for spatial correlations between the grid nodes following a predefined decorrelation distance. This made it possible to increase the spatial patterns of the perturbations and to generate patterns more or less independent of the structure of the mesh.

Several climate integrations were carried out:

- a fully coupled reference simulation
- a sea ice–ocean simulation with stochastic ice strength perturbations using the atmospheric fluxes generated by the reference simulation as atmospheric forcing
- a fully coupled simulation with stochastic ice strength perturbations

Results showed that the responses to the ice strength perturbations in the fully coupled and the sea ice–ocean model were significantly different, both for Arctic and Antarctic sea ice.

For the uncoupled sea ice–ocean simulation with ice strength perturbations the response on the Arctic sea ice thickness distribution is basically similar to what has been observed in chapter 3: a slowly accumulating increase in sea ice thickness in the central Arctic and along coast lines compared to the reference simulation. This is accompanied by an increase in sea ice volume during the first few decades and a stabilization of the increased sea ice volume thereafter.

In the coupled sea ice–ocean–atmosphere model, however, Arctic sea ice volume is not increased. Even though sea ice drift is effectively increased—as has been the case for the uncoupled simulation during the accumulation period—this does not result in increased sea ice volume. Instead, the sea ice thickness distribution experiences a shift from the east to the west, especially to the northern coast of Greenland, the Canadian Arctic Archipelago and into the southern Beaufort Gyre. While this redistribution leads to increased sea ice production over newly created open water areas in the eastern Arctic in the uncoupled simulation, this increased production is reduced in the coupled simulation due to an atmospheric feedback. The atmosphere is heated in the coupled simulation by the ocean during the freezing season and hence production of sea ice over open water is reduced, owing to decreased fluxes. Even though this feedback is rather small, it is capable of preventing the increase in sea ice volume observed in the uncoupled simulation, where atmospheric fluxes are prescribed. This is because of the relatively small year-to-year impact of the stochastic perturbations that unfold their true potential to change the mean state only when accumulated over many years.

For the Antarctic, results are generally different, for both simulations. Antarctic sea ice is comparatively thin, the amount of dynamically formed multiyear ice is small and sea ice is strongly reduced during austral summer. Therefore, no large accumulative effect is visible, neither for the uncoupled nor the coupled stochastic simulation, when compared to the deterministic reference simulation. Instead, eastward drift is increased, more so in the coupled simulation, leading to a slight shift of the sea ice thickness distribution from west to east.

**Stochastic ice strength perturbations in a sea ice–ocean–atmosphere model in the context of potential sea ice predictability**

In chapter 5 the stochastic ice strength perturbations are used to generate ensembles with ECHAM6-FESOM in the context of potential seasonal sea ice predictability. The spread generated by ensembles with stochastic ice strength perturbations is compared to the spread generated by ensembles with perturbed atmospheric initial conditions. The aim is to challenge the perfect model assumption commonly used in potential predictability studies, where the model is

assumed to be perfect with the only uncertainties residing in the initial conditions (most studies merely address initial condition uncertainty pertaining to the atmosphere).

Results show that integrated sea ice quantities such as sea ice volume and area in both hemispheres are potentially predictable with lead times of one year, irrespective of whether uncertainty estimates in the sea ice strength parameterization are included or not. This is also true for most regions when sea ice thickness distributions are analyzed.

On daily to sub-seasonal time scales however, incorporation of stochastic sea ice strength perturbations leads to larger sea ice thickness ensemble spread growth in the central Arctic when compared to ensemble spread generated by solely atmospheric initial perturbations. This has implications for uncertainty estimation in sub-seasonal forecasts and data assimilation, where sea ice thickness ensemble spread is generally too low when compared to the models root mean square error (which, ideally, should be captured by the ensemble spread, see e.g. diagnostics for forecasting systems in *Doblas-Reyes et al.*, 2009; *Berner et al.*, 2011; *Weisheimer et al.*, 2011).

For the Antarctic, increase of sea ice ensemble spread due to the stochastic sea ice strength perturbations is only observable during the first few days of the forecast and is superseded by the spread generated by atmospheric initial perturbations thereafter. This suggests that accounting for uncertainties in the parameterization of the sea ice rheology is of minor importance regarding sea ice model spread in the southern hemisphere.

### Conclusions

In summary, incorporating uncertainty estimates in the parameterization of the sea ice rheology has significant impacts on model simulations of sea ice, not only in the context of ensemble spread generation, but also concerning shifts in the simulated mean sea ice distribution. This is especially noteworthy as the schemes included up to now are only addressing the uncertainty of one single parameter. Incorporating additional uncertainty estimates in other parts of the (coupled) model might lead to an even larger impact. Additionally, it is found that results of implementations in a less complex model should only be extrapolated to a more sophisticated model with utmost care, as the responses might be very different and unexpected.

In general, the schemes that I have introduced in chapters 3 to 5 for perturbing the sea ice strength parameter can basically be used to perturb any parameter within a climate model to include a first estimate of the inherent uncertainty.

# 7. Outlook

The field of model uncertainty estimation for global coupled climate simulations is still developing and numerous questions remain to be answered. Some of those might be tackled by the methods which I have introduced in the last chapters. The perturbation schemes described in chapters 3 and 4 for $P^*$ can easily be extended to other important, yet uncertain and not well constrained parameters within a sea (or climate) model in order to assess the related uncertainty.

Aside from the thorough testing and discussion of the $P^*$ perturbations, I have started to apply and test spatially and temporally correlated parameter perturbations to other parameters of the sea ice model. Of major relevance for tuning a sea ice model are for example the sea ice albedo $\alpha_i$, the parameter $C$ in the exponential function of the ice strength calculations (see equation (3.7)), and the so called lead closing parameter $h_0$ in the formulation of the thermodynamic sea ice growth. The latter describes how fast open water areas are closing up under freezing conditions (see e.g. *Hibler*, 1979). By that it influences the ratio of lateral to vertical sea ice growth. In appendix D.1 some preliminary results of stochastic perturbations to these parameters are discussed.

Even though the stochastic parameter perturbations can basically be applied to any parameter, they need to be tuned and adjusted to the uncertainties they are supposed to sample. This involves adjustments to the spatial and temporal correlation schemes and the characteristics of the distribution functions of the random numbers used to perturb the parameter. Appendix D.2 gives some examples for alternative perturbation design.

Aside from the above mentioned parameters there are also the stress coefficients $c_{air}$ and $c_{ocean}$ in the atmospheric and oceanic stress terms $\vec{\boldsymbol{\tau}}_{air}$ and $\vec{\boldsymbol{\tau}}_{ocean}$ of equation (2.12) which may exhibit substantial uncertainties. They may vary considerably in time and space as a result of the sub-scale structure of the ice floes. Leads and ice ridging may enhance the influence of atmospheric and oceanic stresses, effects that are not or only partly accounted for in sea ice models.

Furthermore, the entire rheology parameterization itself is quite uncertain. Its capability of actually representing the observed behaviour of sea ice floes under convergent and shear motion is still debated and alternatives are being put forward (see e.g. *Girard et al.*, 2011). In this context, newly developed parameterization schemes might benefit from the introduction of stochastic aspects that are included right from the start (see, for example, the randomly chosen values of the cohesion for the elasto–brittle rheology of *Girard et al.* (2011)). On the other hand, including uncertainty estimates in sea ice and climate models at every level has to be implemented with caution. It is not desirable to account for a single uncertainty more than once. This might

lead to a large overestimation of uncertainty. Therefore, the accumulated effects of uncertainty estimates have to be considered, especially when these uncertainty estimates are included in the model on different levels, accounting both for sub-scale and resolved scale uncertainties.

In addition to the representation of model uncertainty, the uncertainty in the initial sea ice conditions needs to be sampled as well. As it is already common practice for simulations of the atmosphere to include uncertainty estimates for the initial conditions, this should and certainly will be adapted for sea ice and ocean modelling as well. The ultimate aim should be the incorporation of a complete set of uncertainty estimates in climate models. This is valid for all components of the model and includes stochastic parameterizations in the atmosphere, the ocean, the sea ice and the land surface model. In this context one should bear in mind that aside from the model uncertainty within each component there is also uncertainty related to the coupling between the components. Especially when the models of a coupled climate simulator apply very different discretization strategies and grids, the coupling between the models can cause inaccuracies. An example is ECHAM6-FESOM, for which the ocean resolution can be considerably higher than the resolution in the atmosphere (see figure 7.1). Appendix D.3 discusses a stochastic coupling scheme, in the development of which I am currently engaged. It aims at transferring some of the increased spatial variability of the higher resolved ocean model to the low resolution atmospheric model.

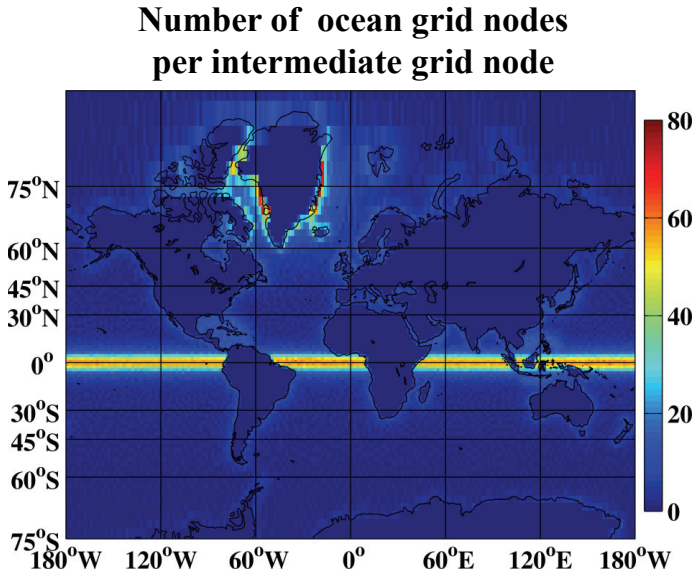


Figure 7.1: Illustration of the resolution difference between the FESOM grid and the intermediate grid used for the coupling to ECHAM6. The color coding indicates the number of FESOM grid nodes associated with the respective intermediate grid node.

# Danksagung

Die vorliegende Arbeit konnte ich nur mit der Unterstützung vieler Kollegen, Freunde und meiner Familie verfassen. Bei allen, die mir mit Rat und Tat zur Seite gestanden haben, möchte ich mich auf diesem Wege herzlich bedanken.

Ein besonderer Dank gilt Prof. Thomas Jung, der stets ein offenes Ohr für meine Fragen hatte und mich in jeder Weise unterstützt hat. Mein großer Dank geht an Prof. Peter Lemke, der mein Interesse an der Klimaforschung mit begründet und es mir ermöglicht hat, auf diesem Gebiet zu forschen. Ich danke darüber hinaus meinen Kollegen Dr. Sergey Danilov, Dr. Helge Gößling, Dr. Martin Losch, Dr. Dmitry Sidorenko, Dr. Ralph Timmermann und insbesondere Thomas Rackow für ihre Hilfsbereitschaft und die inspirierenden Gespräche. Für die stets kollegiale Zusammenarbeit möchte ich mich bei allen Mitarbeitern der Sektion Klimawissenschaften des Alfred-Wegener-Institutes herzlich bedanken.

Und nicht zuletzt danke ich meiner Familie, die mir in jeder Hinsicht den notwendigen Rückhalt gegeben hat.

# Glossary

| | |
|---|---|
| AMOC | Atlantic meridional overturning circulation |
| AWI | Alfred Wegener Institute,<br>Helmholtz Centre for Polar and Marine Research |
| CAA | Canadian Arctic Archipelago |
| CCSM4 | Community Climate System Model (version 4) |
| CICE | Community Ice Code model |
| CMIP5 | Coupled Model Intercomparison Project phase 5 |
| CORE (I and II) | Common Ocean Reference Experiment (atmospheric)<br>forcing (versions 1 and 2) |
| ECHAM6 | atmospheric climate model based on the<br>ECHMWF atmospheric model,<br>developed at the MPI Hamburg (version 6) |
| ECMWF | European Centre for Medium Range Weather Forecasts |
| ECMWF EPS | ECMWF Ensemble Prediction System |
| ERA-40 | ECMWF reanalysis (atmosphere and surface fields) |
| FESOM | Finite Element Sea ice-Ocean Model |
| GFDL CM3 | Geophysical Fluid Dynamics Laboratory Climate Model (version 3) |
| HadGEM2 | Hadley Centre Global Environment Model (version 2) |
| ICESat | Ice, Cloud, and Land Elevation Satellite |
| IPCC | Intergovernmental Panel on Climate Change |
| JSBACH | land surface model (part of ECHAM6) |
| MIROC-ESM | Model for Interdisciplinary Research On Climate Earth System Model |
| MPI (Hamburg) | Max Planck Institute (for Meteorology in Hamburg) (also MPI-M) |
| MPI-ESM-LR | MPI Earth System Model Low Resolution |
| MPI-OM | MPI (sea ice–) ocean model |
| MTP | Markov process time correlated perturbation |
| MTSP | Markov process time and space correlated perturbation |
| NSIDC | National Snow and Ice Data Center |
| NWP | numerical weather prediction |
| OASIS3-MCT | OASIS3 Model Coupling Toolkit (coupler ECHAM6 and FESOM) |
| PHC | Polar Science Center Hydrographic Climatology |
| PIOMAS | Pan-Arctic Ice Ocean Modeling and Assimilation System |
| RP | reassignment time step perturbation |
| SHEBA | Surface Heat Budget of the Arctic Ocean |
| SPPT | stochastically perturbed parameterization tendencies |
| SSBS | spectral stochastic kinetic energy backscatter scheme |
| ULS | upward looking sonar |

# List of relevant variables and parameters

| | |
|---|---|
| $a$ | lower boundary of transformed distribution function |
| $A$ | (fractional) sea ice concentration per $A_{grid}$ |
| $A_{grid}$ | reference area of a grid node [$m^2$] |
| $\alpha$ | autocorrelation coefficient of Markov process |
| $\alpha_i$ | sea ice albedo |
| $b$ | upper boundary of transformed distribution function |
| $\beta$ | tuning parameter of random number transformation |
| $C$ | dynamic ice strength parameter (of exponential function) |
| $d_{corr}$ | correlation distance [m] |
| $\Delta t$ | time step length [s] |
| $(\Delta t)_{pert}$ | reassignment time step [s] |
| $\dot{\epsilon}_{ij}$ | two-dimensional deformation rate tensor [$s^{-1}$] |
| $\eta_o$ | oceanic sea surface height [m] |
| $f$ | Coriolis parameter [$s^{-1}$] |
| $\vec{\mathbf{F}}_{int}$ | internal forces of sea ice (per area) [N $m^{-2}$] |
| $g$ | gravitational acceleration [9.81 m $s^{-2}$] |
| $h$ | (effective) sea ice thickness [m] (volume per $A_{grid}$) |
| $h_0$ | lead closing parameter [m] |
| $h_s$ | (effective) snow (on ice) thickness [m] (volume per $A_{grid}$) |
| $m$ | (sea ice) mass per area [kg $m^{-2}$] |
| $p$ | pressure p (ocean and atmosphere) [N $m^{-2}$] |
| $P$ | sea ice strength [N $m^{-1}$] |
| $P^*$ | dynamic ice strength parameter [N $m^{-2}$] |
| $P^*_{ref}$ | deterministic reference value of $P^*$ [N $m^{-2}$] |

| | |
|---|---|
| $\rho$ | (oceanic) density [kg m$^{-3}$] |
| $\rho_0$ | (oceanic) reference density [1000 kg m$^{-3}$] |
| $\rho_{ice}$ | sea ice density [kg m$^{-3}$] |
| $S$ | ocean salinity [g kg$^{-1}$] |
| $S_h$ | thermodynamic growth rate for $h$ [m s$^{-1}$] |
| $S_s$ | thermodynamic growth rate for $h_s$ [m s$^{-1}$] |
| $S_A$ | thermodynamic growth rate for $A$ [s$^{-1}$] |
| $\sigma$ | standard deviation (of Gaussian distribution) |
| $\sigma_{ij}$ | two-dimensional stress tensor [N m$^{-1}$] |
| $t$ | time [s] |
| $\tau$ | relaxation time [s] |
| $\vec{\boldsymbol{\tau}}_{air}$ | atmospheric stress (on ice) [N m$^{-2}$] |
| $\vec{\boldsymbol{\tau}}_{ocean}$ | oceanic stress (on ice) [N m$^{-2}$] |
| $\theta$ | oceanic potential temperature [K] |
| $\vec{\mathbf{u}}$ | ocean velocity vector [(m s$^{-1}$, m s$^{-1}$, m s$^{-1}$)] |
| $\vec{\mathbf{u}}_i$ | lateral sea ice velocity [(m s$^{-1}$, m s$^{-1}$)] |
| $u$ | zonal ocean velocity [m s$^{-1}$] |
| $u_i$ | zonal sea ice velocity [m s$^{-1}$] |
| $v$ | meridional ocean velocity [m s$^{-1}$] |
| $v_i$ | meridional sea ice velocity [m s$^{-1}$] |
| $w$ | vertical ocean velocity [m s$^{-1}$] |
| $x$ | zonal coordinate [m] |
| $x_{lon}$ | longitude [degrees or radians *East/West*] |
| $y$ | meridional coordinate [m] |
| $y_{lat}$ | latitude [degrees or radians *North/South*] |
| $z$ | vertical coordinate for ocean (in reference to mean sea level) [m] |

# List of Figures

# List of Tables

# Bibliography


Arnold, H. M., I. M. Moroz, and T. N. Palmer (2013), Stochastic parametrizations and model uncertainty in the Lorenz '96 system, *Phil. Trans. Roy. Soc. A*, *371(1991):20110479*, doi: 10.1098/rsta.2011.0479.

Bardsley, W. E. (2007), Note on $y$-truncation: A simple approach to generating bounded distributions for environmental applications, *Adv. Water Resour.*, *30*, 113–117, doi:10.1016/j.advwatres.2006.03.003.

Bekryaev, R. V., I. V. Polyakov, and V. A. Alexeev (2010), Role of polar amplification in long-term surface air temperature variations and modern arctic warming, *J. Climate*, *23*, 3888–3906, doi:10.1175/2010JCLI3297.1.

Berner, J., G. J. Shutts, M. Leutbecher, and T. N. Palmer (2009), A spectral stochastic kinetic energy backscatter scheme and its impact on flow-dependent predictability in the ECMWF Ensemble Prediction System, *J. Atmos. Sci.*, *66*, 603–626, doi:10.1175/2008JAS2677.1.

Berner, J., S.-Y. Ha, J. P. Hacker, A. Fournier, and C. Snyder (2011), Model uncertainty in a mesoscale ensemble prediction system: Stochastic versus multiphysics representations, *Mon. Wea. Rev.*, *139*, 1972–1995, doi:10.1175/2010MWR3595.1.

Blanchard-Wrigglesworth, E., C. M. Bitz, and M. M. Holland (2011), Influence of initial conditions and climate forcing on predicting Arctic sea ice, *Geophys. Res. Lett.*, *38*, L18,503, doi:10.1029/2011GL048807.

Brankart, J.-M. (2013), Impact of uncertainties in the horizontal density gradient upon low resolution global ocean modelling, *Ocean Model.*, *66*, 64–76, doi:10.1016/j.ocemod.2013.02.004.

Bright, D. R., and S. L. Mullen (2002), Short-range ensemble forecasts of precipitation during the Southwest Monsoon, *Weather Forecast.*, *17*, 1080–1100, doi:10.1175/1520-0434(2002)017⟨1080:SREFOP⟩2.0.CO;2.

Buizza, R., M. Miller, and T. N. Palmer (1999), Stochastic representation of model uncertainties in the ECMWF Ensemble Prediction System, *Q.J.R. Meteorol. Soc.*, *125*, 2887–2908, doi:10.1002/qj.49712556006.

Cavalieri, D., C. Parkinson, P. Gloersen, and H. J. Zwally (1996), Sea ice concentrations from Nimbus-7 SMMR and DMSP SSM/I passive microwave data (updated yearly), National Snow

and Ice Data Center, Boulder, CO, digital media, [Available online at `http://nsidc.org/data/docs/daac/nsidc0051_gsfc_seaice.gd.html`].

Chevallier, M., and D. Salas-Mélia (2012), The role of sea ice thickness distribution in the Arctic sea ice potential predictability: A diagnostic approach with a coupled GCM, *J. Climate*, *25*, 3025–3038, doi:10.1175/JCLI-D-11-00209.1.

Chevallier, M., D. Salas y Mélia, A. Voldoire, M. Déqué, and G. Garric (2014), Seasonal forecasts of the pan-Arctic sea ice extent using a GCM-based seasonal prediction system, *J. Climate*, *26*, 6092–6104, doi:10.1175/JCLI-D-12-00612.1.

Collins, a. N. B., W. J., M. Doutriaux-Boucher, N. Gedney, P. Halloran, T. Hinton, J. Hughes, C. D. Jones, M. Joshi, S. Liddicoat, G. Martin, F. O'Connor, J. Rae, C. Senior, S. Sitch, I. Totterdell, A. Wiltshire, and S. Woodward (2011), Development and evaluation of an Earth-system model - HadGEM2, *Model Dev. Discuss.*, *4*, 997–1062, doi:10.5194/gmdd-4-997-2011.

Danilov, S., G. Kivman, and J. Schröter (2004), A finite-element ocean model: Principles and evaluation, *Ocean Model.*, *6*, 125–150, doi:10.1016/S1463-5003(02)00063-X.

Dickson, R. R., J. Meincke, S.-A. Malmberg, and A. J. Lee (1988), The 'great salinity anomaly' in the Northern North Atlantic 1968–1982, *Geophys. Res. Lett.*, *20*, 103–151, doi:10.1016/0079-6611(88)90049-3.

Doblas-Reyes, F. J., A. Weisheimer, M. Déqué, N. Keenlyside, M. McVean, J. M. Murphy, P. Rogel, D. Smith, and T. N. Palmer (2009), Addressing model uncertainty in seasonal and annual dynamical ensemble forecasts, *Q.J.R. Meteorol. Soc.*, *135*, 1538–1559, doi:10.1002/qj464.

Fichefet, T., and M. A. M. Maqueda (1997), Sensitivity of a global sea ice model to the treatment of ice thermodynamics and dynamics, *J. Geophys. Res.*, *102*, 12,609–12,646, doi:10.1029/97JC00480.

Flato, G. M. (1998), The thickness variable in sea-ice models, *Atmos.-Ocean*, *36*, 29–36, doi:10.1080/07055900.1998.9649604.

Freeden, W., and M. Schreiner (2009), Spherical functions of mathematical geosciences, chap. 1., *Advances in Geophysical and Environmental Mechanics*, Springer-Verlag, Berlin and Heidelberg, Germany.

Gates, W. L., J. S. Boyle, C. Covey, C. G. Dease, C. M. Doutriaux, R. S. Drach, M. Fiorino, P. J. Gleckler, J. J. Hnilo, S. M. Marlais, T. J. Phillips, G. L. Potter, B. D. Santer, K. R. Sperber, K. E. Taylor, and D. N. Williams (1999), An overview of the results of the Atmospheric Model Intercomparison Project (AMIP I), *Bull. Amer. Meteor. Soc.*, *80*, 29–55, doi:10.1175/1520-0477(1999)080⟨0029:AOOTRO⟩2.0.CO;2.

Gent, P. R., G. Danabasoglu, L. J. Donner, M. M. Holland, E. C. Hunke, S. R. Jayne, D. M. Lawrence, R. B. Neale, P. J. Rasch, M. Vertenstein, P. H. Worley, Z.-L. Yang, and M. Zhang

(2011), The Community Climate System Model version 4, *J. Climate*, *24*, 4973–4991, doi: 10.1175/2011JCLI4083.1.

Giorgetta, M. A., E. Roecker, T. Mauritsen, J. Bader, T. Crueger, M. Esch, S. Rast, L. Kornblueh, H. Schmidt, S. Kinne, C. Hohenegger, B. Möbis, T. Krismer, K.-H. Wieners, and B. Stevens (2013), The atmospheric general circulation model ECHAM6 - model description, *Reports on Earth System Science*, *135*.

Girard, L., S. Bouillon, J. Weiss, D. Amitrano, T. Fichefet, and V. Legat (2011), A new modeling framework for sea-ice mechanics based on elasto-brittle rheology, *Ann. Glaciol.*, *52*, 123–132, doi:10.3189/172756411795931499.

Griffies, S. M., M. Winton, L. J. Donner, L. W. Horowitz, S. M. Downes, R. Farneti, A. Gnanadesikan, W. J. Hurlin, H.-C. Lee, Z. Liang, J. B. Palter, B. L. Samuels, A. T. Wittenberg, B. L. Wyman, J. Yin, and N. Zadeh (2011), The GFDL CM3 coupled climate model: Characteristics of the ocean and sea ice simulations, *J. Climate*, *24*, 3520–3544, doi:10.1175/2011JCLI3964.1.

Harder, M. (1996), Dynamics, roughness, and age of Arctic sea ice – Numerical investigations with a large-scale model, *Berichte zur Polarforschung*, *203*, pp. 127, Alfred Wegener Institute, Helmholtz Centre for Polar and Marine Research, Bremerhaven, Deutschland.

Harder, M., and H. Fischer (1999), Sea ice dynamics in the Weddell Sea simulated with an optimized model, *J. Geophys. Res.*, *104*, 11,151–11,162, doi:10.1029/1999JC900047.

Hawkins, E., and R. Sutton (2009), The potential to narrow uncertainty in regional climate predictions, *Bull. Amer. Meteor. Soc.*, *90*, 1095–1107, doi:10.1175/2009BAMS2607.1.

Hendricks, S., S. Gerland, L. H. Smedsrud, C. Haas, A. A. Pfaffhuber, and F. Nilsen (2011), Sea-ice thickness variability in Storfjorden, Svalbard, *Ann. Glaciol.*, *52*, 61–68, doi:10.3189/172756411795931561.

Hibler, W. D. (1979), A dynamic thermodynamic sea ice model, *J. Phys. Oceanogr.*, *9*, 815–846, doi:10.1175/1520-0485(1979)009⟨0815:ADTSIM⟩2.0.CO;2.

Holland, M. M., D. Bailey, and S. Vavrus (2011), Inherent sea ice predictability in the rapidly changing Arctic environment of the Community Climate System Model, version 3, *Clim. Dyn.*, *36*, 1239–1253, doi:10.1007/s00382-010-0792-4.

Holland, M. M., E. Blanchard-Wrigglesworth, J. Kay, and S. Vavrus (2013), Initial-value predictability of Antarctic sea ice in the Community Climate System Model 3, *Geophys. Res. Lett.*, *40*, 2121–2124, doi:10.1002/grl.50410.

Hunke, E. C., and J. K. Dukowicz (1997), An elastic–viscous–plastic model for sea ice dynamics, *J. Phys. Oceanogr.*, *27*, 1849–1867, doi:10.1175/1520-0485(1997)027⟨1849:AEVPMF⟩2.0.CO;2.

Hunke, E. C., and W. H. Lipscomb (2010), CICE: The Los Alamos Sea Ice Model: Documentation and software user's manual, version 4.1, *Tech. rep. LA-CC-06-012*, pp. 76, T-3 Fluid Dynamics Group, Los Alamos National Laboratory.

Hunkins, K. (1975), The oceanic boundary layer and stress beneath a drifting ice floe, *J. Geophys. Res.*, *80*, 3425–3433, doi:10.1029/JC080i024p03425.

IPCC AR5 WG1 (2013), Climate Change 2013: The Physical Science Basis. Contribution of Working Group I to the Fifth Assessment Report of the Intergovernmental Panel on Climate Change, *IPCC AR5 WG1*, pp. 1535, Cambridge University Press, Cambridge, United Kingdom, and New York, NY, USA.

IPCC SRES (2000), Special Report on Emissions Scenarios: A special report of Working Group II of the Intergovernmental Panel on Climate Change, *IPCC SRES*, pp. 570, Cambridge University Press, Cambridge, United Kingdom, and New York, NY, USA.

Jahn, A., and M. M. Holland (2013), Implications of Arctic sea ice changes for North Atlantic deep convection and the meridional overturning circulation in CCSM4-CMIP5 simulations, *Geophys. Res. Lett.*, *40*, 1206–1211, doi:10.1002/grl.50183.

Johnson, M., A. Proshutinsky, Y. Aksenov, A. T. Nguyen, R. Lindsay, C. Haas, J. Zhang, N. Diansky, R. Kwok, W. Maslowski, S. Häkkinen, I. Ashik, and B. de Cuevas (2012), Evaluation of Arctic sea ice thickness simulated by Arctic Ocean model intercomparison project models, *J. Geophys. Res.*, *117*, C00D13, doi:10.1029/2011JC007257.

Jung, T., T. N. Palmer, and G. J. Shutts (2005), Influence of a stochastic parameterization on the frequency of occurrence of North Pacific weather regimes in the ECMWF model, *Geophys. Res. Lett.*, *32*, L23,811, doi:10.1029/2005GL024248.

Juricke, S., and T. Jung (2014), Influence of stochastic sea ice parameterization on climate and the role of atmosphere-sea ice-ocean interaction, *Phil. Trans. R. Soc. A*, *372(2018):20130283*, doi:10.1098/rsta.2013.0283.

Juricke, S., P. Lemke, R. Timmermann, and T. Rackow (2013), Effects of stochastic ice strength perturbation on Arctic finite element sea ice modeling, *J. Climate*, *26*, 3785–3802, doi:10.1175/JCLI-D-12-00388.1.

Juricke, S., H. F. Goessling, and T. Jung (2014), Potential sea ice predictability and the role of stochastic sea ice perturbations, *Geophys. Res. Lett.*, to be resubmitted.

Kloeden, P. E., and E. Platen (1992), *Numerical Solution of Stochastic Differential Equations*, pp. 636, Springer-Verlag, Berlin, Germany.

Koenigk, T., and U. Mikolajewicz (2009), Seasonal to interannual climate predictability in mid and high northern latitudes in a global coupled model, *Clim. Dyn.*, *32*, 783–798, doi:10.1007/s00382-008-0419-1.

Kotecha, J. H., and P. M. Djurić (1999), Gibbs sampling approach for generation of truncated multivariate gaussian random variables, in *Proceedings ICASSP 1999*, *3*, 1757–1760, IEEE, Phoenix, AZ, USA.

Kuhlbrodt, T., A. Grisel, M. Montoya, A. Levermann, M. Hoffmann, and S. Rahmstorf (2007), On the driving processes of the Atlantic meridional overturning circulation, *Rev. Geophys.*, *45*, RG2001, doi:10.1029/2004RG000166.

Kwok, R., G. F. Cunningham, H. J. Zwally, and D. Yi (2007), Ice, Cloud, and Land Elevation Satellite (ICESat) over Arctic sea ice: Retrieval of freeboard, *J. Geophys. Res.*, *112*, C12,013, doi:10.1029/2006JC003978.

Kwok, R., G. F. Cunningham, M. Wensnahan, I. Rigor, H. J. Zwally, and D. Yi (2009), Thinning and volume loss of the Arctic Ocean sea ice cover: 2003–2008, *J. Geophys. Res.*, *114*, C07,005, doi:10.1029/2009JC005312.

Kwok, R., and D. A. Rothrock (2009), Decline in Arctic sea ice thickness from submarine and ICESat records: 1958–2008, *Geophys. Res. Lett.*, *36*, L15,501, doi:10.1029/2009GL039035.

Large, W. G., and S. G. Yeager (2009), The global climatology of an interannually varying air-sea flux data set, *Clim. Dyn.*, *33*, 341–364, doi:10.1007/s00382-008-0441-3.

Latif, M., T. Martin, and W. Park (2013), Southern ocean sector centennial climate variability and recent decadal trends, *J. Climate*, *26*, 7767–7782, doi:10.1175/JCLI-D-12-00281.1.

Laxon, S., N. Peacock, and D. Smith (2003), High interannual variability of sea ice thickness in the Arctic region, *Nature*, *425*, 947–950, doi:10.1038/nature02050.

Lefebvre, M. (2007), *Applied stochastic processes*, Springer Science+Business Media LLC, New York, USA.

Lemieux, J. F., D. Knoll, B. Tremblay, D. M. Holland, and M. Losch (2012), A comparison of the Jacobian-free Newton–Krylov method and the EVP model for solving the sea ice momentum equation with a viscous-plastic formulation: a serial algorithm study, *J. Comput. Phys.*, *231*, 5926–5944, doi:10.1016/j.jcp.2012.05.024.

Lemke, P., E. W. Trinkl, and K. Hasselmann (1980), Stochastic dynamic analysis of polar sea ice variability, *J. Phys. Oceanogr.*, *10*, 2100–2120, doi:10.1175/1520-0485(1980)010⟨2100:SDAOPS⟩2.0.CO;2.

Li, X., M. Charron, L. Spacek, and C. Guillem (2008), A regional ensemble prediction system based on moist targeted singular vectors and stochastic parameter perturbations, *Mon. Weather Rev.*, *136*, 443–462, doi:10.1175/2007MWR2109.1.

Lin, J. W.-B., and J. D. Neelin (2000), Influence of a stochastic moist convective parameterization on tropical climate variability, *Geophys. Res. Lett.*, *27*, 3691–3694, doi:10.1029/2000GL011964.

Lin, J. W.-B., and J. D. Neelin (2002), Considerations for stochastic convective parameterization, *J. Atmos. Sci.*, *59*, 959–975, doi:10.1175/1520-0469(2002)059⟨0959:CFSCP⟩2.0.CO;2.

Lorenz, E. N. (1963), Deterministic nonperiodic flow, *J. Atmos. Sci.*, *20*, 130–141, doi:10.1175/1520-0469(1963)020⟨0130:DNF⟩2.0.CO;2.

Lorenz, E. N. (1996), Predictability: a problem partly solved, in *Proc. Semin. Predictability*, vol. 1, pp. 1–19, ECMWF, Reading, United Kingdom.

Losch, M., A. Fuchs, J. F. Lemieux, and A. Vanselow (2013), A parallel jacobian-free newton–krylov solver for a coupled sea ice-ocean model, *J. Comput. Phys.*, *257*, 901–911, doi:10.1016/j.jcp.2013.09.026.

Lott, F., L. Guez, and P. Maury (2012), A stochastic parameterization of non-orographic gravity waves: Formalism and impact on the equatorial stratosphere, *Geophys. Res. Lett.*, *39*, L06,807, doi:10.1029/2012GL051001.

Magnusson, L., J. Nycander, and E. Källén (2009), Flow-dependent versus flow-independent initial perturbations for ensemble prediction, *Tellus A*, *61*, 194–209, doi:10.1111/j.1600-0870.2008.00385.x.

Mahajan, S., R. Zhang, and T. L. Delworth (2011), Impact of the Atlantic meridional overturning circulation (AMOC) on Arctic surface air temperature and sea ice variability, *J. Clim.*, *24*, 6573–6581, doi:10.1175/2011JCL14002.1.

Melling, H., and D. A. Riedel (2008), Ice draft and ice velocity data in the Beaufort Sea, 1990–2003, National Snow and Ice Data Center, Boulder, CO, digital media, [Available online at `http://nsidc.org/data/g02177.html`].

Owens, W. B., and P. Lemke (1990), Sensitivity studies with a sea ice–mixed layer–pycnocline model in the Weddell Sea, *J. Geophys. Res.*, *95*, 9527–9538, doi:10.1029/JC095iC06p09527.

Palmer, T. N. (2012), Towards the probabilistic earth-system simulator: A vision for the future of climate and weather prediction, *Q.J.R. Meteorol. Soc.*, *138*, 841–861, doi:10.1002/qj.1923.

Pithan, F., and T. Mauritsen (2014), Arctic amplification dominated by temperature feedbacks in contemporary climate models, *Nat. Geosci.*, *7*, 181–184, doi:10.1038/ngeo2071.

Plant, R. S., and G. C. Craig (2008), A stochastic parameterization for deep convection based on equilibrium statistics, *J. Atmos. Sci.*, *65*, 87–105, doi:10.1175/2007JAS2263.1.

Pohlmann, H., M. Botzet, M. Latif, A. Roesch, M. Wild, and P. Tschuk (2004), Estimating the decadal predictability of a coupled AOGCM, *J. Climate*, *17*, 4463–4472, doi:10.1175/3209.1.

Rackow, T., H. F. Goessling, T. Jung, D. Sidorenko, T. Semmler, and D. Handorf (2014), Towards multi-resolution global climate modeling with ECHAM6-FESOM. Part II: Climate variability, in preparation.

Rahmstorf, S. (2002), Ocean circulation and climate during the past 120,000 years, *Nature*, *419*, 207–214, doi:10.1038/nature01090.

Rahmstorf, S. (2006), Thermohaline ocean circulation, in *Encyclopedia of Quaternary Sciences*, edited by S. A. Elias, Elsevier, Amsterdam, Netherlands.

Semmler, T., R. McGrath, and S. Wang (2012), The impact of Arctic sea ice on the Arctic energy budget and on the climate of the Northern mid-latitudes, *Clim. Dyn.*, *39*, 2675–2694, doi:10.1007/s00382-012-1353-9.

Shepard, D. (1968), A two-dimensional interpolation function for irregularly-spaced data, in *Proceedings of the 1968 23rd ACM national conference*, pp. 517–524, ACM, New York, NY, USA.

Shutts, G. J. (2005), A kinetic energy backscatter algorithm for use in ensemble prediction systems, *Q.J.R. Meteorol. Soc.*, *131*, 3079–3102, doi:10.1256/qj.04.106.

Sidorenko, D., Q. Wang, S. Danilov, and J. Schröter (2011), FESOM under coordinated ocean-ice reference experiment forcing, *Ocean Dynam.*, *61*, 881–890, doi:10.1007/s10236-011-0406-7.

Sidorenko, D., T. Rackow, T. Jung, T. Semmler, D. Barbi, S. Danilov, K. Dethloff, W. Dorn, H. F. Goessling, D. Handorf, S. Harig, W. Hiller, S. Juricke, M. Losch, J. Schröter, Q. Wang, and K. Fieg (2014), Towards multi-resolution global climate modeling with ECHAM6-FESOM. Part I: Model formulation and mean climate, under review.

Sigmond, M., J. Fyfe, G. M. Flato, V. V. Kharin, and W. J. Merryfield (2013), Seasonal forecast skill of Arctic sea ice area in a dynamical forecast system, *Geophys. Res. Lett.*, *40*, 529–534, doi:10.1002/grl.50129.

Steele, M., R. Morley, and W. Ermold (2001), PHC: A global ocean hydrography with a high-quality arctic ocean, *J. Climate*, *14*, 2079–2087, doi:10.1175/1520-0442(2001)014⟨2079:PAGOHW⟩2.0.CO;2.

Stevens, B., M. Giorgetta, M. Esch, T. Mauritsen, T. Crueger, S. Rast, M. Salzmann, H. Schmidt, J. Bader, K. Block, R. Brokopf, I. Fast, S. Kinne, L. Kornblueh, U. Lohmann, R. Pincus, T. Reichler, and E. Roeckner (2013), Atmospheric component of the MPI-M Earth System Model: ECHAM6, *J. Adv. Model. Earth Syst.*, *5*, 146–172, doi:10.1002/jame.20015.

Stössel, A., P. Lemke, and W. B. Owens (1990), Coupled sea ice–mixed layer simulations for the Southern Ocean, *J. Geophys. Res.*, *95*, 9539–9555, doi:10.1029/JC095iC06p09539.

Stroeve, J. C., V. Kattsov, A. Barrett, M. Serreze, T. Pavlova, M. M. Holland, and W. N. Meier (2012), Trends in Arctic sea ice extent from CMIP5, CMIP3 and observations, *Geophys. Res. Lett.*, *39*, L16,502, doi:10.1029/2012GL052676.

Taylor, K. E., R. J. Stouffer, and G. A. Meehl (2012), An overview of CMIP5 and the experiment design, *Bull. Amer. Meteor. Soc.*, *93*, 485–498, doi:10.1175/BAMS-D-11-00094.1.

Tietsche, S., J. J. Day, V. Guemas, W. J. Hurlin, S. P. E. Keeley, D. Matei, R. Msadek, M. Collins, and E. Hawkins (2014), Seasonal to interannual arctic sea ice predictability in current global climate models, *Geophys. Res. Lett.*, *41*, doi:10.1002/2013GL058755.

Timmermann, R., S. Danilov, J. Schröter, C. Böning, D. Sidorenko, and K. Rollenhagen (2009), Ocean circulation and sea ice distribution in a finite element global sea ice-ocean model, *Ocean Model.*, *27*, 114–129, doi:10.1016/j.ocemod.2008.10.009.

Tremblay, L.-B., and M. Hakakian (2006), Estimating the sea ice compressive strength from satellite-derived sea ice drift and NCEP reanalysis data, *J. Phys. Oceanogr.*, *36*, 2165–2172, doi:10.1175/JPO2954.1.

Turner, J., J. E. Overland, and J. E. Walsh (2007), An arctic and antarctic perspective on recent climate change, *Int. J. Climatol.*, *27*, 277–293, doi:10.1002/joc.1406.

Turner, J., T. J. Bracegirdle, T. Phillips, G. J. Marshall, and J. S. Hosking (2013), An initial assessment of Antarctic sea ice extent in the CMIP5 models, *J. Clim.*, *26*, 1473–1484, doi:10.1175/JCLID-12-00068.1.

Uppala, S. M., P. W. KÅllberg, A. J. Simmons, U. Andrae, V. D. C. Bechtold, M. Fiorino, J. K. Gibson, J. Haseler, A. Hernandez, G. A. Kelly, X. Li, K. Onogi, S. Saarinen, N. Sokka, R. P. Allan, E. Andersson, K. Arpe, M. A. Balmaseda, A. C. M. Beljaars, L. V. D. Berg, J. Bidlot, N. Bormann, S. Caires, F. Chevallier, A. Dethof, M. Dragosavac, M. Fisher, M. Fuentes, S. Hagemann, E. Holm, B. J. Hoskins, L. Isaksen, P. A. E. M. Janssen, R. Jenne, A. P. Mcnally, J.-F. Mahfouf, J.-J. Morcrette, N. A. Rayner, R. W. Saunders, P. Simon, A. Sterl, K. E. Trenberth, A. Untch, D. Vasiljevic, P. Viterbo, and J. Woollen (2005), The ERA-40 re-analysis, *Q.J.R. Meteorol. Soc.*, *131*, 2961–3012, doi:10.1256/qj.04.176.

Valcke, B. (2013), The OASIS3 coupler: A European climate modelling community software, *Geosci. Model Dev.*, *6*, 373–388, doi:10.5194/gmdd-5-2139-2012.

Vitart, F. (2014), Evolution of ECMWF sub-seasonal forecast skill scores, *Q.J.R. Meteorol. Soc.*, doi:10.1002/qj.2256.

Wang, Q., S. Danilov, and J. Schröter (2008), Finite element ocean circulation model based on triangular prismatic elements, with application in studying the effect of topography representation, *J. of Geophys. Res.*, *113*, C05,015, doi:10.1029/2007JC004482.

Wang, Q., S. Danilov, D. Sidorenko, R. Timmermann, C. Wekerle, X. Wang, T. Jung, and J. Schröter (2013), The Finite Element Sea ice-Ocean Model (FESOM): Formulation of an unstructured-mesh ocean general circulation model, *Geosci. Model Dev. Discuss.*, *6*, 3893–3976, doi:10.5194/gmdd-6-3893-2013.

Watanabe, S., T. Hajima, K. Sudo, T. Nagashima, T. Takemura, H. Okajima, T. Nozawa, H. Kawase, M. Abe, T. Yokohata, T. Ise, H. Sato, E. Kato, K. Takata, S. Emori, and M. Kawamiya (2011), MIROC-ESM 2010: model description and basic results of CMIP5-20c3m experiments, *Geosci. Model Dev.*, *4*, 845–872, doi:10.5194/gmd-4-845-2011.

Weisheimer, A., T. N. Palmer, and F. J. Doblas-Reyes (2011), Assessment of representations of model uncertainty in monthly and seasonal forecast ensembles, *Geophys. Res. Lett.*, *38*, L16,703, doi:10.1029/2011GL048123.

Weiss, J. (2013), Drift, deformation, and fracture of sea ice, chap. 5, *SpringerBriefs in Earth Sciences*, Springer Netherlands, Dordrecht Netherlands, doi:10.1007/978-94-007-6202-2_5.

Wettlaufer, J. S. (1991), Heat flux at the ice-ocean interface, *J. Geophys. Res.*, *96*, 7215–7236, doi:10.1029/90JC00081.

Wilks, D. S. (2005), Effects of stochastic parametrizations in the Lorenz '96 system, *Q.J.R. Meteorol. Soc.*, *131*, 389–407, doi:10.1256/qj.04.03.

Wilks, D. S. (2011), *Statistical methods in the atmospheric sciences*, International Geophysics Series, 3rd edn ed., Academic Press, Waltham, MA.

Williams, P. D. (2012), Climatic impacts of stochastic fluctuations in air-sea fluxes, *Geophys. Res. Lett.*, *39*, L10,705, doi:10.1029/2012GL051813.

Witte, H., and E. Fahrbach (2005), AWI moored ULS data, Greenland Sea and Fram Strait, 1991–2002, National Snow and Ice Data Center, Boulder, CO, digital media, [Available online at `http://nsidc.org/data/g02139.html`].

WOR (2010), *World Ocean Review 1*, chap. 1, edited by T. Schröder, maribus gGmbH, Hamburg, Germany.

Yu, Y., G. A. Maykut, and D. A. Rothrock (2004), Changes in the thickness distribution of Arctic sea ice between 1958–1970 and 1993–1997, *J. Geophys. Res.*, *109*, C08,004, doi:10.1029/2003JC001982.

Zhang, J., and D. A. Rothrock (2003), Modeling global sea ice with a thickness and enthalpy distribution model in generalized curvilinear coordinates, *Mon. Wea. Rev.*, *131*, 845–861, doi:10.1175/1520-0493(2003)131⟨0845:MGSIWA⟩2.0.CO;2.

# Appendix A

# Bounded distributions

For this study bounded distribution functions for the random numbers of the perturbations are needed. In figure A.1 the corresponding distribution functions of the so-called $x$- and $y$-truncated Gaussian distributions (*Bardsley*, 2007) can be seen, with a fixed variance $\sigma^2$ and zero mean of the initial Gaussian distribution. An additional bounded, Gaussian-like random number can be generated by the transformation

$$x(i,j) = -a + (2a)/(1 + e^{-\beta y(i,j)}), \tag{A.1}$$

where $y(i,j)$ is a random number from a Gaussian distribution, again with variance $\sigma^2$ and zero mean, and $a$ is the bounding parameter. In this transformation $\beta$ is some fixed value that meets the inequality $0 < \beta < \sqrt{2}/\sigma_{lim}$, with $\beta = 1.4/\sigma_{lim}$ used here. The value $\beta$ is necessary to keep the maximum of the transformed distribution function at 0. $\sigma_{lim}$ is a value greater or equal to the standard deviation $\sigma$ of the Gaussian distribution that is going to be transformed.

The distribution function after the transformation of a Gaussian distributed random number $y(i,j)$ is also shown in figure A.1.

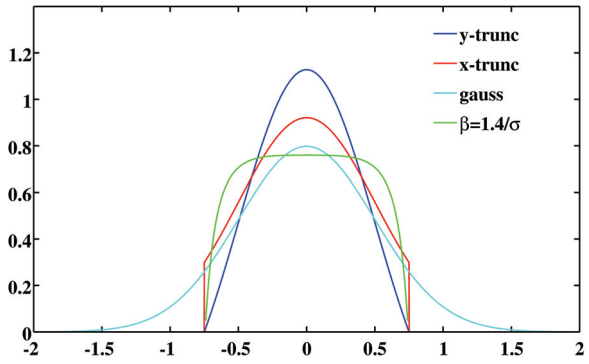


Figure A.1: The Gaussian distribution function (cyan), the corresponding $x$-truncated and $y$-truncated Gaussian distribution functions (red and blue, respectively), and the distribution function of a random variable after the transformation (A.1) with $\beta = 1.4/\sigma$ is applied to the Gaussian distributed random variable (green). The standard deviation is $\sigma = 0.5$ for the Gaussian distribution, the mean is 0 and the bounding parameter is $a = 0.75$ for the three truncated distributions.

# Appendix B

# Derivation of the Markov process time correlated perturbation

Equation (3.9) in section 3.3.2 can be derived by discretizing a stochastic differential equation of the form

$$dy_t = -\lambda y_t dt + \sigma_W dW_t \text{ (in Itô formulation)}, \tag{B.1}$$

using the Euler–Maruyama scheme (*Kloeden and Platen*, 1992), with $(W_t)_{t\geq 0}$ a Wiener process and $\sigma_W^2 = \sigma^2/(\Delta t)_{pert}$.

Under these conditions the discretization of equation (B.1) yields

$$\alpha = 1 - \lambda(\Delta t), \tag{B.2}$$

with $\lambda = 1/\tau$ and $\tau$ the relaxation time, as already mentioned in section 3.3.2. The mean of a random variable $\mathbf{y}$ at node $i$ described by equation (3.9) is zero for all time steps $j$, while the variance is given by

$$Var(\mathbf{y}(i,j)) = \frac{\sigma^2 \Delta t}{(\Delta t)_{pert}} \frac{(\alpha^2)^{(j-j')} - 1}{\alpha^2 - 1} = \tilde{\sigma}^2 \frac{(\alpha^2)^{(j-j')} - 1}{\alpha^2 - 1} \tag{B.3}$$

and depends on the amount of time steps the node has been covered by ice since it was last ice-free, $(j - j')$, with $j$ being the current time step and $j'$ the time step when the node was last ice-free. The resulting random variable is Gaussian distributed because all the summands are Gaussian distributed.

For $(j - j') \to \infty$ the variance is limited by

$$\frac{\sigma^2 \Delta t}{(\Delta t)_{pert}(1 - \alpha^2)} = \frac{\tilde{\sigma}^2}{(1 - \alpha^2)}. \tag{B.4}$$

For the transformation of the random number $y(i,j)$ into the bounded $x(i,j)$ used in equation (3.9) the simple equation (A.1) can be used, or corresponding transformations for the cases of $x$- and $y$-truncated Gaussian distributions. *Kotecha and Djurić* (1999) gave such a transformation for the $x$-truncated Gaussian distribution. In case of the more complicated $y$-truncated Gaus-

sian distribution the corresponding transformation needs to be implemented via, for instance, Newton's method. For both transformations the variance at the current time step is needed. For the simple transformation via equation (A.1) the value $\sigma_{lim}$ is set to the limiting variance in equation (B.4) for all time steps.

# Appendix C

# Supporting material for chapter 5

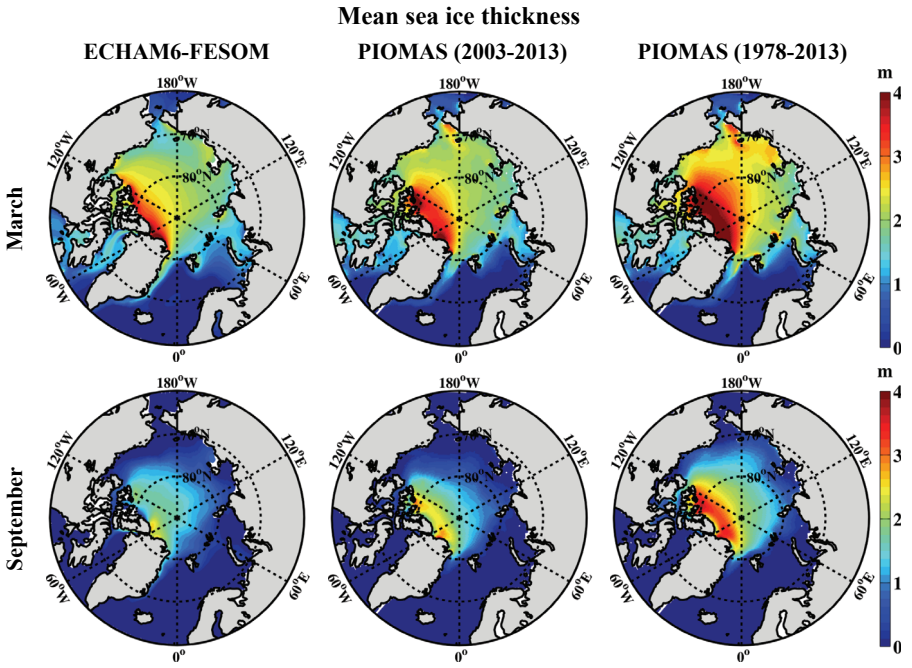


Figure C.1: Mean Arctic sea ice thickness distribution (m) for (top) March and (bottom) September: (left) simulated by ECHAM6-FESOM (averaged over 150 years of a climate simulation) and from the Pan-Arctic Ice Ocean Modeling and Assimilation System (PIOMAS) reanalysis (from the Polar Science Center at `http://psc.apl.washingto.edu`; *Zhang and Rothrock*, 2003) for (middle) 2003–2013 and (right) 1978–2013.

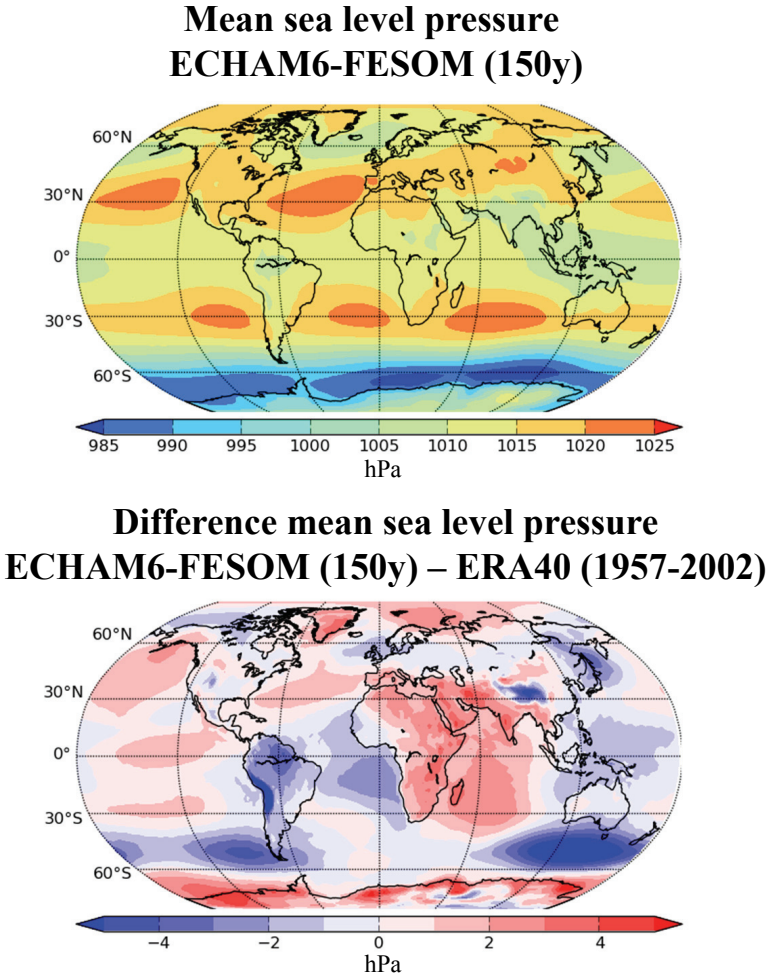


Figure C.2: Top: Annual mean sea level pressure (hPa) simulated by ECHAM6-FESOM (averaged over 150 years of a climate simulation). Bottom: Difference in annual mean sea level pressure (hPa) between ECHAM6-FESOM (150 year average) and ERA40 reanalysis (1957–2002 average; *Uppala et al.*, 2005).

# Appendix D

# Other stochastic perturbation schemes

## D.1. Perturbations of alternative parameters

All the preliminary tests with perturbations of the parameters discussed below have been conducted for uncoupled FESOM simulations with CORE version 2 atmospheric forcing (*Large and Yeager*, 2009).

### D.1.1. $C$ and $h_0$ perturbations

While $P^*$ impacts linearly on the internal ice strength, $C$ enters into the exponential function relating sea ice concentration to the ice strength. With increasing sea ice concentrations, the exponential term in equation (3.7) increases. It reaches its maximum of 1 at an ice concentration of $A = 1$ (i.e. 100% coverage). The term stays close to 0 for low to medium sea ice concentration and rises quickly at concentrations of above 0.8 to 0.9 (see figure D.1). The parameter $C$ impacts the range of sea ice concentration values for which internal forces play a considerable role in the simulation of the sea ice dynamics. For larger values of $C$ higher ice concentrations are necessary for sea ice to resist deformation. In contrast to $P^*$, variations of the parameter $C$ do not impact the maximum value of the internal ice strength for a given sea ice thickness. For low ice concentrations the value of $C$ is generally of little importance and so is the whole internal stress term of equation (2.12).

The lead closing parameter $h_0$ is an important parameter in the formulation of the thermodynamic sea ice growth. It determines the rate at which open water areas (leads, i.e. $(1 - A)$) are covered by sea ice under freezing conditions. Under freezing conditions the right-hand side $S_A$ of equation (2.11) includes the term

$$\frac{1 - A}{h_0} \left( \frac{\partial h}{\partial t} \right)_{o,freezing}, \tag{D.1}$$

where $\left( \frac{\partial h}{\partial t} \right)_{o,freezing}$ is the thermodynamic growth rate of sea ice over open water. $h_0$ is also

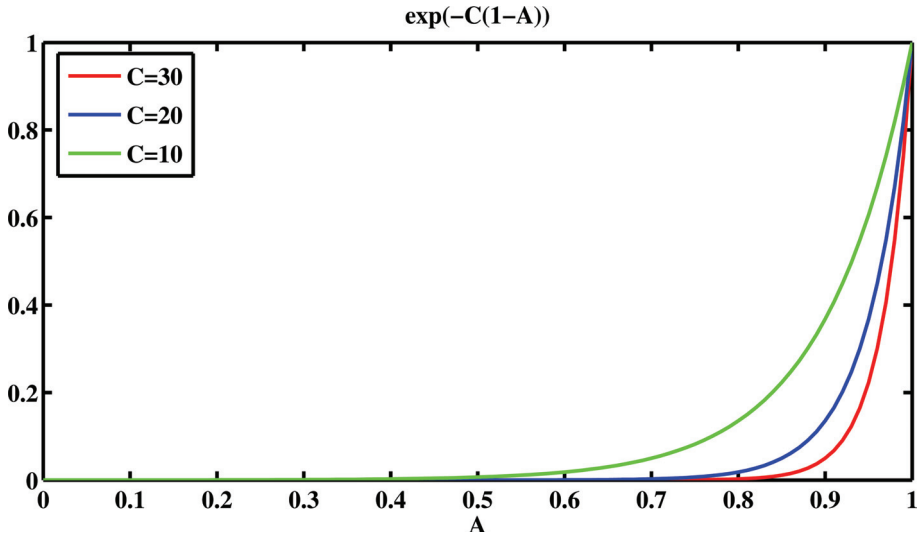


Figure D.1: The term $e^{(-C(1-A))}$ of the internal ice strength parameterization (see equation (3.7)) as a function of sea ice concentration A, for different values of the parameter $C$, i.e. for $C = 10$ (green), the FESOM default value $C = 20$ (blue), and $C = 30$ (red).

called the demarcation thickness, as it discriminates between the thick ice $h$ and the thin ice that is generated in leads and on open water (see *Hibler*, 1979). Small values of $h_0$ increase the rate with which leads are closing, while large values decelerate lead closing. As a consequence, the actual ice thickness $h/A$ is affected in the opposite way. An increase of $A$ leads to a decrease of $h/A$ if $h$ is not increased by the same factor.

To get an idea of the uncertainty related to the choice of both parameters, I have conducted single 3-year simulations applying the stochastic parameter perturbation introduced in chapter 3 separately to $C$ and $h_0$ (keeping the other values fixed). The setting of the parameter perturbations is the same as for experiment MTSP0 of chapter 3 (see table 3.1). This means that the perturbation scheme has not been tuned separately for the different parameters. The only (minor) difference to the scheme described in section 3.3.3 concerns perturbations of $h_0$. In this case, perturbed values are not averaged over the three nodes of an element (see chapter 3), as thermodynamic calculations take place on the nodes themselves. The three perturbed simulations ($P^*$, $C$, and $h_0$) are compared to a deterministic simulation with fixed default values $P^* = 20000\,\mathrm{N\ m^{-2}}$, $C = 20$, and $h_0 = 0.5\,\mathrm{m}$.

Figures D.2 to D.5 show the impact of the parameter perturbations for $P^*$, $C$, and $h_0$ when compared to the unperturbed reference simulation. Shown is the seasonally averaged difference of one single stochastic realization to the reference simulation, for both thickness $h$ and concentration $A$, and the northern as well as southern hemisphere. Differences have been calculated for the third year after the stochastic perturbations have been switched on. The simulation with $P^*$ perturbations (left columns) is the simulation MTSP0 of chapter 3 (compare figures D.2 and D.3, third panel, left, with figure 3.4, right column; note the different contour intervals).

Figure D.2 (left column) confirms the large impact of the $P^*$ perturbations on Arctic sea ice thickness. Affected areas show a large deviation from the reference simulation and are also

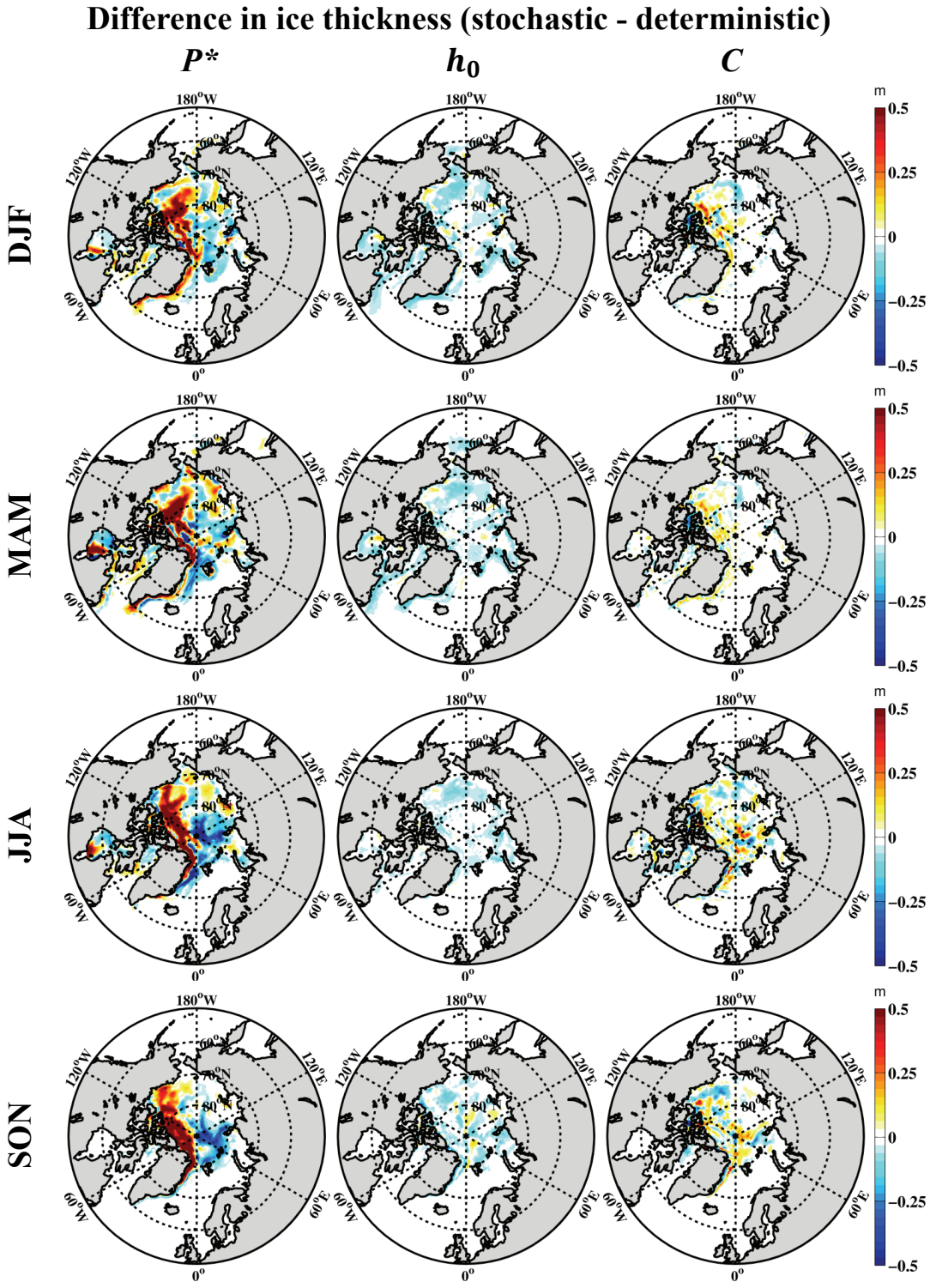


Figure D.2: Difference in northern hemisphere sea ice thickness (m) between simulations with (left column) $P^*$ perturbations, (middle) $h_0$ perturbations, (right) $C$ perturbations, and a deterministic reference simulation without parameter perturbations. Simulations have been carried out with FESOM, applying CORE version 2 atmospheric forcing (*Large and Yeager*, 2009). Shown are the mean differences for the four seasons (top to bottom) DJF, MAM, JJA and SNO of the third year after initialization.

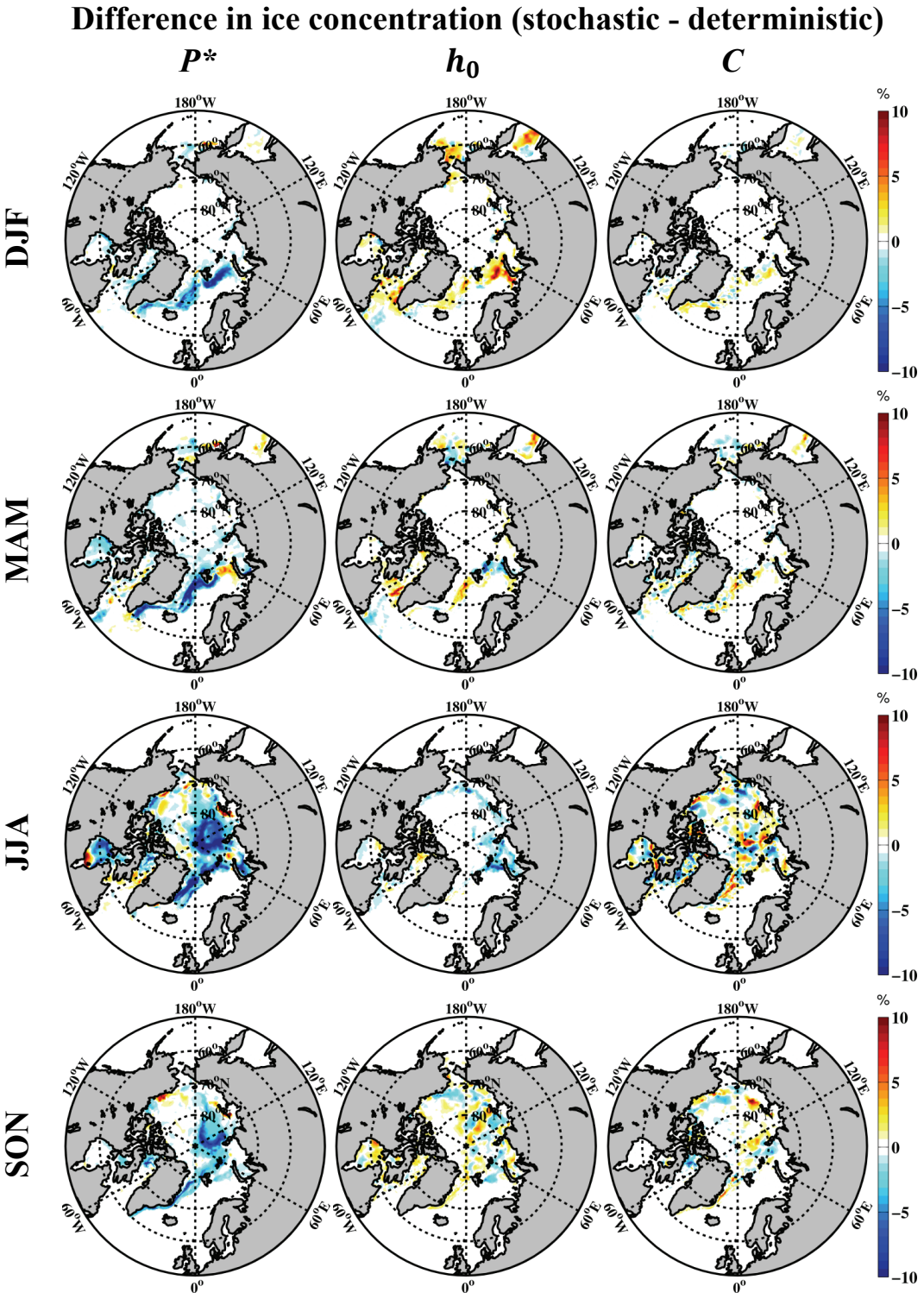


Figure D.3: As in figure D.2, but for sea ice concentration.

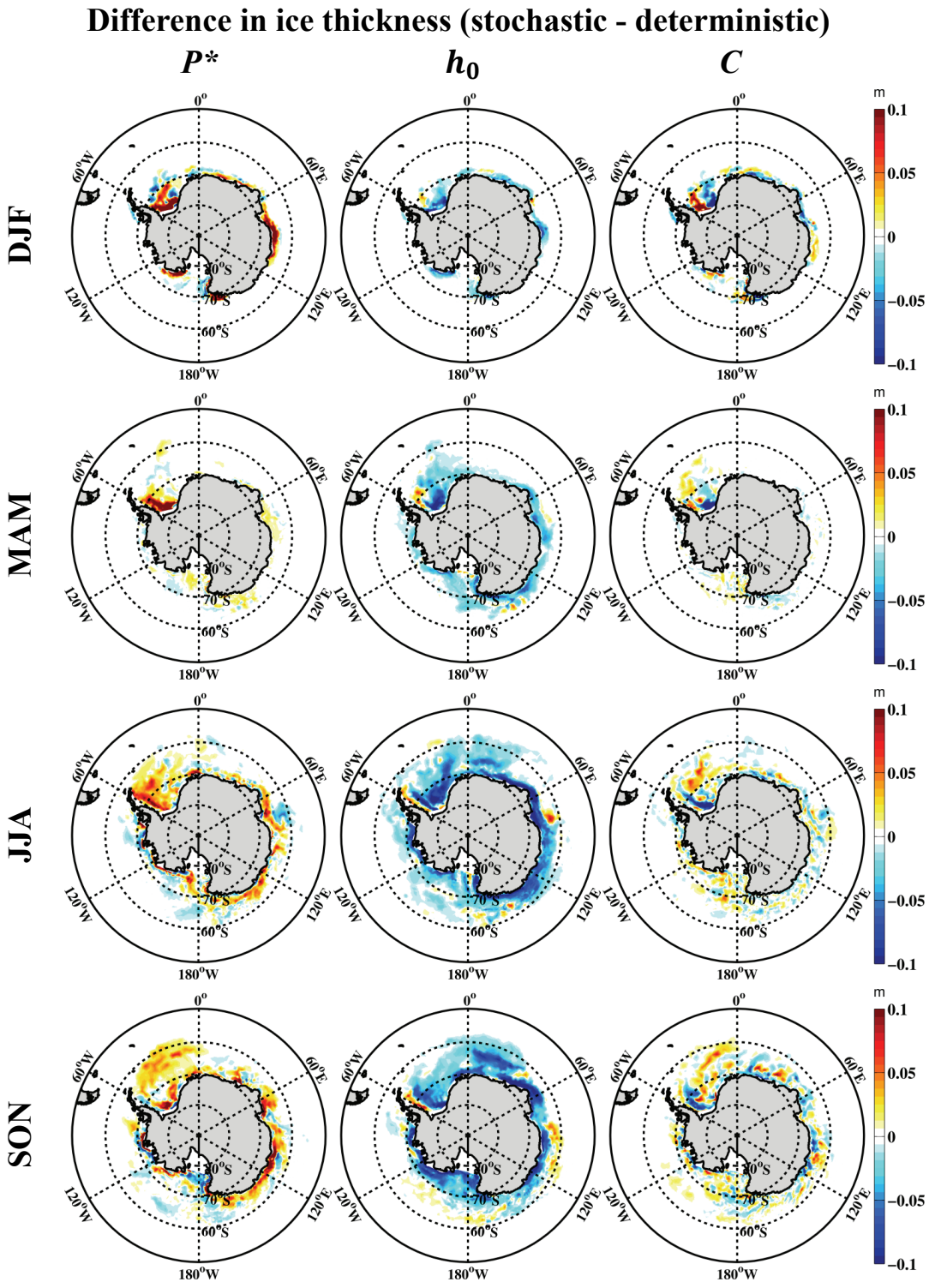


Figure D.4: As in figure D.2, but for the southern hemisphere. Note the differing contour intervals.

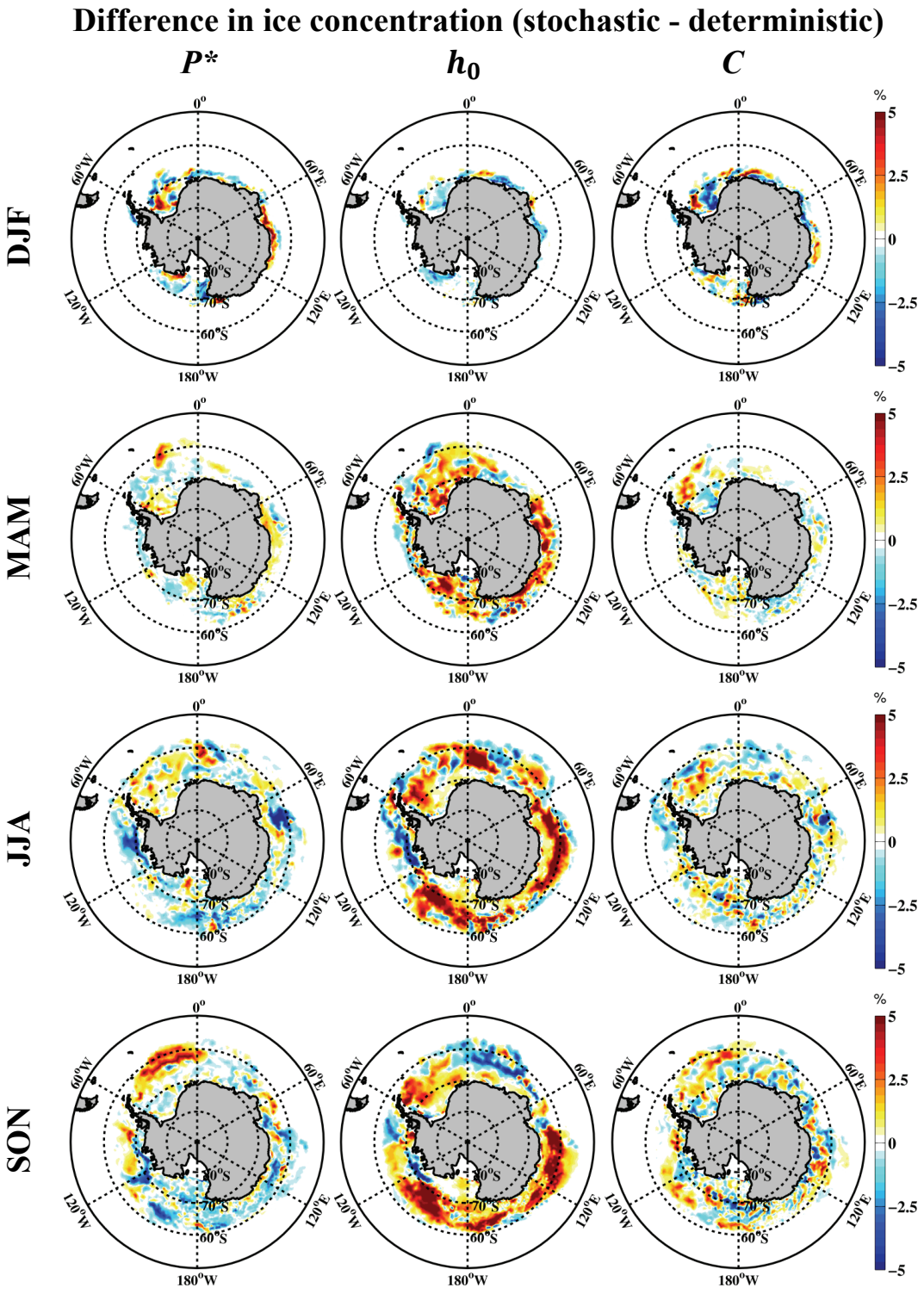


Figure D.5: As in figure D.3, but for the southern hemisphere. Note the differing contour intervals.

of considerable spatial scale. Sea ice concentration (figure D.3, left column) is less affected and changes are localized near the ice edge, especially during winter, when concentrations in the central Arctic are high.

Changes in $h$ and $A$ due to perturbations of $C$ (figures D.2 and D.3, right columns) are generally not very large and are of rather small scale. While differences are confined to similar regions as those caused by $P^*$ perturbations, the sign of these changes seems more or less random. This suggests that the $C$ perturbations are not leading to significant shifts in the mean sea ice distribution. It is also an indication for presumably smaller ensemble spread when compared to the large changes caused by the $P^*$ perturbations.

Differences caused by $h_0$ on the other hand show a clear preference towards reduced sea ice thickness in most areas (D.2, middle column) and a rather contrary behaviour for sea ice concentration (figure D.3, middle column), at least during winter and autumn. Although the amplitude of the changes is also rather small, spatial scales are large. For sea ice thickness most of the Arctic sea ice is affected, while changes in sea ice concentration are again confined to the ice edge.

Looking at the impacts of the perturbations on southern hemisphere sea ice (figures D.4 and D.5), these preliminary results present quite substantial differences when compared to the response of Arctic sea ice. The first thing to notice is the reduced amplitude of the changes. As has been discussed before, it is caused by the comparatively thin Antarctic sea ice and the large reduction of sea ice area during austral summer months.

Changes due to $C$ perturbations (right columns) are again rather small, localized and seem more or less randomly distributed.

The differences caused by $P^*$ perturbations (left columns) are still quite large scale, at least for sea ice thickness. They are mainly located near coastal areas and in the Weddell Sea.

$h_0$ perturbations (middle columns), however, produce very large scale impacts in the southern hemisphere, leading generally to an increase in sea ice concentration and a decrease in (effective) sea ice thickness. This is consistent with the fact that $h_0$ determines the ratio between lateral and vertical sea ice growth, which leads to contrary behaviour for sea ice concentration and thickness. However, whether or not these differences are significant and lead to a shift in the mean distribution cannot be answered by a single simulation. But if they do not lead to a shift in the mean, these first results consequently suggest that comparatively large ensemble spread can be expected for $h_0$ perturbations. Further simulations will have to be carried out in the future to clarify this.

Nevertheless, the single simulations presented here reveal the differing magnitude of uncertainties related to different sea ice parameters. In addition, this preliminary evaluation illustrates that uncertainty estimation might lead to quite different conclusions for southern and northern hemisphere sea ice, due to the different feedbacks and physical processes involved.

### D.1.2. Sea ice albedo perturbations

The sea ice albedo parameterization applied by FESOM is rather simple. It discriminates between snow-covered and snow-free sea ice, as well as between melting and dry snow or ice

conditions, respectively, given a predefined melting temperature threshold ($T_m = 0°C$). The ice albedo $\alpha_i$ can take on one of the following values, given the respective conditions:

- ice albedo $\alpha_{di} = 0.7$ (for $T_i <= T_m$ and $h_s = 0$),
- melting ice albedo $\alpha_{mi} = 0.68$ (for $T_i > T_m$ and $h_s = 0$),
- snow albedo $\alpha_{ds} = 0.81$ (for $T_i <= T_m$ and $h_s > 0$),
- melting snow albedo $\alpha_{ms} = 0.77$ (for $T_i > T_m$ and $h_s > 0$),

where $T_i$ is the temperature in °C at the snow or ice surface (towards the atmosphere), respectively. Fluxes over open water are calculated separately using a fixed ocean albedo $\alpha_o = 0.1$.

I have conducted some preliminary tests concerning perturbations to $\alpha_i$. Tests include perturbing only the ice albedos $\alpha_{di}$ and $\alpha_{mi}$, and perturbing $\alpha_i$ after it has been calculated. In addition, I applied not only symmetric perturbations, as was the case for $P^*$, but I also tested the asymmetric perturbations described in appendix D.2. This seems reasonable, as sub-scale features on sea ice such as melt ponds and soot can lower the albedo considerably. Therefore the perturbation scheme should allow for low values of $\alpha_i$, with a low probability of occurrence, though. A symmetric perturbation of values already close to the upper boundary 1 would prevent this. Furthermore, I have tested different spatial correlation schemes for the albedo perturbations. All of these tests have been sensitivity studies and results can only be viewed as preliminary. Therefore, I will restrict this discussion to one single example of a sea ice albedo perturbation.

Figure D.6 shows the relative difference in Arctic sea ice thickness caused by $P^*$ and $\alpha_i$ perturbations, separately, when compared to a deterministic FESOM simulation. The perturbations of $\alpha_i$ are spatially correlated by a correlation matrix comparable to the one used in chapter 4 for the $P^*$ perturbations, with a very large correlation distance of $d_{corr} = 4000\,\text{km}$. The only other difference in the spatial correlation method is that a correlation matrix on a coarser rectangular grid is used to generate the pattern. This reduces the computational costs of the pattern generation. After the generation, values of the correlation pattern are interpolated to the finer FESOM grid. Another difference to the $P^*$ perturbations is the application of an asymmetric transformation for the Gaussian random numbers (see appendix D.2). A perturbation in the range of $-80\%$ to $+20\%$ is applied to the albedo $\alpha_i$ after its calculation.

A single 3-year simulation with albedo perturbations has been conducted. The simulation applying $P^*$ perturbations is the same as the MTSP0 simulation of chapter 3.

Figure D.6 illustrates that the impacts of the $P^*$ perturbations are especially strong near the coast lines and in the eastern Arctic, while the albedo perturbations primarily affect regions close to the ice edge. Furthermore, the albedo perturbations show a general decrease in sea ice thickness, which is mainly caused by the asymmetric perturbations. These allow for much lower albedos to occur. Generally, figure D.6 highlights the different areas effected by uncertainties in the formulation of the sea ice dynamics and thermodynamics. Further investigations in this context will be necessary.

Additionally, it is also important to note that albedo parameterizations differ quite considerably between models. While FESOM uses a rather simple sea ice albedo parameterization,

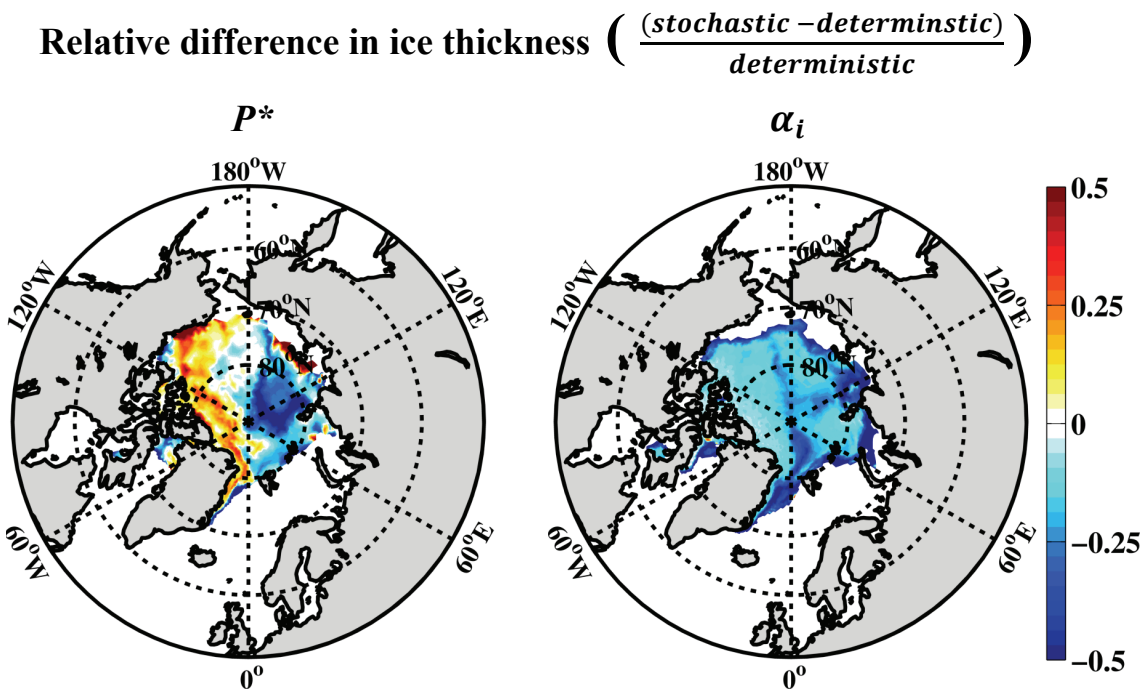


Figure D.6: Relative difference in northern hemisphere sea ice thickness between simulations with (left) $P^*$ and (right) $\alpha_i$ perturbations and the respective deterministic reference simulation without parameter perturbations. Simulations have been carried out with FESOM, applying CORE version 2 atmospheric forcing (*Large and Yeager*, 2009). Shown are the monthly mean differences of March for one year, three years after initialization.

ECHAM6 applies a much more sophisticated parameterization (*Giorgetta et al.*, 2013). It includes among others effects of melt ponds fraction, snow cover fraction and separation of radiation into different spectral bands. This makes albedo perturbations for different models difficult to compare. Furthermore, strong atmospheric feedback mechanisms in response to albedo perturbations might result in quite different responses in a fully coupled compared to sea ice–ocean models.

Due to the diversity of albedo parameterizations it is reasonable to develop a new stochastic parameterization for sea ice albedo. It should include the stochastic aspects right from the beginning and could be validated against observational data [13].

## D.2. Alternative perturbation designs

For the albedo perturbations of appendix D.1.2 I have developed an asymmetric transformation. It is based on the transformation given by equation (A.1) in the appendix A. The purpose is to transform a Gaussian distributed random number into a limited range to keep perturbations within physically realistic limits.

All the necessary calculations for generating temporal and spatial correlations are carried

[13] See for example the observational data (including albedo measurements) of the Surface Heat Budget of the Arctic Ocean (SHEBA) project at `http://www.ral.ucar.edu/projects/GCSS/WG5/shebasid.html` (16.05.2014).

out with Gaussian distributed random numbers prior to the transformation. The advantage is that linear combinations of Gaussian distributed random numbers are still Gaussian distributed. Therefore, transformation into a limited range is applied only after all other necessary calculations have been carried out.

The transformation should meet the condition that it transforms the random numbers into a bounded distribution with a single probability maximum at 0 and zero probability at the limits. The transformation of equation (A.1) meets these requirements. And so does the generalized transformation

$$x = -a + \frac{b-a}{1 - \frac{b}{a}e^{-\beta y}} \tag{D.2}$$

with $y$ some Gaussian distributed random variable with zero mean and standard deviation $\sigma$. The parameter $\beta$ lies in the range $0 < \beta < \sqrt{2}/\sigma$. It arises from the necessity to keep the maximum of the transformed distribution at 0. This can be shown by calculating the distribution function using a transformation theorem for random numbers (see e.g. *Lefebvre*, 2007) and then calculating the first and second derivatives of the distribution function (calculations not shown). For a local maximum the conditions are for the first derivative to be equal to 0 and for the second derivative to be smaller than 0. Applying these conditions to the distribution function of the transformed random numbers at 0, the above condition for $\beta$ can be derived.

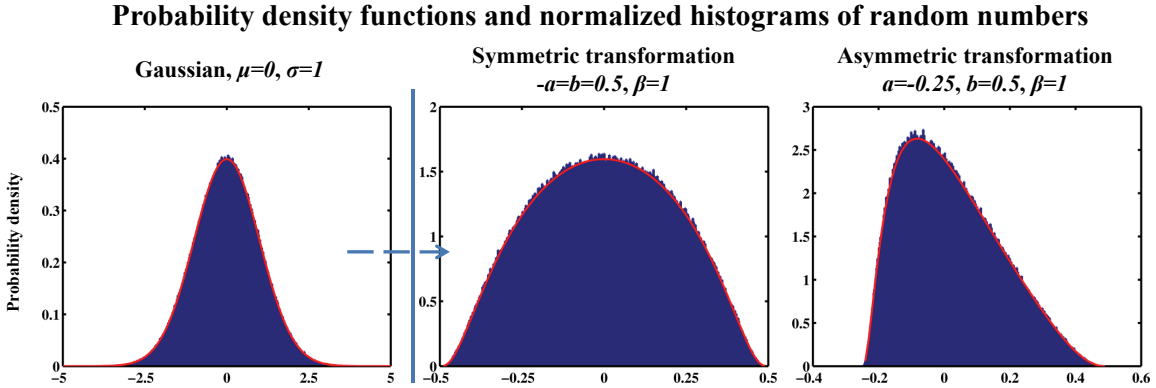


Figure D.7: Distribution functions of (left) a Gaussian distributed random number ($\mu = 0$ and $\sigma = 1$), (middle) a symmetric transformation of the Gaussian distributed random number using equation (D.2) (limits $-a = b = 0.5$, $\beta = 1$) and (right) an asymmetric transformation of the Gaussian distributed random number using equation (D.2) (limits $a = -0.25$ and $b = 0.5$, $\beta = 1$). Shown are the theoretic distribution functions (red lines) and the (normalized) histograms of the respective computer-generated random numbers (blue bars).

The parameters $a < 0$ and $0 < b$ are the lower and upper bound of the transformed distribution function. Inserting $a = -b$ for a symmetric transformation results in equation (A.1). It should be noted that, for the transformation of equation (D.2), 0 is also an invariant point. Figure D.7 illustrates the symmetric and asymmetric distribution functions, as well as the respective Gaussian distribution function. Results from theoretical calculations as well as transformed computer-generated random numbers assort well.

Using different transformations such as the one given by equation (D.2) can be very useful when the perturbations have to be adjusted for different parameters. Another aspect of pertur-

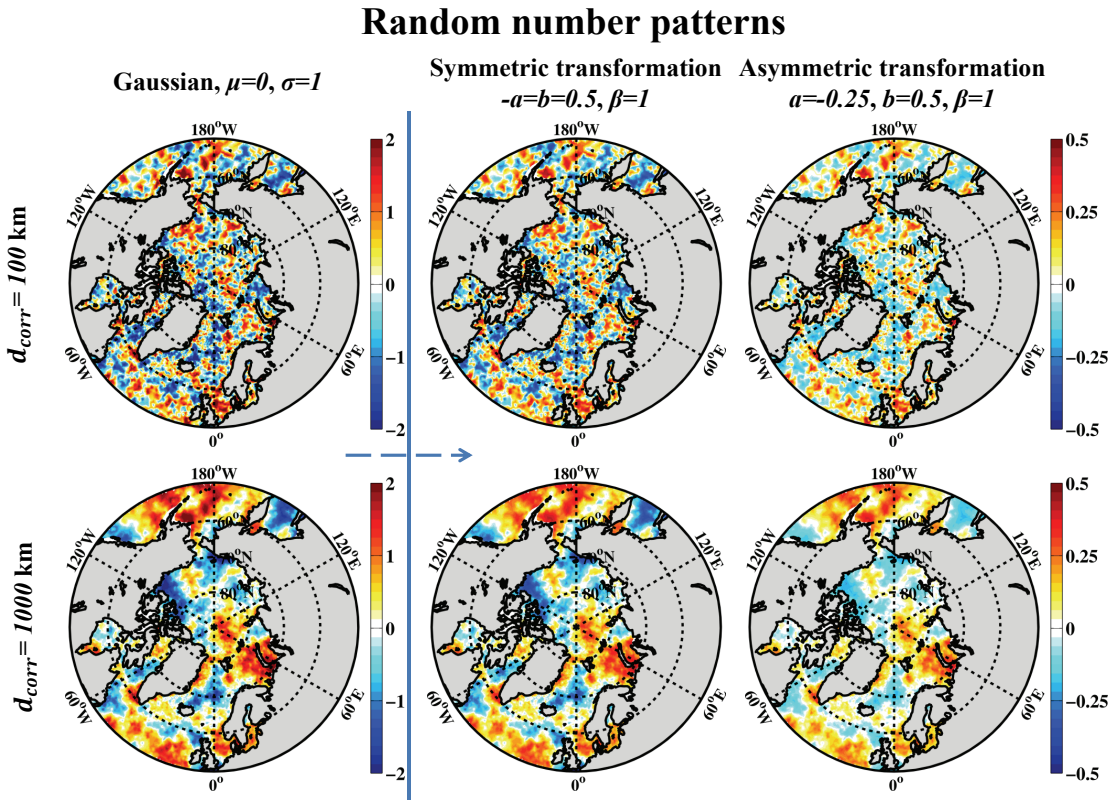


Figure D.8: Patterns of random numbers with (left) a Gaussian distribution ($\mu = 0$ and $\sigma = 1$), (middle) after a symmetric transformation of the Gaussian distributed random numbers using equation (D.2) (limits $-a = b = 0.5$, $\beta = 1$) and (right) after an asymmetric transformation of the Gaussian distributed random numbers using equation (D.2) (limits $a = -0.25$ and $b = 0.5$, $\beta = 1$). Patterns are generated for two different correlation distances, (top) $d_{corr} = 100\,\text{km}$ and (bottom) $d_{corr} = 1000\,\text{km}$, using the pattern generation strategy described in chapter 4.

bation design is the strategy applied to create the spatial correlation. Chapters 3 and 4 have introduced two different spatial correlation schemes, both of which have been isotropic. Many other schemes are imaginable, isotropic as well as anisotropic. Figure D.8 illustrates the impact of changes in the spatial correlation parameter $d_{corr}$ of the correlation matrix described in chapter 4, using the same pattern generation scheme. In addition, transformation (D.2) is applied to the patterns of Gaussian distributed random numbers, both for a symmetric and an asymmetric configuration, to illustrate the combined effect of spatial correlation and transformation of random numbers into a bounded distribution.

## D.3. Coupling uncertainty

Another application of stochastic perturbations that is currently being investigated is connected to the coupling procedure between FESOM and ECHAM6 described in section 2.2.2. In the deterministic ECHAM6-FESOM model spatially averaged snow and sea ice thickness, sea ice concentration, and sea surface temperature fields are calculated on the FESOM grid and passed to the intermediate grid. The OASIS3-MCT coupler uses a bilinear interpolation to communi-

cate these fields from the intermediate grid to the ECHAM6 grid. In some regions, where the FESOM grid resolution is very high, dozens of FESOM grid points are associated with one single intermediate grid node. When FESOM values are averaged, information on spatial variability of the respective surface field is lost. From the perspective of the intermediate and the ECHAM6 grid, this variability belongs to the sub-grid scale.

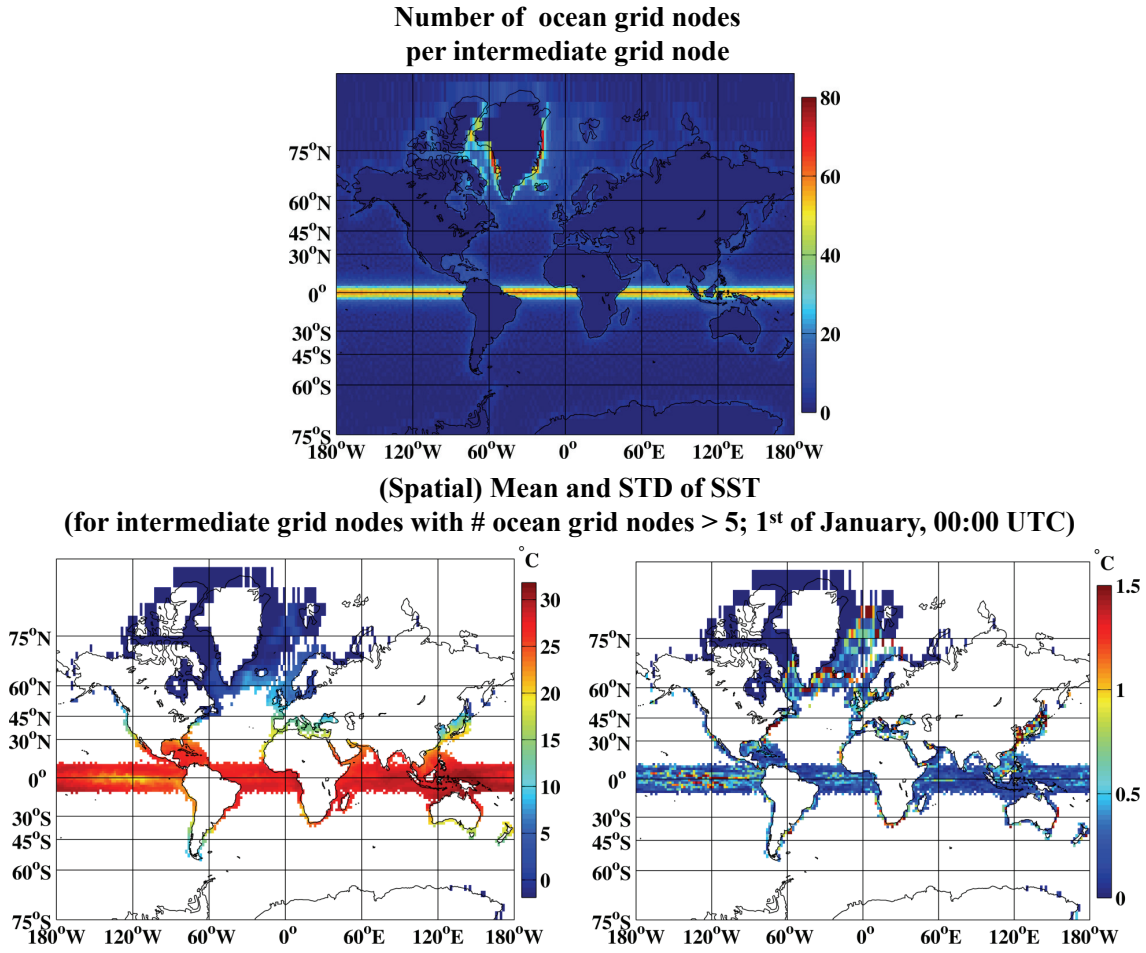


Figure D.9: Illustration of the resolution difference between the FESOM grid and the intermediate grid used for the coupling to ECHAM6: (top) the number of FESOM grid nodes associated with the respective intermediate grid node; (bottom left) the mean sea surface temperature [°C] as an average over the associated FESOM grid nodes as seen by the intermediate grid; (bottom right) the standard deviation of sea surface temperature of the associated FESOM grid nodes [°C] for each intermediate grid node. The bottom panel shows values for the first of January, 00:00 UTC, of an arbitrary year of the coupled simulation and only for those intermediate grid nodes with more than 5 FESOM grid nodes.

Figure D.9 (top) illustrates the number of FESOM grid nodes associated to each of the intermediate grid nodes. This number varies from less than three in the open oceans, where FESOM grid resolution is coarse, to well above 40 nodes along the highly resolved equatorial belt and the coast of Greenland. Relatively higher resolution can also be found along most coastlines.

In addition, figure D.9 (bottom left) shows spatially averaged sea surface temperature of the

intermediate grid exemplary for the first of January of some arbitrary model year. Shown are only the sea surface temperatures of those intermediate grid nodes to which more than 5 FESOM grid nodes belong. The rather coarse intermediate grid resolution is sufficient to be able to make out regions of strong temperature gradients, especially in the equatorial Pacific region and along the western boundary currents. These strong gradients can also be found when considering sea ice fields (not shown). Especially along the ice edge and the coastal regions, values of sea ice thickness and concentration can vary considerably from one intermediate grid node to another. The spatial variability of the FESOM grid nodes belonging to an intermediate grid node can be even larger. Spatial averaging smoothes out small-scale features originating from localized sea ice ridging, the steep concentration gradients along the ice edge, or sea surface temperature gradients along fronts or eddies. This sub-grid scale variability of the ocean surface fields can be illustrated by looking at the spatial standard deviation, for intermediate grid nodes to which more than 5 FESOM grid nodes are associated. This is shown in figure D.9 (bottom right) for sea surface temperature. Temperature standard deviations can be larger than 2°C along the equatorial belt, the western coastlines and the ice edge in the North Atlantic. Similarly strong variability can be observed for the sea ice fields (not shown).

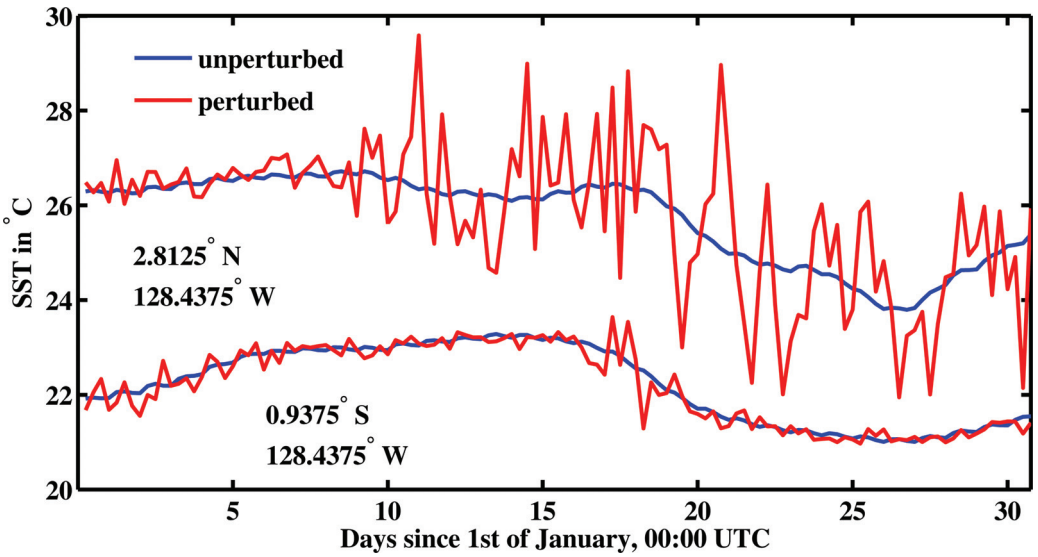


Figure D.10: Evolution of sea surface temperature [°C] at two locations in the equatorial Pacific (at $2.8125°N$, $128.4375°W$ and $0.9375°N$, $128.4375°W$), for a January of an arbitrary year of the coupled simulation. Shown are the unperturbed sea surface temperature fields (blue) and the stochastically perturbed fields (red). See text for details on the perturbation method.

While FESOM is capable of very localized grid refinements, ECHAM6 is not. Averaging of FESOM fields causes uncertainties in the simulations, as ECHAM6 cannot process the actually simulated surface fields due to its coarser resolution. To include a measure of coupling uncertainty and possibly even increase the accuracy of the coupling procedure, the basic idea is to communicate not only the mean fields, but to calculate in addition the spatial standard deviations of the FESOM grid. This is done for intermediate grid nodes with more than 5 FESOM grid nodes and every 6-hourly coupling interval. Based on these standard deviations, the mean fields can be perturbed on the intermediate grid to estimate the uncertainty of the flow.

Independent Gaussian distributed random numbers with the respective standard deviations are used for the perturbations at the selected intermediate grid nodes. By that uncertainty in the actual choice of the nodal field value can be sampled and the variability of the surface fields used by ECHAM6 is increased. The perturbations are applied to the sea surface temperature, to $h/A$, and to $h_s/A$. The perturbations of the latter two terms are used to calculate the perturbations of the separate fields $A$, $h$, and $h_s$. This procedure has been chosen to keep the ratios $h/A$ and $h_s/A$ within reasonable bounds. After the perturbations have been applied, values need to be additionally transformed into a physically realistic range. Details of the perturbation procedure are currently investigated.

Figure D.10 provides a first impression of the perturbations of sea surface temperature at two different locations in the equatorial Pacific. Shown are both unperturbed mean values and randomly perturbed values (following the procedure described above) at the two locations. It illustrates how the sub-grid scale temperature variability varies over time, as sub-grid scale features exhibiting strong temperature gradients pass through. First results of this perturbation method are currently being evaluated, in view of impacts on global mean climate and climate variability.